UNIVERSITÀ DEGLI STUDI DI ROMA "TOR VERGATA"

FACOLTA' DI SCIENZE MATEMATICHE FISICHE E NATURALI

DOTTORATO DI RICERCA IN
MATERIALI PER L'AMBIENTE E L'ENERGIA

CICLO DEL CORSO DI DOTTORATO
XII

Thin films growth by Pulsed Laser Deposition for Solid Oxide Fuel Cell applications

Simone Sanna

A.A. 2009/2010

Docente Guida/Tutor: Dr. Antonello Tebano, Prof. Giuseppe Balestrino

Coordinatore: Prof. ssa Silvia Licoccia

Abstract

La crescente domanda di sistemi miniaturizzati per la conversione e stoccaggio dell'energia ha spinto un'ampia ricerca finalizzata alla fabbricazione di dispositivi ionici a stato solido sotto forma di film sottile. Vale a dire, negli ultimi anni molti ricercatori stanno lavorando per realizzare le celle a combustibile Ossidi solidi in scala micrometrica (micro-SOFC). Le micro celle a ossidi solidi sono molto promettenti, in quanto una riduzione su scala micrometrica dello spessore dei componenti delle celle a combustibile (catodi, elettroliti e anodi) comporta un aumento considerevole delle prestazioni. Prestazioni più elevate del SOFCs consente di ridurre la temperatura di esercizio (circa 800-1000°C per SOFC convenzionali basate su zirconia stabilizzata con yttria (YSZ)) tali da consentire il loro uso come batterie per i dispositivi portatili. Dispositivi elettrochimici possono essere miniaturizzati per applicazioni portatili (μ-SOFC), utilizzando nuove tecniche di deposizione di film sottili. Una delle tecniche più promettenti è la Pulsed Laser Deposition (PLD). Questa tecnica è adatta a crescere ossidi complessi e eterostrutture con spessore complessivo di pochi nanometri. In questa tesi abbiamo utilizzato la tecnica PLD per la fabbricazione di componenti SOFC, come elettroliti e catodi. La qualità cristallina e la struttura morfologica dei film sottili sono state studiate con la diffrazione a raggi X (XRD) e con il Field Emission Scanning Electron Microscopy (FE-SEM). In conclusione, le prestazioni dei componenti sono stati studiati con la Spetettroscopia di Impedenza ad alta e bassa pressione parziale di ossigeno nell’inervallo di temperature che vanno da 400°C a 800°C.
Capitolo 1 è incentrato sullo stato dell'arte delle tecnologie a film sottile in μ-SOFC.
Capitolo 2 spiega le tecniche utilizzate per la sintesi e la caratterizzazione elettrochimica di film sottili e di eterostrutture.
Capitolo 3 mostra le proprietà della Ceria drogata con Samario (SDC) sotto forma di film depositato su MgO (001).
Capitolo 4 illustra i meccanismi di conducibilità ionica all'interfaccia SDC/YSZ di film superreticoli depositati su MgO.
Il capitolo 5 mostra le prestazioni dei catodi nano-porosi confrontati a catodi densi.

A mio figlio

Contents

Chapter 3

Structural and electrochemical characterization of epitaxial Samarium-doped ceria thin film

Chapter 4

Structural and electrochemical characterization of [SDC/YSZ] heterostructures

Chapter 5

Nanostructured cathode thin films grown by Pulsed laser deposition

Outline

The growing demand for miniaturized systems for energy conversion and storage has prompted extensive research aimed at the fabrication of solid state ionic devices in thin film form. Namely, in the recent years many researchers are working to realize Solid Oxides Fuel Cell in micrometric scale (micro-SOFCs). Micro-SOFCs are very promising because a reduction to the micro-scale of the fuel cell components (cathodes, electrolytes and anodes) thickness has relevant consequence to increase the performances. Higher performance of the SOFCs means to reduce the working temperature (about 800-1000 °C for conventional SOFC based on yttria-stabilized zirconia) allowing their use as batteries in the portable devices. Electrochemical devices can be miniaturized for portable applications (μ-SOFCs) using novel deposition techniques of thin films and heterostructures. One of the promising

technique is Pulsed Laser Deposition (PLD). Namely, this technique is suitable to grow complex oxides and heterostructures with overall thickness of few nanometers. In this thesis we used the PLD technique for the fabrication of SOFC components, such as electrolytes and cathodes. The crystalline quality and the morphological structure of the thin films were investigated by X-Ray Diffraction (XRD) and Field Emission Scanning Electron Microscopy (FE-SEM). In conclusion the performances of the components were studied using Electrochemical Impedance technique at high and low oxygen partial pressure in the temperature range from 400°C to 800°C.

Chapter 1 is focused on state of the art of thin film technologies in the μ-SOFCs.

Chapter 2 explains the techniques used for the synthesis and the electrochemical characterization of the thin films and the heterostructures.

Chapter 3 shows the properties of the epitaxial Samarium-doped Ceria (SDC) thin film with lower and higher mosaic spread deposited onto MgO (001) single crystals.

Chapter 4 shows the ionic mechanisms of the conductivity at the interface in the SDC/YSZ multilayered systems.

Chapter 5 shows the performances of the nano-porus cathodes with larger active surface and larger triple phase boundary (TPB) at the electrode/electrolyte compared to dense cathodes.

Chapter 1

Overview

1.1 Solid Oxide Fuel Cells description

Fuel cells are electrochemical devices that convert the chemical energy of a reaction directly into electrical energy. Fuel cells consist of an electrolyte layer in contact with a porous anode and cathode on either side. A schematic representation of a fuel cell, based on oxygen-ion conductor, with the reactant/product gases and the ion conduction flow directions through the cell is shown in Figure 1. In a typical fuel cell, gaseous fuels are fed continuously to the anode (negative electrode) and an oxidant (i.e., oxygen from air) is fed continuously to the cathode (positive electrode); the electrochemical reactions take place at the electrodes to produce an electric current.

Solid oxide fuel cells (SOFCs) are advanced electrochemical reactors operating at high temperature. SOFCs are presently under development for a variety of electric power generation applications with high energy conversion efficiency [1].

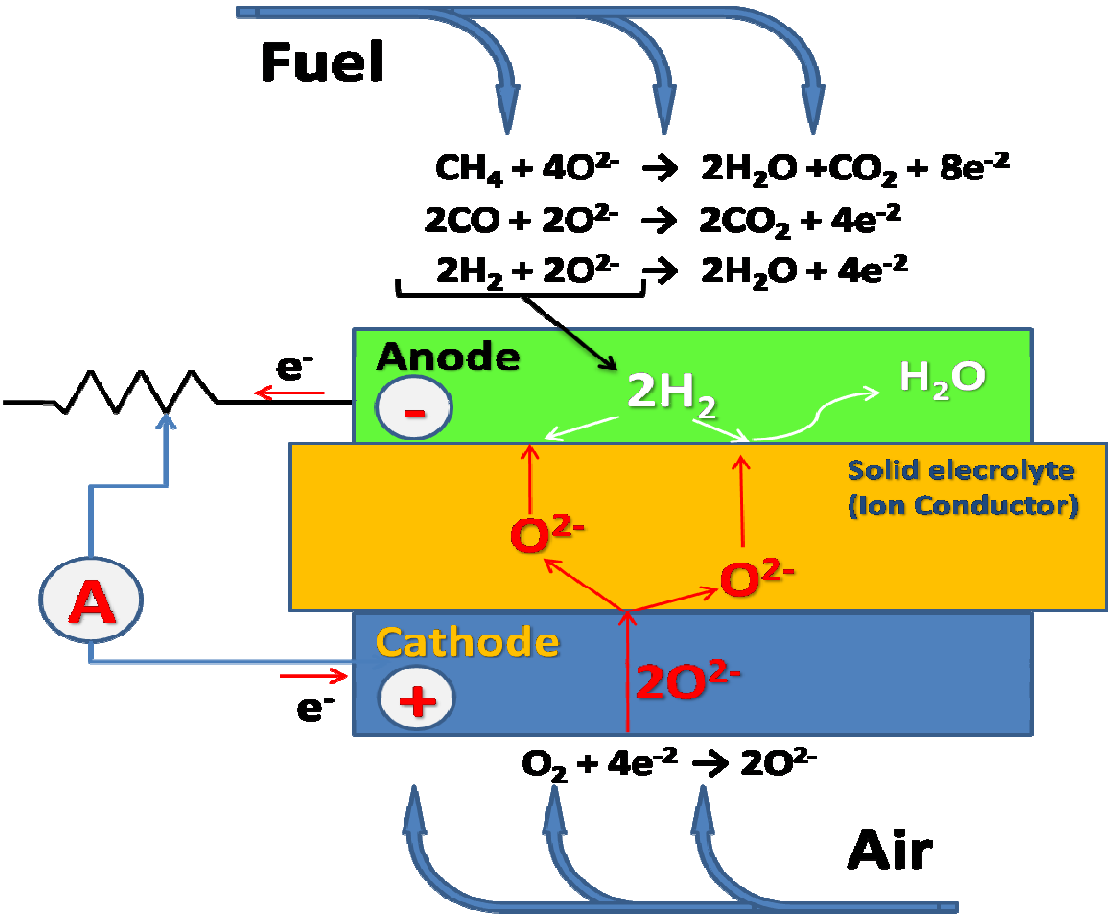

Figure 1. Diagram of the SOFC based oxygen-ion conductor.

The main advantages of the SOFC can be summarized as follows:

- SOFCs are flexible in the choice of fuel such as carbon-based fuels
- SOFCs have a solid state construction and, as they have no moving parts, can be installed indoors.

- The high operating temperature of SOFCs produces a high quality heat byproduct which can be used for co-generation, or in combined cycle applications.
- SOFCs do not contain noble metals.
- SOFCs have extremely low emissions, eliminating the danger of carbon monoxide in exhaust gases as any CO produced is converted to CO_2 at the high operating temperature.

1.2 Micro-SOFCs

Historically, the materials used for SOFC applications are bulk ceramics and thick films (several micrometers). However, recent trends indicate an increasing interest in thin films SOFC components with thickness of a few nanometers. In particular, the researchers are focused on the fabrication of electrolyte thin films to reduce the ohmic resistance. One of the reasons for the interest in micro-SOFCs is to decrease the operating temperature from the range of 800-1000°C to 600-800°C due to nano-scale dimension . These lower operating temperatures enable the use of lower-cost metallic interconnectors, reduce the thermal stress in the SOFC and possibly allow their use as portable power generators in devices such as laptop computers and mobile telephones. Lower temperatures lead to increased electrolyte ohmic resistance, given the thermally activated behavior of ionic transport. This effect, however, can be compensated by decreasing electrolyte thickness [2].

Thin film deposition can be combined with micro-machining techniques in order to realize fuel cells with micrometer dimensions. In fact, thin films can be deposited on insulating substrate and after the deposition it can be etched.

Figure 2 shows a sketch of a micro-SOFC with double chamber (one for a fuel and one for air).

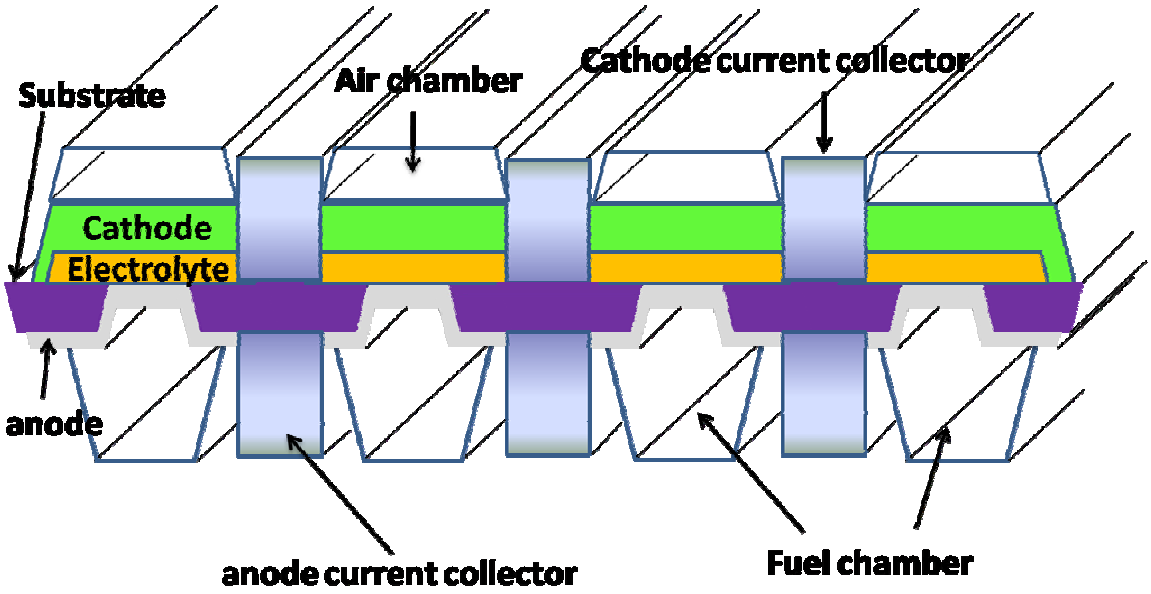

Figure 2. Sketch of a micro-SOFC.

Figure 3 shows a FE-SEM micrograph of a prototype of a free standing micro-SOFC deposited on a silicon nitride (SiN) membrane by pulsed laser deposition (PLD). The SiN membrane was etched by reactive ion etching (RIE) [2].

The prototype was made in three steps:

- Sequential deposition of the electrolyte and anode on the SiN membrane without exposure to atmosphere by PLD.
- Etching of the SiN membrane left on the back side of the chip by RIE.
- Deposition of the porous cathode on the back side of the chip at room temperature by PLD.

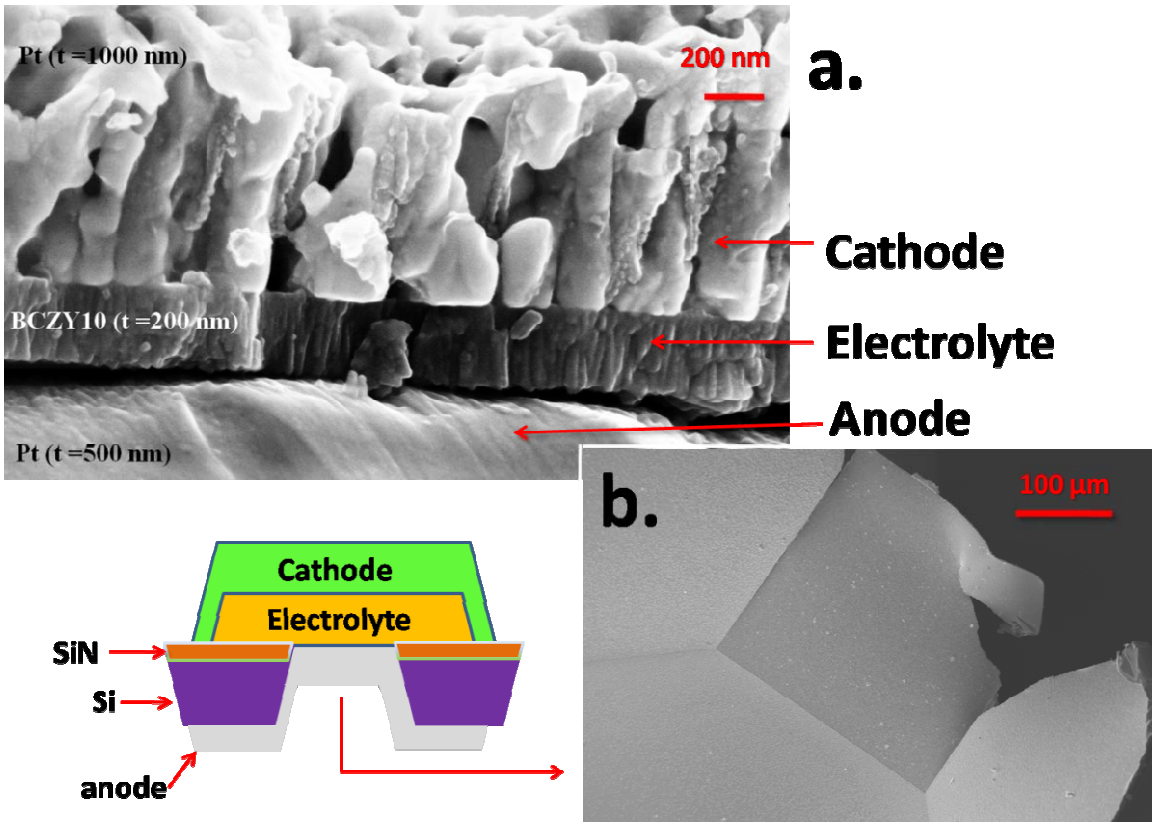

Figure 3. FE-SEM micrograph of cross section (a.) and surface-views (b.) of micro-SOFC prototype.

1.3 Ionic conductivity in ultra thin films and heterostructures

Several researchers such as Maier, Kosacki, Tuller etc. are studying the relationship between the thickness and the ionic conductivity of the electrolyte thin films [3-4].

Kosacki, in particular, reported an enhancement in the ionic conductivity of 10 mol% YSZ thin films for a thickness of less than 60 nm deposited on MgO. The enhancement was attributed to a highly conductive interfacial layer at the YSZ and MgO interface.

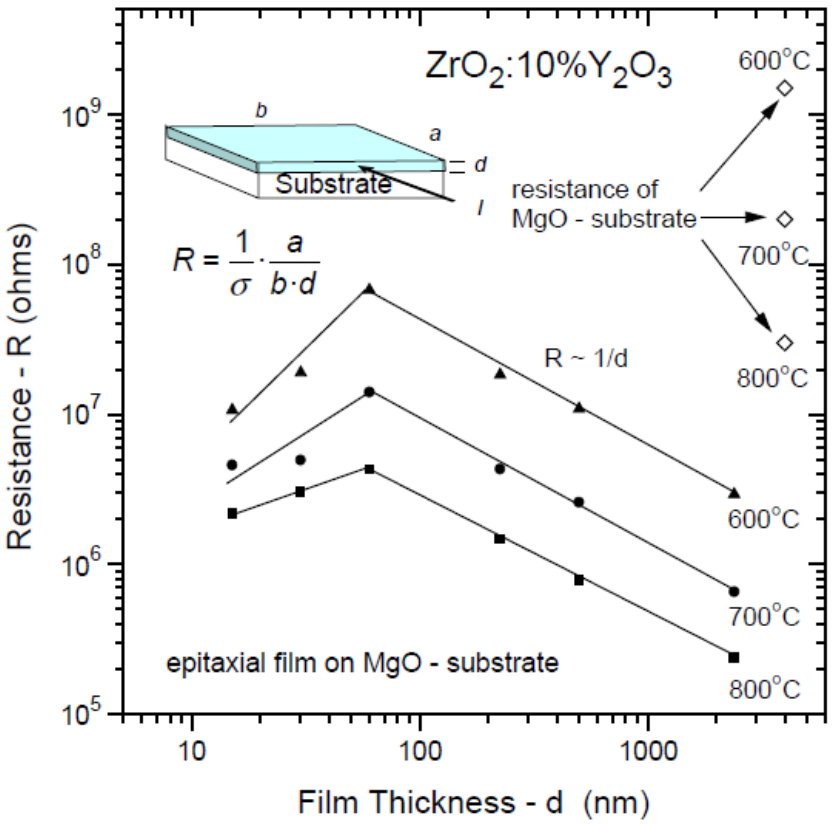

Figure 3. The resistance of YSZ thin films deposited on MgO substrate as a function of the thickness [3-4].

Maier et al studied the electrical behavior of interfacial regions, which often differs from that of bulk due to space charge effects in the superlattice thin films. In fact, Maier and his coworkers extended the space-charge concept as one of the possible origins of a higher conductivity along interfaces in the nano-scaled materials. This effect is confined to lengths in the order of the Debye length Λ_D:

$$\Lambda_D = \sqrt{\frac{\varepsilon RT}{2z^2F^2c_\infty}} \qquad (1)$$

where ε is dielectric constant, z is the number of charges on the defect, c_∞ is the molar concentration of defect far from the interface, R is the gas constant and F is Faraday constant. Typical Debye length for extrinsic materials is about 10 nm. For

highly doped, such as SDC and YSZ materials the length of d can be neglected. A Structurally disturbed interface region might result an increase of ionic conductivity. Figure 4 shows the space charge region of an oxygen ion conductor with an increased density of mobile ionic charge carriers for a disordered interface region.

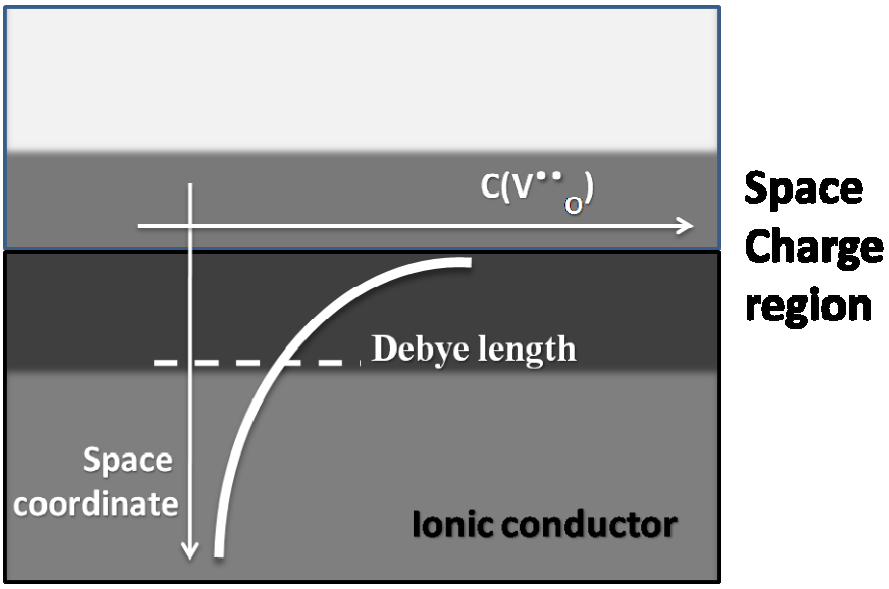

Figure 4. Space charge region of an oxygen ion conductor.

Figure 5 shows the parallel ionic conductivity of CaF_2/BaF_2 heterostructures deposited by molecular beam epitaxy (MBE) on Al_2O_3 for films with various periods (thickness of single bi-layer) and interfacial densities in the 430-16 nm range with the overall thickness is 500 nm [5]. Maier shows an enhancement of the ionic conductivity from 430 nm to 16 nm. When the period is less than 16 nm he observed a decrease of the ionic conductivity, probably due to the lack of continuity for tiny thicknesses [5].

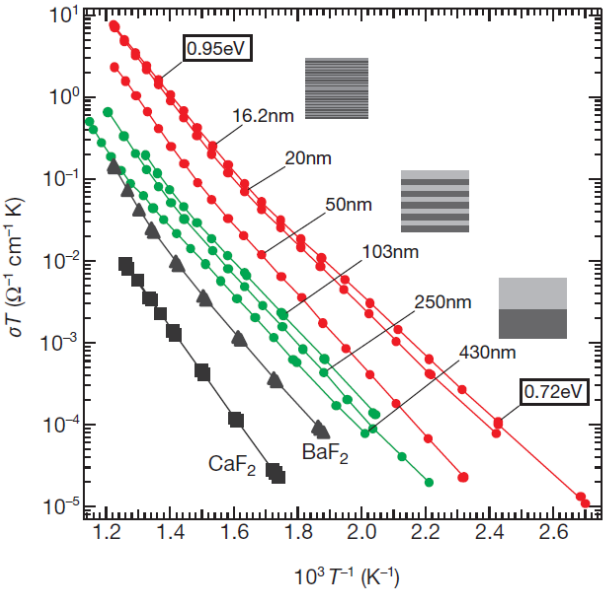

Figure 5. Ionic conductivity of CaF_2/BaF_2 heterostructures deposited onto Al_2O_3 from 430 nm to 16 nm [5].

Figure 6 shows the conductivities as a function of the period (thickness of bi-layer) for films of CaF_2/BaF_2 with overall thickness in the range 430-2 nm.

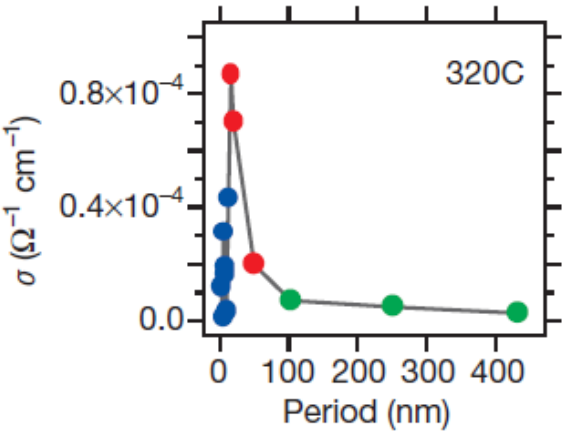

Figure 6. Conductivities as in function of the period in the range 430-2 nm [6].

Electrical conductivity of Gadolinium-doped-ceria (GDC) and Yttria–stabilized Zirconia (YSZ) films have been extensively studied for application in micro-SOFC. Several researchers such as Maier, Gauckler, Ramanathan, Guo and Kosacki investigated microstructural effects, strain effects and space charge effects induced by the substrates.

Azad et al. studied the nanoscale effect on ionic conductivity of GDC/ZrO_2 heterostructures deposited onto Al_2O_3 single crystals [6]. Structural characterization indicated that microstructural defects such as dislocations exist in the layers as well as at interfaces resulting from the lattice mismatch between two materials (fig.7).

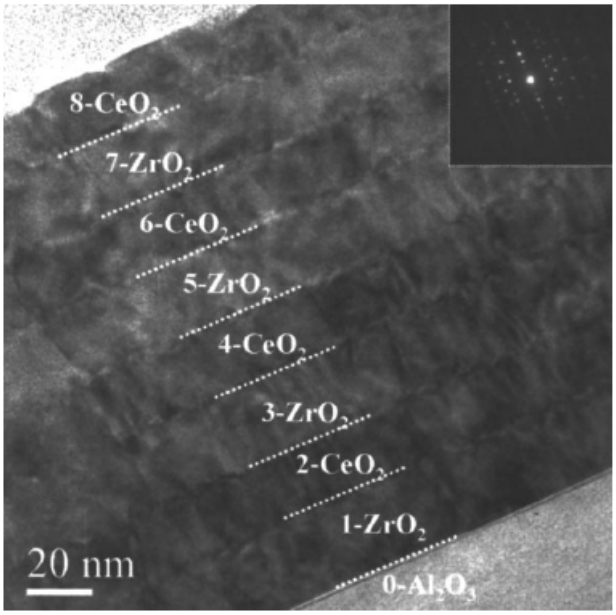

Figure 7. TEM- micrograph of GDC/ZrO_2 heterostructure deposited onto Al_2O_3 [6].

Similar to the fluoride heterolayers such as GDC and ZrO_2, the overall oxide ionic conductivities increase continuously with decreasing individual thickness, while they decrease as the value of individual thickness is reduced below 15 nm. According to Azad et al., this is due to strain effects associated with the thin films compared to the

thick films. The maximum increase in conductivity is around one order of magnitude compared to a single phase polycrystalline Gd: CeO_2 bulk or a single-crystal YSZ film. The authors proposed that such conductivity increase was attributed to effects of microstructural defects, which may increase the solubility of Gd in CeO2 layers or the mobility of the oxygen vacancies. Figure 8 shows the conductivity as a function of the number of layers with individual thickness of 15 nm [6].

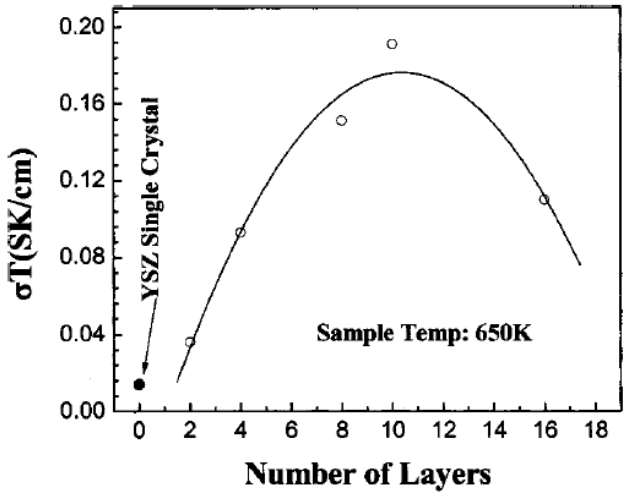

Figure 8. Conductivities of single crystal YSZ, and several number of layers at 650K [6].

The drop of conductivity for the sample with sixteen layers is probably due to high crystallographic disorder.

ZrO_2-based heterolayer interfaces (YSZ/Lu_2O_3, YSZ/Sc_2O_3, ZrO_2+CaO and YSZ/Y_2O_2) were investigated by Korte et al. in Janek's group [7-9]. They concluded that the large mismatch at the interface plays a fundamental role for the interface conductivity σ_{int}.

Their systems with lattice mismatch are dominated by elastic strain: slight dilatative strain in the YSZ/Lu_2O_3 systems, significant compressive strain in the YSZ/Sc_2O_3

systems and significant tensile strain for YSZ/Y_2O_2 heterostructure. The logarithm of $\sigma_{tot}/\sigma_{vol}$ vs. the lattices misfits [7] are reported in Figure 9.

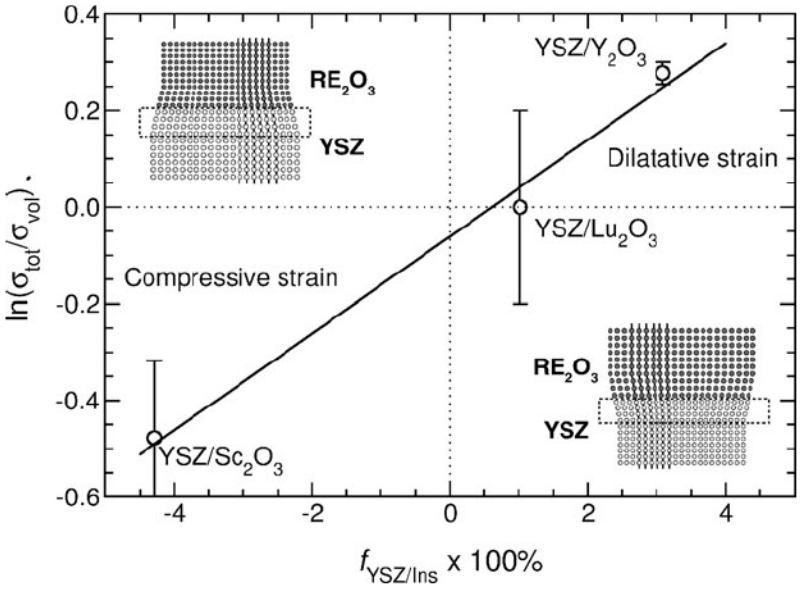

Figure 9. Plot of the logarithm of the maximum change $\sigma_{tot}/\sigma_{vol}$ of the total conductivity relative to the bulk conductivity against the mismatch factor f_{YSZ}/Ins [7].

An expression to calculate the ratio between the interface conductivity σ_{int} and the bulk conductivity σ_{bulk} as a function of the epitaxial strain $\Delta a/a$ was proposed:

$$\ln\left(\frac{\sigma_{\text{int}}}{\sigma_{bulk}}\right) \cong \frac{1}{3}\frac{\Delta V^{M}}{RT}\frac{Y}{1-\nu}\frac{\Delta a}{a} \qquad (2)$$

where ΔV^M, Y and ν represent the volume of migration of oxygen vacancies, the Young's modulus and the Poisson's ratio, respectively [10-12].

Figure 10 shows structurally disordered interface regions at a heterophase boundary.

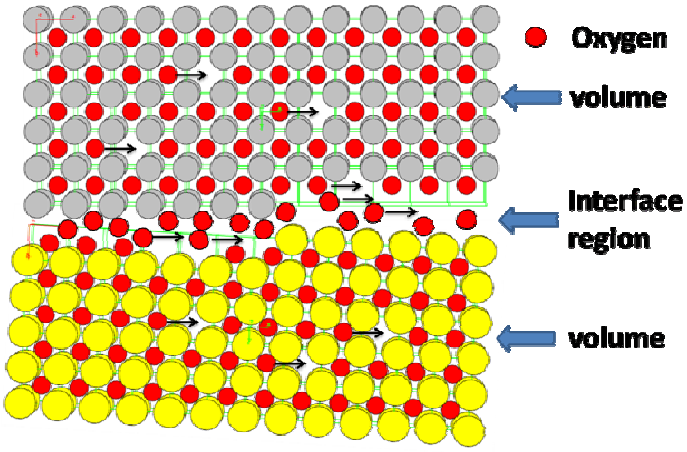

Figure 10. Structurally disordered interface region.

Interfaces between two different lattices like grain boundaries or phase boundaries can be structurally classified as coherent, semicoherent and incoherent interfaces depending on the degree of the mismatch [9].

- ***Coherent interface***: the ionic mobility can only be affected by residual lattice strain. The activation energy can change for atomic jumps in the strained region at the interface.
- ***Semicoherent interface***: several dislocations are present at the interface region. The lower packing density and strain field produce the ionic migration.
- ***Incoherent interface***: the interface structure is highly disturbed. In such regions, significant lower packing densities and different atomic interactions are present compared to the bulk. The result is higher ionic conductivity than that of semicoherent and incoherent interfaces.

In general, the interfacial transport becomes faster when changing the interfacial structure from coherent to semicoherent and finally incoherent. Figure 11 shows a sketch of the dependence of interface structure and the density of misfit dislocations on lattice mismatch.

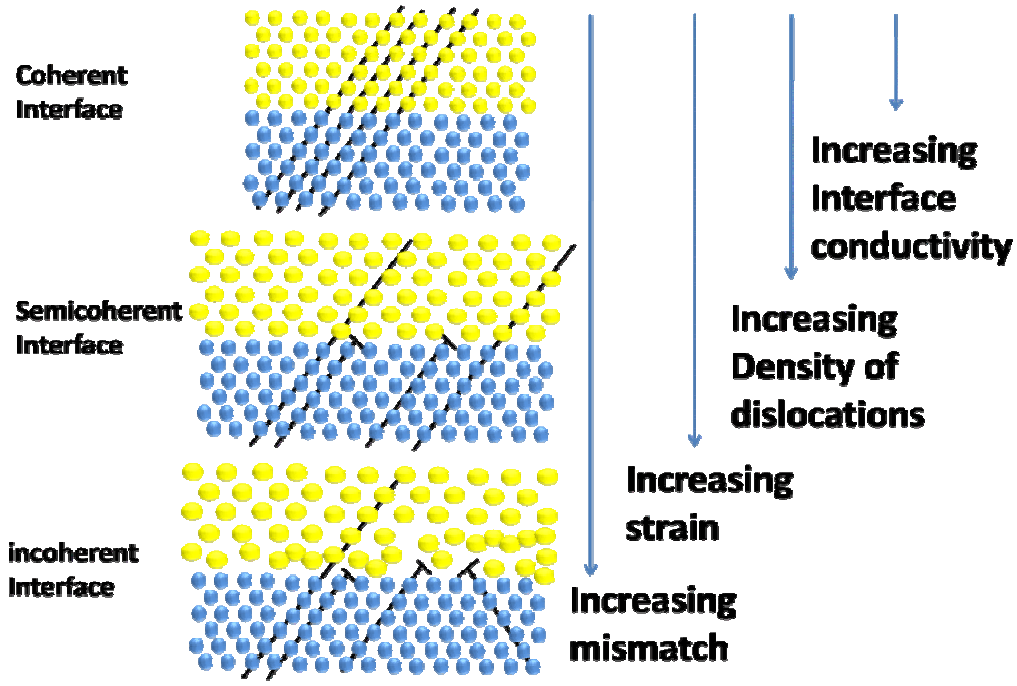

Figure 11. Sketch of the dependence of interface structure and the density of misfit dislocations on lattice mismatch.

Recently, the ionic conductivity of $SrTiO_3$/YSZ/$SrTiO_3$ trilayers deposited onto $SrTiO_3$ (STO) single crystal, were investigated by Garcia-Barriocanal et al [13]. They changed the thickness of YSZ from 62 nm to 1 nm maintaining constant (about 10 nm) the thickness of STO layer. They observed an enhancement of the conductivity by two to eight orders of magnitude compared to the conductivity of YSZ bulk. The authors proposed that both the concentration and mobility of carriers are varied owing to direct or indirect effects of strain. However, it is not clear if the colossal conductivity measured by Garcia-Barriocanal is dominated by ion carriers. Namely a significant electronic contribution is reported in the literature for perovskite thin film such as STO [14-15].

Figure 12 shows the dependence of the logarithm of the long-range ionic conductivity of the trilayers reported by Garcia-Barriocanal STO/YSZ/STO versus inverse temperature. The thickness range of the YSZ layer is 1 to 62 nm [13].

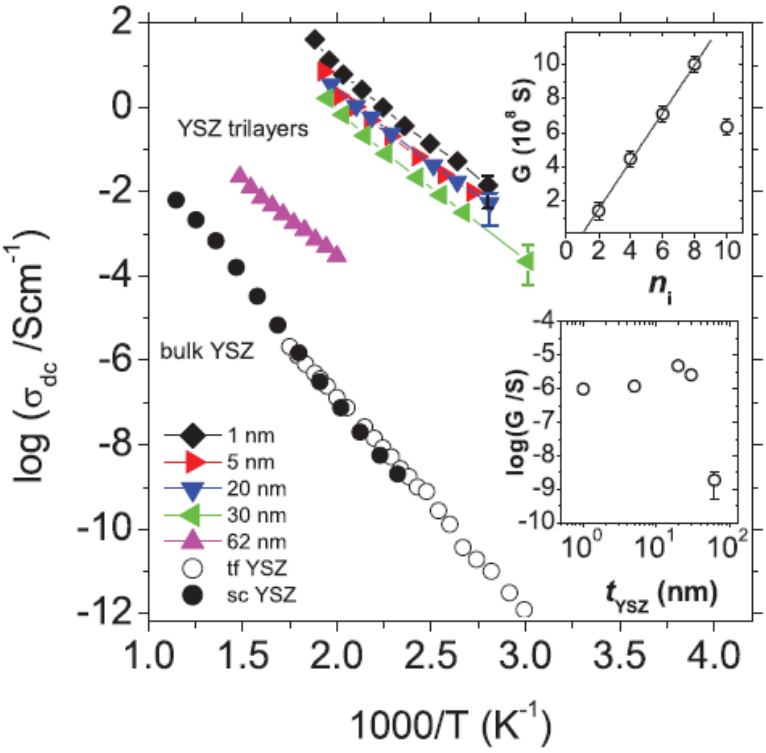

Figure 16. Conductivity of the trilayers reported by Garcia-Barriocanal STO/YSZ/STO [13].

Guo published a comment to Garcia-Barriocanal's paper: he proposes that the observed enhancement of the conductivity is mostly due to p-type conductivity of STO. Figure 16 shows a Nyquist of the STO substrate at 220°C [16]. Figure 17 shows the Arrhenius plot of the STO substrate and the heterostructures STO/YSZ/STO.

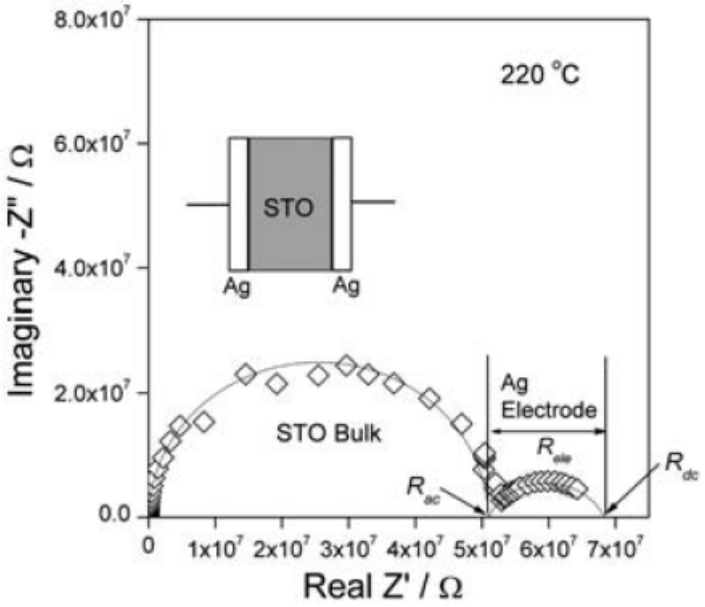

Figure 16. Impedance spectra of STO substrate at 220°C in air [16].

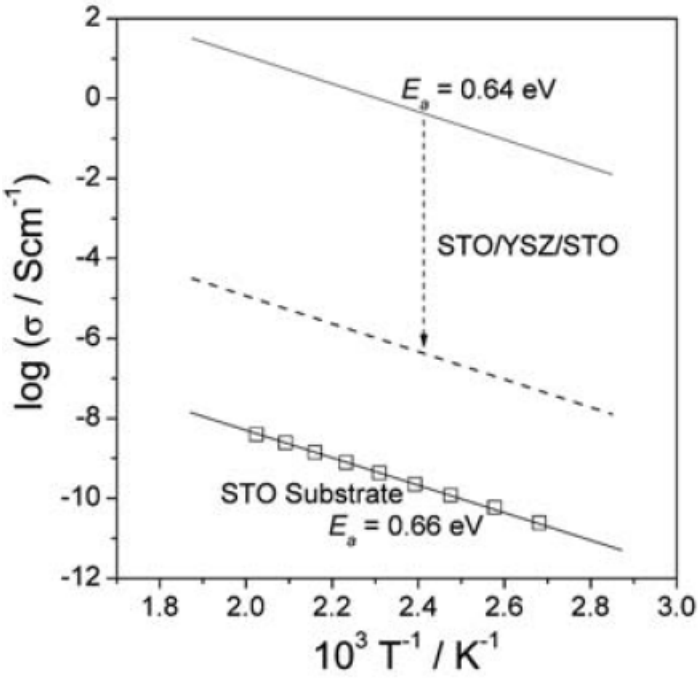

Figure 17. The Arrhenius plot of the STO substrate and the heterostructures STO/YSZ/STO [16].

The activation energy for STO and STO/YSZ/STO has the same value: this indicates that that the contribution of the substrate is predominant relative to the superlattices.

References

[1] A. Boudghene Stambouli, E. Traversa, *Renewable and Sustainable Energy Reviews* **2002** *6*, 433.

[2] U. P. Muecke, D. Beckel, A. Bernard, A. Bieberle-Hutter, S. Graf, A. Infortuna, P. Muller, J. L. M. Rupp, J. Schneider, and L. J. Gauckler, *Adv. Funct. Mater.* **2008**, *18*, 3158.

[3] I. Kosacki, C. M. Rouleau, P. F. Becher, J. Bentley, D. H. Lowndes, *Electrochem. Solid State Lett.* **2004**, *7*, A459.

[4] I. Kosacki, C. M. Rouleau, P. F. Becher, J. Bentley, D. H. Lowndes, *Solid State Ionics* **2005**, *176*, 1319.

[5] N. Sata, K. Eberman, K. Eberl, J. Maier, *Nature* **2000,** *408*, 21/28 DECEMBER.

[6] S. Azad, O. A. Marina, C. M. Wang, L. Saraf, V. Shutthanandan, D. E. McCready, A. El-Azab, J. E. Jaffe, M. H. Engelhard, C. H. F. Peden, and S. Thevuthasanc, *Appl. Phys. Lett.* **2005**, *86,*131906.

[7] N. Schichtel, C. Korte, D. Hesse and J. Janek, *Phys. Chem. Chem. Phys.*, **2009**, *11*, 3043.

[8] C. Korte, A. Peters, J. Janek, D. Hesse, N. Zakharov, *Phys. Chem. Chem. Phys.*, **2008**, *10*, 4623.

[9] A. Peters, C. Korte, D. Hesse, N. Zakharov, J. Janek, *Solid State Ionics* **2007,** *178*, 67.

[10] E. T. Park and J.-H. Park, in *Proceedings of the 3rd International Meeting of Pacific Rim Ceramic Societies*, Kyungju, Korea, **1998**, http://www.osti.gov/servlets/purl/656718-lsmLVa/webviewable/.

[11] H. M. Kandil, J. D. Greiner and J. F. Smith, *J. Am. Ceram. Soc.*, **1984**, *67*, 341.

[12] C. A. Tracy and G. D. Quinn, in *Ceramic Engineering and Science Proceedings*, ed. K. Logan, American Ceramic Society, **1994**, 15, 837.

[13] J. Garcia-Barriocana, A. Rivera-Calzada, M. Varela, Z. Sefrioui, E. Iborra, C. Leon, S. J. Pennycook, J. Santamaria, *Science* **2008**, *321*,676.

[14] M. Ahrens, R. Merkle, B. Rahmati, J. Maier, Phys. B **2007**, *393*, 239.

[15] S. Sanna, V. Esposito, D. Pergolesi, A. Orsini, A. Tebano, S. Licoccia, G. Balestrino, E. Traversa, *Adv. Funct. Mater* **2009**, *19*, 1713.

[16] X. Guo, *science*, **2009,** *34*, 465.

Chapter 2

Fabrication and characterization of thin films for SOFC applications

2.1 Fundamentals of Pulsed Laser Deposition

Pulsed Laser Deposition (PLD) is excellent and simple among all thin film growth techniques. A high power laser is used as an external energy source to vaporize materials and to deposit thin films. A set of optical components is used to focus the laser beam over the target. Film growth can be carried out in an ultra high vacuum chamber and in reactive gas (for example oxygen or nitrogen gasses). When the laser radiation is absorbed by the target, electromagnetic energy is converted into electronic excitation and then into thermal, chemical, and even mechanical energy to cause evaporation, ablation, excitation, and plasma formation. Evaporants form a "plume" consisting of a mixture of energetic species including atoms, molecules,

electrons, ions and clusters. The advantages of this technique are flexibility, fast response and that the thin films are of the same stoichiometry as the target [1]. The major disadvantage is the presence of micro-sized particulates on the substrates. Figure 1 shows a schematic diagram of an experimental setup.

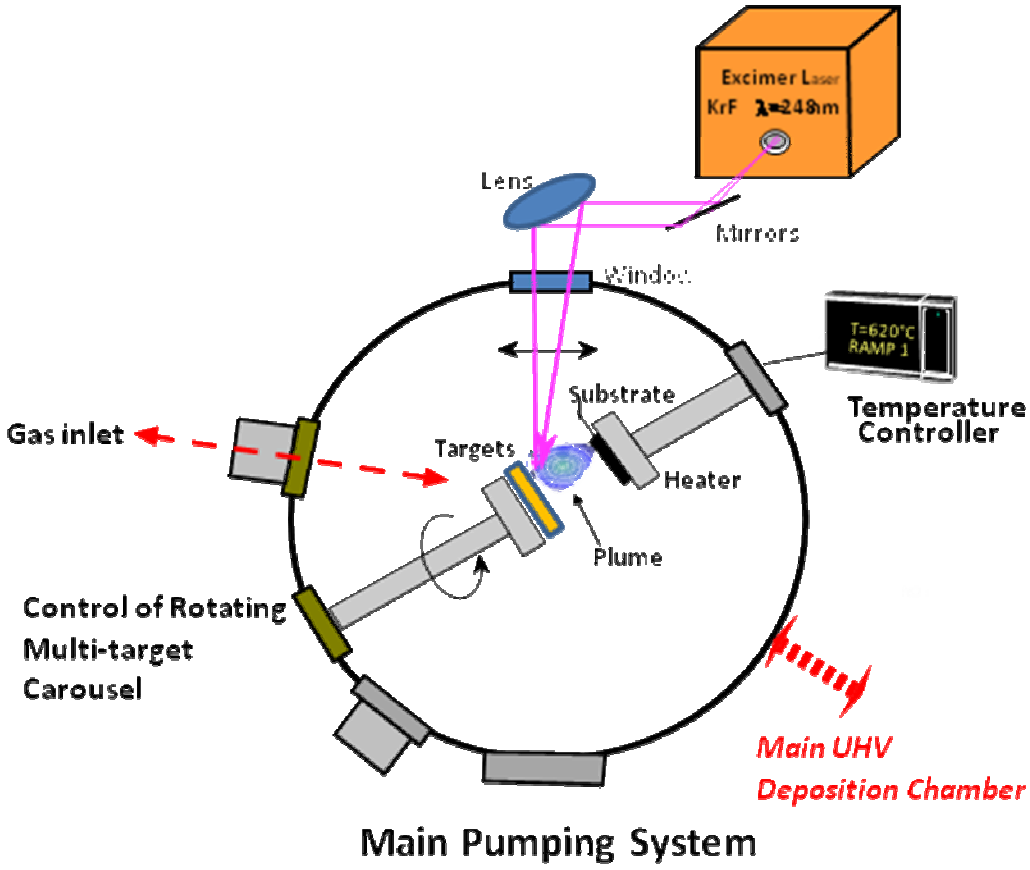

Figure 1. Schematic diagram of PLD experimental setup.

2.2 Deposition systems

Laser. In general, the useful range of laser wavelengths for thin-film growth by PLD lies between 200 nm and 400 nm. Most materials used for deposition work exhibit strong absorption in this spectral region. A typical laser used for PLD is excimer

laser. In fact, KrF (used in our laboratory), with a wavelength of 248 nm and XeCl with a wavelength of 222 nm, are the popular choices among PLD community. The light output from an excimer laser is derived from an excited gaseous mixture. When the excimer molecules are produced from electric discharge excitation, they decay via spontaneous emission and collisional deactivation giving the molecules a life time of 2.5 ns. Our thin films were grown with a KrF excimer laser (Lambda Physik LPX) with a wavelength of 248 nm and a pulse width of 25 ns. The laser fluence was set at approximately 5 J/cm^2. The laser repetition rate was 10 Hz. The targets used for deposition were SDC and YSZ. The SDC target was prepared using $(CeO_2)_{0.8}(Sm_2O_3)_{0.2}$ powders synthesized in our laboratory using a direct coprecipitation method. The YSZ target was prepared using (ZrO_2):8 mol % Y_2O_3 commercial powder. Cylindrical pellets were fabricated by uniaxially cold-pressing the powder at 140 MPa and sintering it at 1450°C for 10 h.

The deposition chambers. The deposition chamber is one of the most important components in a PLD system. The chamber is usually equipped with a multi-target rotating holder, allowing a fast switch of the target during the deposition. Other features include a heater, lenses, windows, gas inlet and ultra-high vacuum equipment to ensure a base pressure of 10^{-8} mbar. The distance between the substrate and the target is about 25 mm. Figure 2 shows a photo of the chamber used in our laboratory.

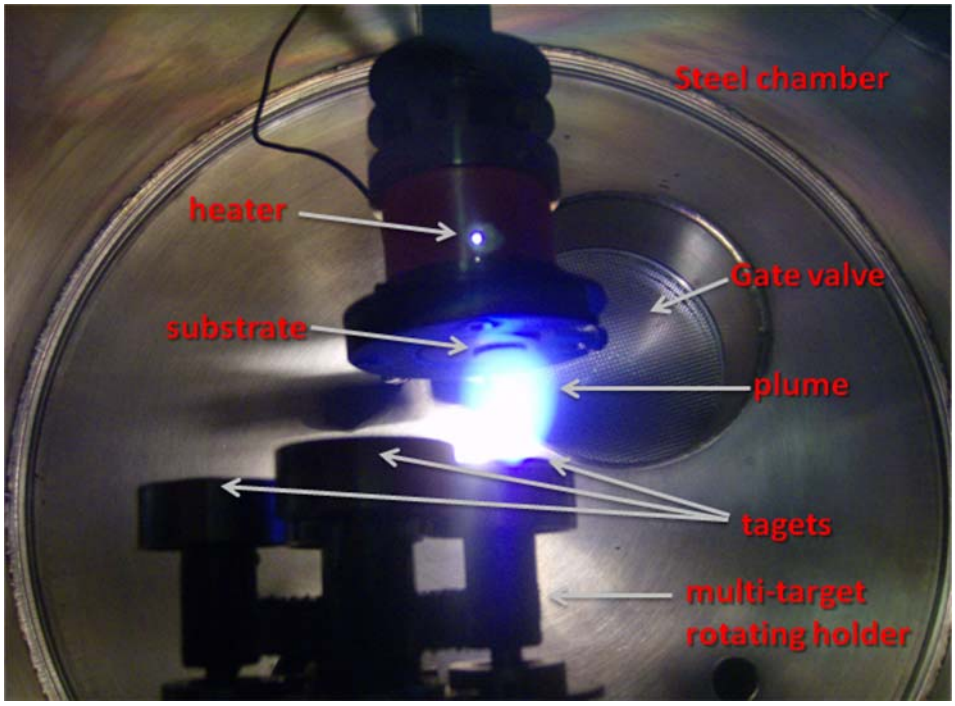

Figure 2. Photo of the chamber used in our laboratory. The distance between the substrate and the target is about 25mm.

One of the great advantages of PLD is the ease with which in situ multilayer structures and superlattices can be formed. In fact, a multi-target carousel containing several targets can be used in deposition chamber (see fig.2).

Substrate holders and heaters. Usually, the substrate must be heated to produce good adhesion and epitaxy. For our epitaxial thin films deposited by PLD, substrate temperatures of 600°C must be maintained in ambient oxygen (from 10^{-3} to 10^{-1} mbar). On the contrary, porous thin films were deposited at room temperature and annealed after the PLD deposition.

Vacuum equipment. One of the advantages of PLD, as compared to other film deposition techniques, is that a PLD system needs a relatively simple and economical

pumping and gas flow systems. Our systems consist of a turbo molecular pump for high vacuum (~ 10^{-8} mbar) and rotary pump for pre-vacuum (~ 10^{-3} mbar). Vacuum gauges were used to check the pressure inside the chamber during the deposition.

2.3 X-Ray Diffraction technique for structural characterization of thin films

The X-ray diffraction technique reveals information about the crystallographic structure of materials and thin films. The basis of diffraction analysis is wave interference: X-ray wavelengths are comparable with inter-atomic distances of the crystal. The interference is constructive when the phase shift is a multiple of 2π, in accordance with Bragg's law:

$$n\lambda = 2d\sin\theta \qquad (1)$$

where n is a integer, λ is the wavelength of the incident radiation, *d* is the spacing between the planes in the atomic lattice and θ is the angle between the incident ray and the scattering planes [2].

Rocking curve. From the rocking curve (RC) it is possible to estimate the film mosaic spread. In the RC procedure, the detector is positioned at the 2θ Bragg position while the angle between the incident ray and the surface of the sample is moved around the Bragg's angle θ (fig.3).

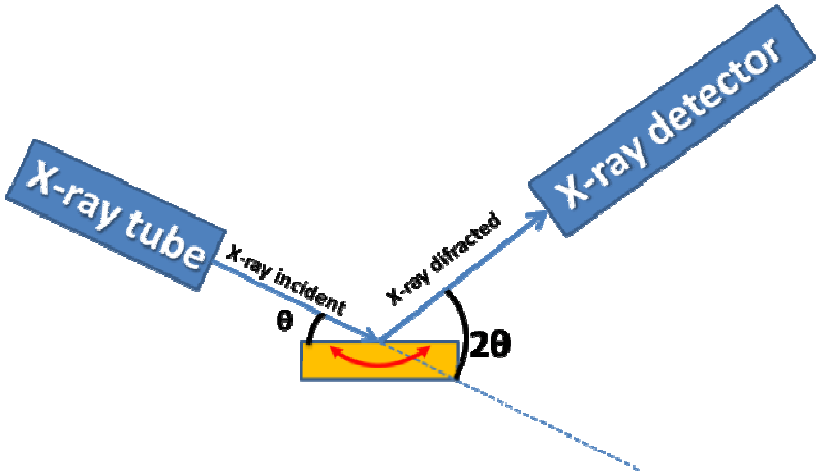

Figure 3. Rocking curve experimental setup.

From the value of Full Width at High Maximum (FWHM) we can understand how grains are tilted in the film. For this reason a lower value of FWHM means a higher quality of the crystal and lower disorder of the films (fig.4a).

Reciprocal Space Maps. Reciprocal space maps (RSMs), consisting of a series of RC's, show the distribution of the diffracted X-rays in reciprocal space (RS) in a two dimensional way. Different distortions of a perfect crystal or a heterostructure can be identified by their characteristic shape in RS [2-5]. By RSM we can understand the strain status: the relative positions of the reciprocal lattice points reflect the strain status of the layers and the plane tilts (fig.4b).

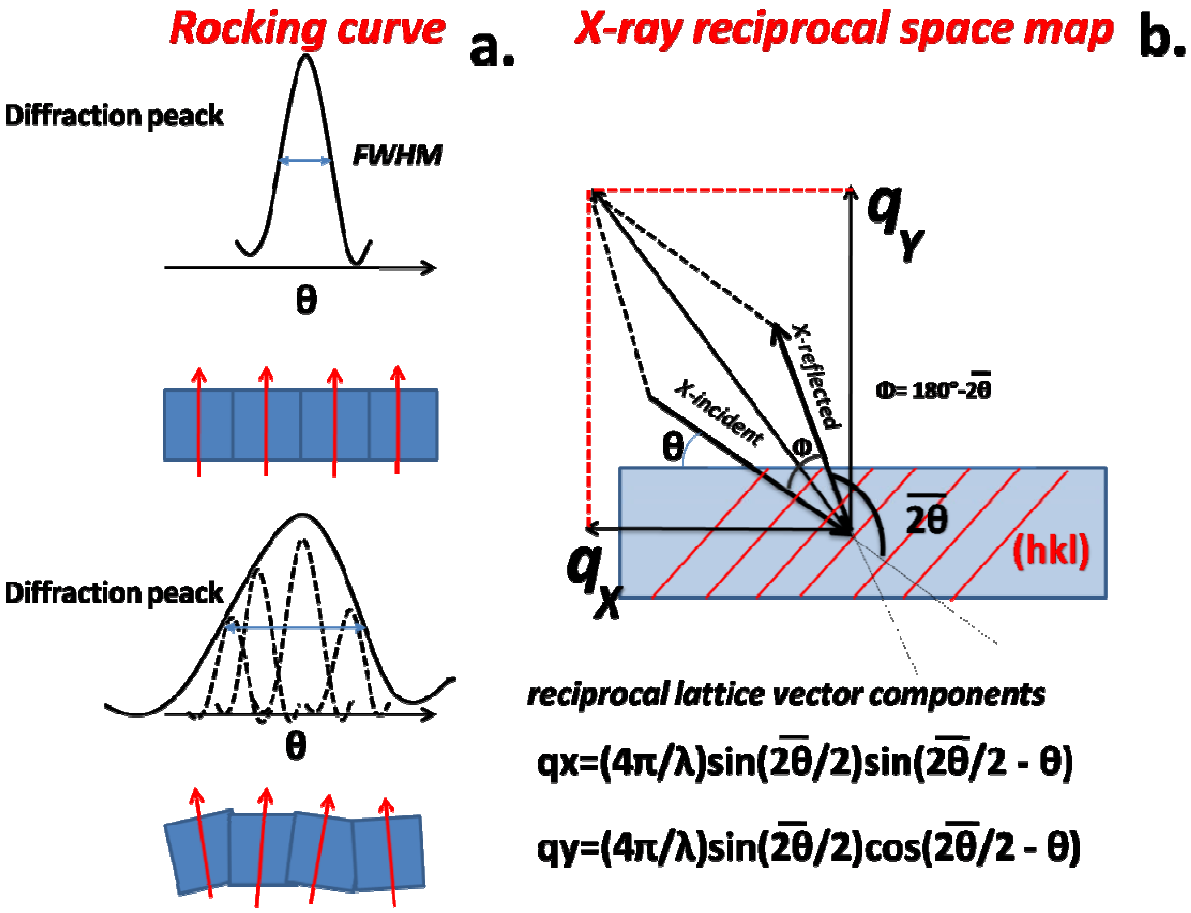

Figure 4. Representation of the rocking curve (a) and reciprocal space maps (b).

From the angular positions of the layer peaks in the asymmetric map [2-5], the reciprocal lattice vector components q_x and q_y parallel and perpendicular to the film surface respectively are:

$$q_x = \frac{4\pi}{\lambda}\sin(\frac{\overline{2\theta}}{2})\sin(\frac{\overline{2\theta}}{2} - \theta)$$

$$q_y = \frac{4\pi}{\lambda}\sin(\frac{\overline{2\theta}}{2})\cos(\frac{\overline{2\theta}}{2} - \theta) \qquad (3)$$

For the asymmetrical *(hkl)* reflection the reciprocal lattice vector components depend on the in-plane lattices constant a_p and the perpendicular to the film surface a_n (for a cubic compound):

$$q_x = 2\pi\sqrt{h^2 + k^2} / a_p$$

$$q_y = 2\pi\sqrt{l^2} / a_n \qquad (4)$$

2.4 Electrochemical characterization: Electrochemical Impedance Spectroscopy (EIS)

Impedance spectroscopy (IS) is powerful method for characterizing many of the electrical properties of materials and their interfaces with electronically conducting electrodes. It may be used to investigate the dynamics of bound or mobile charge in the bulk or interfacial regions of any kind of solid or liquid material: ionic, semiconducting, mixed electronic–ionic, and even insulators (dielectrics). The most common and standard approach to using the EIS technique is to measure impedance by applying a single-frequency voltage or current to the interface and measuring the phase shift and amplitude, or real and imaginary parts, of the resulting current at that frequency using either an analog circuit or fast Fourier transform (FFT) analysis of the response. Commercial instruments (for example the solartron used in our laboratory) are available which measure the impedance as a function of frequency automatically in the frequency ranges of about 1mHz to 10MHz.

Any intrinsic property that influences the conductivity of electrodes, electrolytes and in particular solid oxides fuel cell systems can be studied by EIS. The parameters derived from an EIS spectrum fall generally into two categories: (a) those pertinent only to the material itself, such as conductivity, dielectric constant, mobility of charges, equilibrium concentrations of the charged species, and bulk generation–recombination rates; and (b) those pertinent to an electrode–material interface, such as adsorption–reaction rate constants, capacitance of the interface region, and diffusion coefficient of neutral species in the electrode itself [6].

A signal $V(t) = V_m \cdot \sin \omega t$ where $\omega = 2\pi f$ is applied to a cell and the resulting state current $i(t) = I_0 \cdot \sin(\omega t + \theta)$ measured. θ is the phase difference between the voltage and the current. The impedance of the electrochemical system is $\vec{Z} = \frac{\vec{V}}{\vec{i}}$. Now we can write the impedance as a complex function of ω :

$$\vec{Z}(\omega) = \left|\vec{Z}(\omega)\right| \cdot \exp(j\phi) = \mathrm{Re}\left[\vec{Z}(\omega)\right] + j \cdot \mathrm{Im}\left[\vec{Z}(\omega)\right] = Z' + jZ''$$

where $j = \sqrt{-1}$. The impedance is a vector quantity and may be plotted in the plane with either rectangular or polar coordinates, as shown in Figure 5.

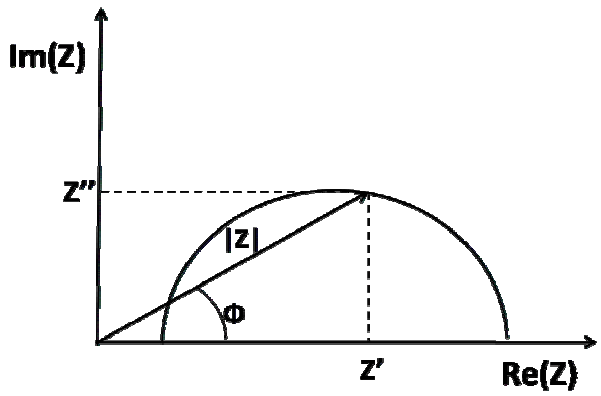

Figure 5. The impedance *Z* plotted as a planar vector using rectangular and polar coordinates.

The interpretation of a spectrum of impedance is based on its comparison with a model defined *"equivalent circuit"*[6].

Properties of equivalent circuits:

- The spectrum of the equivalent circuits must be similar to the system under investigation
- Each element (for example R or C) must be associated with the electrochemical process in the system under investigation.
- The number of elements should be as low as possible

The main elements of equivalent circuits are shown in table 1:

Element	Symbol	Impedance	Nyquist plot
Resistance	R	$\vec{Z} = R$	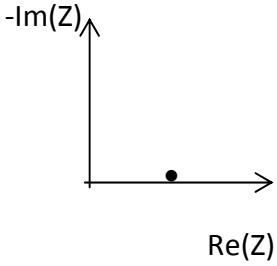
Capacitance	C	$\vec{Z} = -\frac{j}{\omega C}$	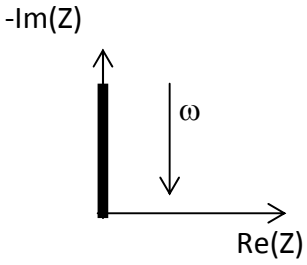
Inductance	L	$\vec{Z} = j\omega L$	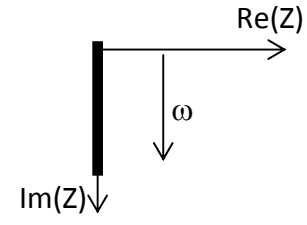

Phase costan elements	CPE	$\vec{Z} = A(j\omega)^{-\alpha}$	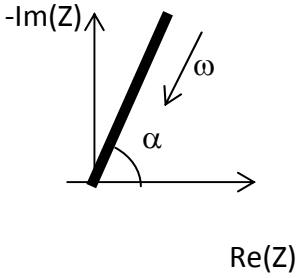
Warburg impedance (relative to the diffusion)	W_∞	$\vec{Z} = R_W \frac{1-j}{\sqrt{\omega}}$	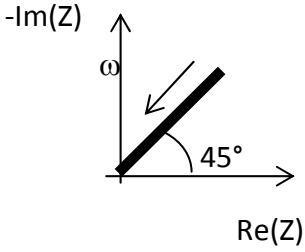
Warburg impedance (relative to the diffusion across the thin film with no blocking interfaces)	W	$\vec{Z} = R_W \frac{\tanh\sqrt{j\omega\frac{\delta^2}{D}}}{\sqrt{j\omega\frac{\delta^2}{D}}}$	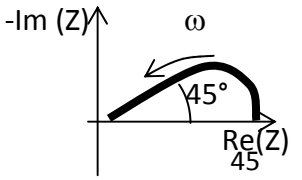
Warburg impedance (relative to the diffusion across the thin film with blocking interfaces)	W_b	$\vec{Z} = R_W \frac{\coth\sqrt{j\omega\frac{\delta^2}{D}}}{\sqrt{j\omega\frac{\delta^2}{D}}}$	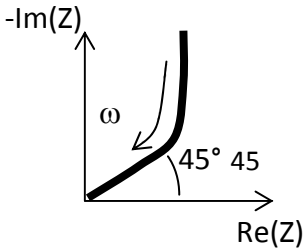

	RC serie	RC parallel
Circuit	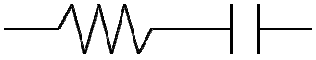	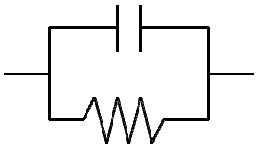
Equation	$\vec{Z} = R - \frac{j}{\omega C}$	$\vec{Z} = \left(\frac{1}{R} + j\omega C\right)^{-1}$
Nyquist plot	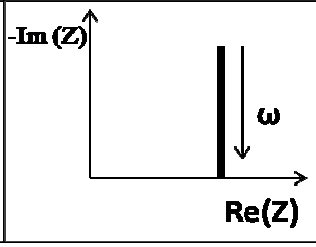	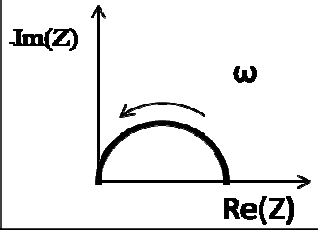

Table1

2.5 Defects in Oxides

Oxides used for SOFC applications, depend on the types, concentrations and mobilities of the ionic and electronic defects. The defects prevalent in an oxide depend strongly on oxygen partial pressure. In this thesis, we focused on transport mechanisms of doped ceria, because cerium cations are reduced from Ce^{4+} to Ce^{3+} at high temperatures and low oxygen partial pressures, resulting in a *n*-type semiconducting behavior [7]. The electronic contribution to conductivity is known to lead to a drastic decay of SOFC performance and for this reason it is important to know the behavior of the SDC electrolyte at low oxygen partial pressure. Defect concentrations are correlated with Brouwer diagrams (see fig.6). At the stoichiometric composition, the concentration of oxygen vacancies and oxygen

interstitials must be equal. At high oxygen partial pressures, excess oxygen can be incorporated through the formation of excess oxygen interstitials. At low oxygen partial pressures, a deficiency in oxygen content can be accommodated through the formation of excess oxygen vacancies [8]. The concentrations of electronic defects are also dependent on oxygen partial pressure from the equations:

$$\frac{1}{2}O_2(gas) + V_O^{\bullet\bullet} + 2e' = O_o$$

$$K = \frac{[O_O]}{P_{O_2}^{1/2}[V_O^{\bullet\bullet}]n^2} = \frac{1}{P_{O_2}^{1/2}[V_O^{\bullet\bullet}]n^2} \quad (5)$$

At low oxygen partial pressure, the concentrations of electrons (n) and oxygen vacancies are much larger than those of any other defect, so the charge neutrality requires:

$$2[V_O^{\bullet\bullet}] = n \quad (6)$$

In which case:

$$n = (2/K)^{1/3} P_{O_2}^{-1/6} \quad (7)$$

In intermediate oxygen partial pressures, where the concentration of intrinsic anion Frenkel pairs $(V_O^{\bullet\bullet} + O_i'')$ is high, the concentration of oxygen vacancies is much larger than the concentration of electrons, so Equation 7 becomes:

$$K = \frac{[O_O]}{P_{O_2}^{1/2}[V_O^{\bullet\bullet}]n^2} = \frac{1}{P_{O_2}^{1/2}[V_O^{\bullet\bullet}]n^2} \Rightarrow n = (2/K[V_O^{\bullet\bullet}])^{1/2} P_{O_2}^{-1/4} \quad (8)$$

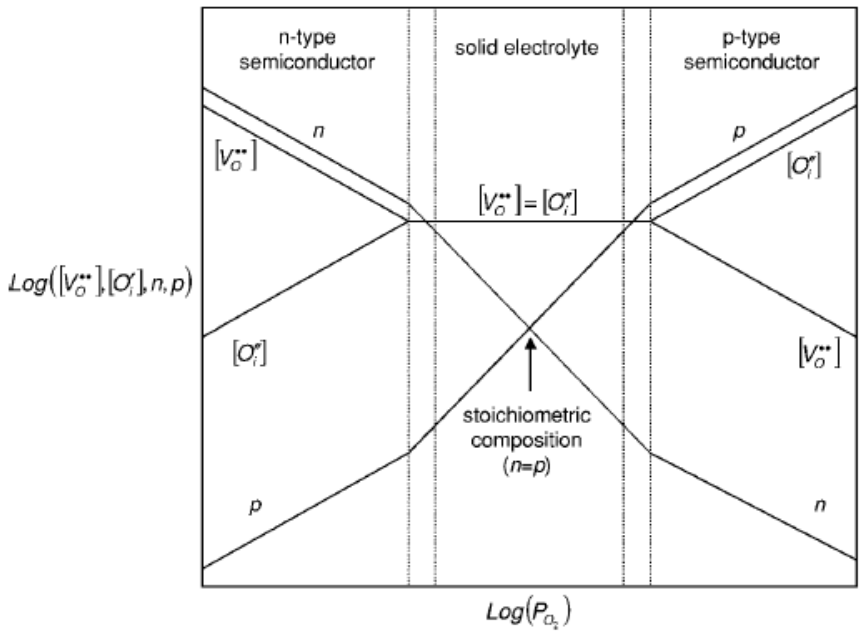

Figure 6. Brouwer diagrams.

In general, the exponents in the equations 7 and 8, with slope= -1/4 or slope= -1/6 in the logarithmic scale in the Brouwer diagram, are important for understanding the reduction mechanisms in doped and un-doped oxides [12].

The different regions in the Brouwer diagram are useful for different types of sensors and electrolytes. Oxides for SOFC applications require that the ionic conductivity, represented in the Brouwer diagram by the region where $[V_O^{\bullet\bullet}] = [O_i'']$ in the fig 6, is much higher than the electronic conductivity, and thus would be used in intermediate oxygen partial pressures in the region labeled "solid electrolyte" in figure 6. Often the dopants are added to increase the concentration of ionic defects and extend the range over which the oxide is electrolyte [7-8]. For example in this thesis ceria oxide (CeO_2) doped with samarium (SDC) or gadolinium (GDC) and

zirconia doped with yttria (YSZ) were characterized at high, intermediate and low oxygen partial pressure. The reactions of these materials are:

$$R_2O_3 = 2R'_Z + 3O_O^X + V_O^{\cdot\cdot}$$

$$R = Y, Gd, Sm; Z = Zr, Ce$$

From equation 7 and 8, the oxygen partial pressure dependence for conductivity of semiconducting oxide is in the form:

$$\sigma = KP_{O_2}^{1/m} \qquad (10)$$

where *m* can vary from -4 to -6.

2.6 Experimental setup for EIS

In this thesis, the AC impedance spectroscopy measurements were carried out for thin films deposited onto insulating substrates in two point configuration with electrodes deposited onto the film surfaces. We measured the parallel conductivity perpendicular to the growth direction and parallel to the interfaces (figure 7a).

The electrodes deposited onto electrolyte were characterized in sandwich configuration (figure 7b).

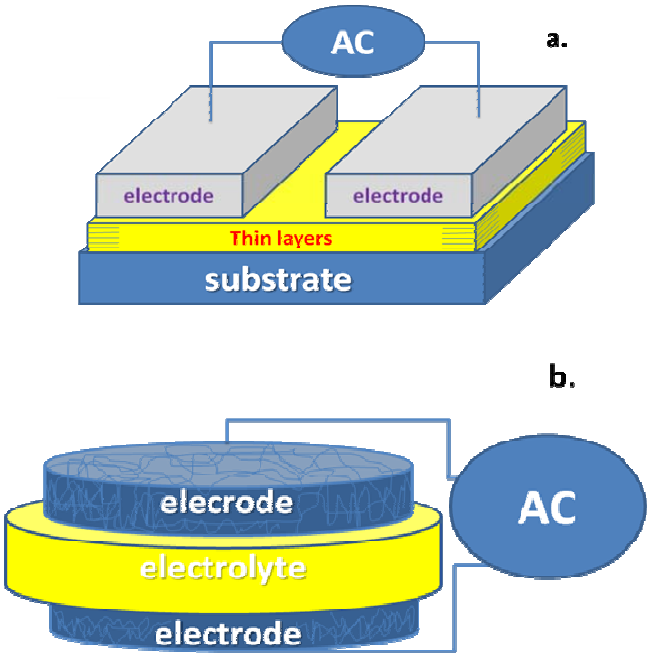

Figure 7. typical two-point electrode configuration for AC impedance spectroscopy: a for thin films deposited onto single crystal substrates, b for porous electrodes deposited onto electrolytes.

EIS measurements were performed in plane configuration using a frequency response analyzer (FRA, Solartron 1260), coupled with a dielectric interface (Solartron 1296), in the 400–800°C temperature range and in the 0.01 Hz - 10 MHz frequency range, with a 100 mV alternate current signal. Transverse impedance measurements were not carried out because the thin films were deposited onto single crystals substrates. Zview® (shareware version) software was used to fit the EIS data. Electrical conductivity measurements of the films were carried out in the 10^{-25} - 1 atm pO_2 range. Air, pure oxygen, argon, and 5% hydrogen-argon dry mixtures were used to vary pO_2. Total gas flow was 150 sccm. Flow rates were controlled by digital flow-meters (MKS). The oxygen concentration was measured using two oxygen sensors/pumps (Zyrox) placed at gas inlet and outlet, respectively. Figure 8 shows a

schematic setup for the two point conductivity measurements as a function of the temperature and oxygen partial pressure.

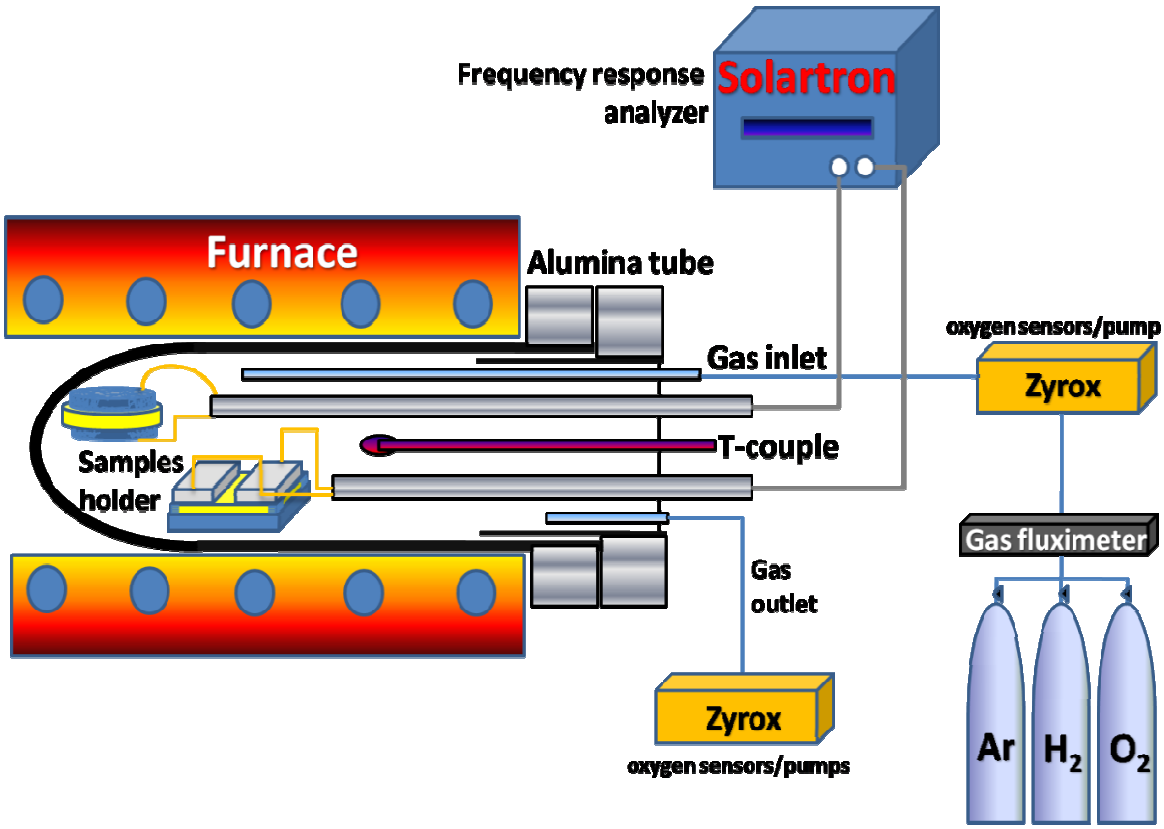

Figure 8. Schematic setup for the two point conductivity measurements as a function of the temperature and oxygen partial pressure.

References

[1] Douglas B. Chrisey, Graham K. Hubler, Pulsed Laser Deposition of Thin Films, *John Wiley & Sons, Inc., Publication.*

[2] G. Bauer, J. Li, E. Koppensteiner, J. Crystal Growth, **1995**, *157*, 61.

[3] P.F. Fewster, Appl. Phys. A, 1994, 58, 121.

[4] B.K. Tanner, in: Analysis of Microelectronic Materials and Devices, Eds. M. Grasserbauer and H.W. Wemer (Wiley, New York, 1991) 609.

[5] E. Koppensteiner, G. Bauer. H. Kibbel and E. Kasper, J. Appl. Phys., **1994,** *76*, 3489.

[6] Evgenij Barsoukov, J. Ross Macdonald, Impedance Spectroscopy Theory, Experiment, and Applications, *John Wiley & Sons, Inc., Publication.*

[7] M. Mogensen, N.M. Sammes, G.A. Tompsett, *Solid State Ionics* **2000**, *129*, 63.

[8] J.W.Fergus *j. Of mater. Science* **2003**, ***38,*** 4259.

Chapter 3

Structural and electrochemical characterization of epitaxial Samarium-doped ceria thin film

3.1 Introduction

The growing demand for miniaturized systems for energy conversion and storage has prompted extensive research aimed at the fabrication of solid state ionic devices in thin film form. Electrochemical devices, such as solid oxide fuel cells (SOFCs), can be miniaturized for portable applications (μ-SOFCs) [1]. This goal requires the reduction of the operating temperature and the production of components as thin films [2-7]. In general, μ-SOFC devices are expected to produce energy densities per volume and specific energy per weight up to four times larger than state-of-the-art rechargeable Li-ion and Ni metal hydride batteries [8].

Samarium and gadolinium doped ceria (SDC, GDC) possess larger ionic conductivity than yttria-stabilized zirconia (YSZ), the conventional SOFC electrolyte material, and are thus intensively studied to achieve the target of reducing SOFC operating temperature in the 600-800 °C range [9-11].

However, doped ceria is a mixed ionic-electronic conductor (MIEC), because cerium cations are reduced from Ce^{4+} to Ce^{3+} at high temperatures and low oxygen partial pressures, resulting in a *n*-type semiconducting behaviour related to the small polaron hopping mechanism [12]. The electronic contribution to conductivity is known to lead to a drastic decay of SOFC performance; however, such contribution is negligible at low temperatures for doped ceria, allowing its use as IT-SOFC electrolyte. Doped-ceria is particularly promising as electrolyte for μ-SOFCs, as demonstrated by the numerous papers recently appeared in the relevant literature investigating doped ceria in thin film form [5, 7, 13-19]. Pulsed laser deposition (PLD) is particularly promising amongst the different film deposition techniques, because of its capability of reproducing the target composition onto the film substrates [20].

3.2 Epitaxial thin films and heterostructures deposited onto single crystal perovskite substrates

Doped ceria films having fluorite structure can be deposited, starting from a polycrystalline target, on several non-fluorite substrates maintaining the correct stoichiometry [19]. In particular, doped ceria has been shown to grow on (001) MgO substrates as well as on (001) $LaAlO_3$ (LAO), (110) $NdGaO_3$ (NGO), and (001)

$SrTiO_3$ (STO) perovskite substrates [14,16]. Perovskite-type substrates provide the proper lattice match for ceria, inducing the growth of epitaxial monocrystalline films with a low degree of structural disorder [16]. The growth condition for SDC on NGO were: oxygen partial pressure in the deposition chamber about 4 x 10^{-3} mbar, the temperature of substrate about 630°C. The laser fluence was set at approximately 5 J/cm^2 with repetition rate of 10 Hz. The distance target substrate was about 2.5 mm.

Figure 1 shows the XRD plots (θ-2θ fig.a and rocking curve fig. b) of Samarium oxide (20 mol%)-doped ceria (SDC) thin film deposited onto NGO single crystal. In the θ-2θ scan of Fig. 1a, only the (002) diffraction peaks from the NGO substrate and the SDC film were detected. This indicated a [001] preferential orientation for the SDC film growth. The rocking curve of the (002) SDC film peak in figure 4b showed a FWHM value of about 0.1°. Small FWHM values demonstrate a very low degree of crystallographic disorder for the deposited film.

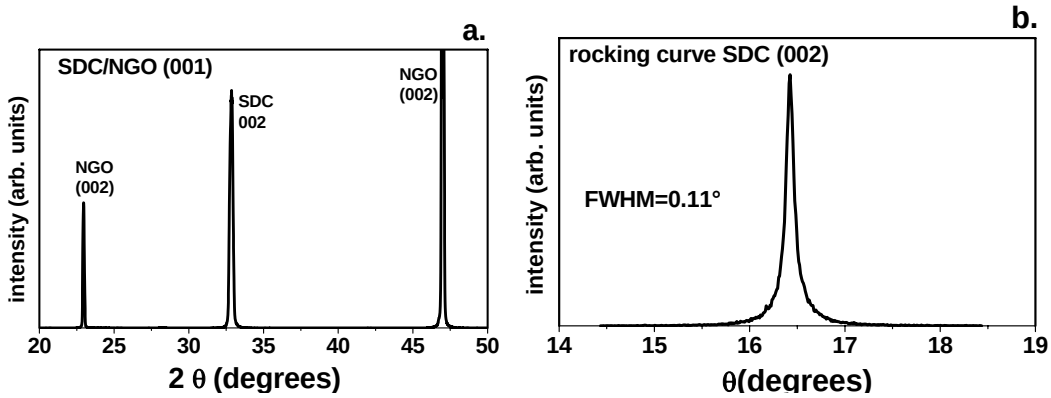

Figure 1. θ-2θ scan (a) and rocking curve (b) of SDC deposited onto NGO perovskite.

Figure 2 shows the XRD plots of tri-layer of LSCF/SDC/LSCF deposited onto STO single crystal substrates deposited at 600°C and 10^{-4}mbar oxygen partial pressure. XRD plots demonstrate a very low mosaic spread for the tri-layers LSCF/GDC/LSCF and LSCF/GDC/ESB/GDC/LSCF.

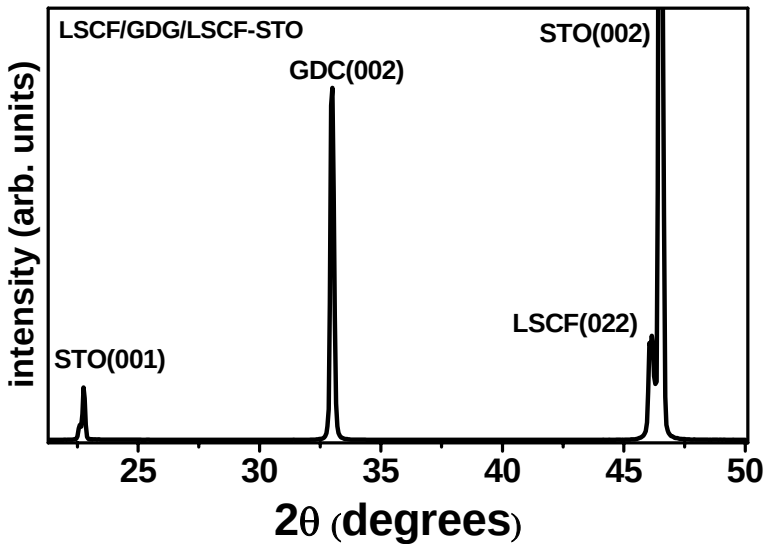

Figure 2. θ-2θ scan of heterostructures of LSFC/SDC/LSCF deposited onto STO

Figure 3 shows a XRD scan of heterostructures of LSCF/SDC/ESB/SDC/LSCF deposited onto STO substrate at the same growing condition of SDC and LSCF/GDC/LSCF deposited onto STO.

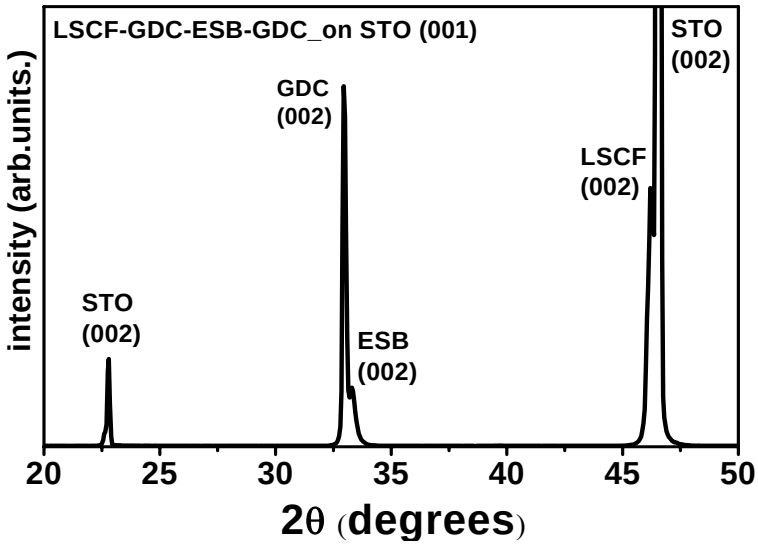

Figure 3. θ-2θ scan of heterostructures of LSFC/GDC/LSCF deposited onto STO. XRD plots (fig.5 and fig.6) demonstrate a very low mosaic spread for the tri-layers LSCF/GDC/LSCF and LSCF/GDC/ESB/GDC/LSCF.

Figure 4 shows a FE-SEM micrograph of the cross section of tri-layer of LSCF/SDC/LSCF deposited onto STO single crystal substrates after deposition without annealing treatment.

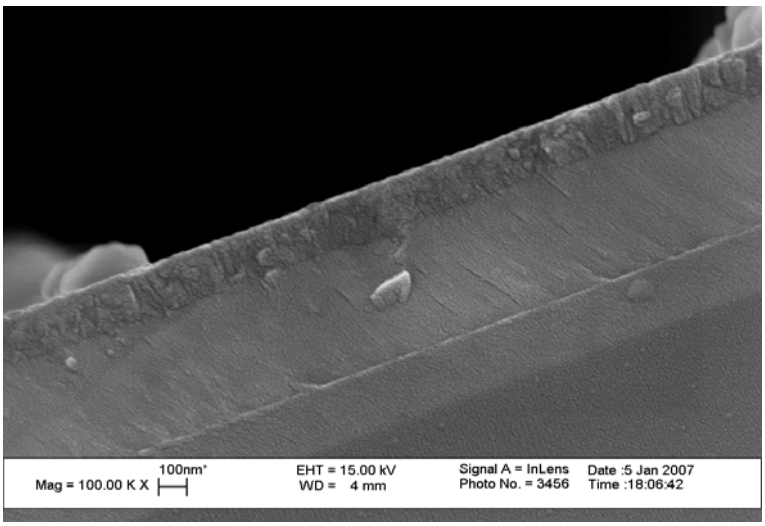

Figure 4. FE-SEM of heterostructures of LSFC/GDC/LSCF deposited onto STO.

Figure 5 shows the top-view of the tri-layers LSCF/GDC/LSCF annealed at 800°C for 12 hours. The morphology confirms a very low mosaic spread for the tri-layers LSCF/GDC/LSCF. Bottom LSCF (fig. 5d and 5c) and GDC (fig. 5c, 5b and 5a) are dense, homogeneous, and continuous and grain boundary regions are not revealed. On the contrary top LSCF layer (fig. 5a) is not dense but it is formed by crystals with size of about 100 nm.

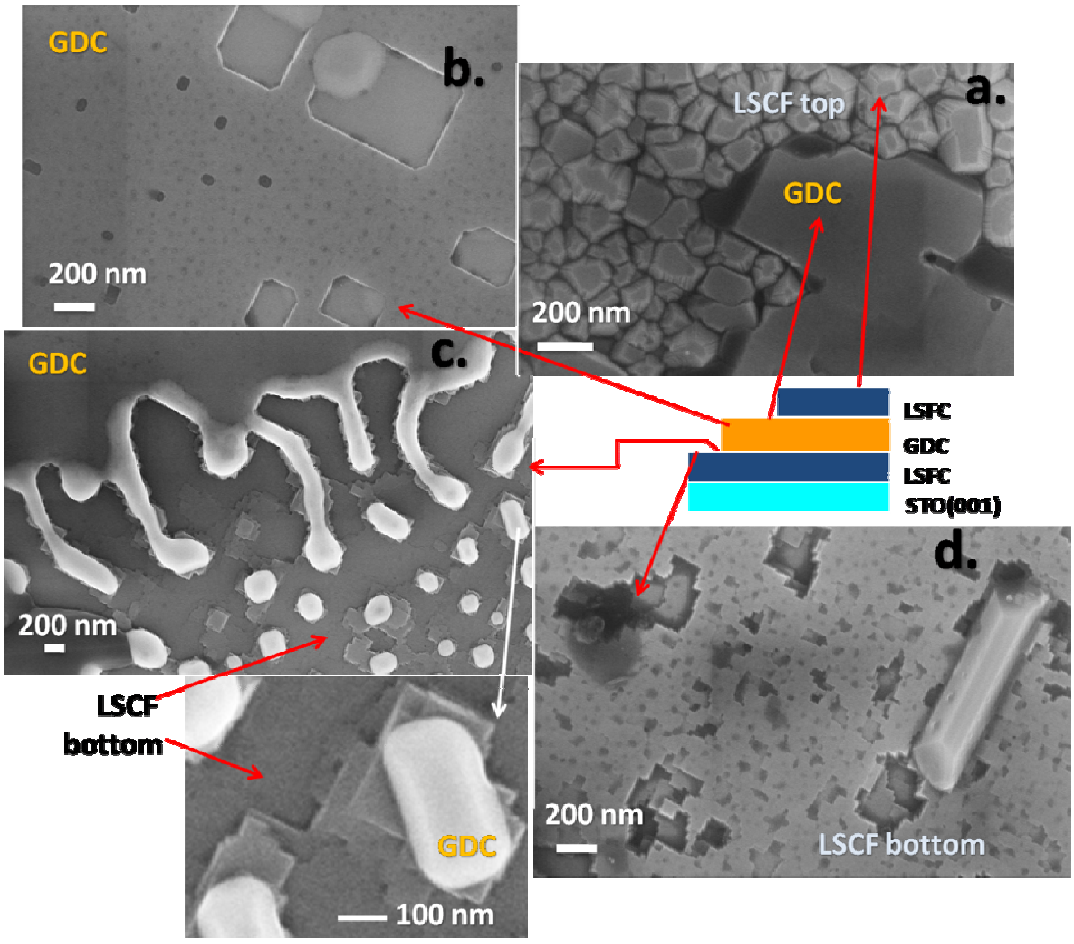

Figure 5. FE-SEM of the surface of LSFC/GDC/LSCF deposited onto STO.

However, perovskite substrates might show electronic, ionic, or mixed ionic-electronic conduction at temperatures above 300 °C, which might affect the proper

evaluation of the electrical measurements performed on ceria films. Namely the electrochemical measurements of SDC/YSZ bi-layer deposited onto STO single crystal (fig.6), with the overall thickness of about 400 nm, shows typical behavior of p-type conductor of perovskite in air and at low pO_2. Figure 6 shows a Brouwer diagram of bi-layer of SDC/YSZ deposited onto STO single crystal. From the total electrical conductivity as a function of oxygen partial pressure in the fig.6 is clearly evident the absence of the contribution of the thin film in the electrochemical measurements. Namely the conductivity, calculated with geometrical factor of the film (overall thickness about 400 nm, about 2 mm distance between the electrodes and 5mm the electrode width normal to the current flow) in the Brouwer diagram exhibits the tipical behaviour of the substrate STO [21, 22].

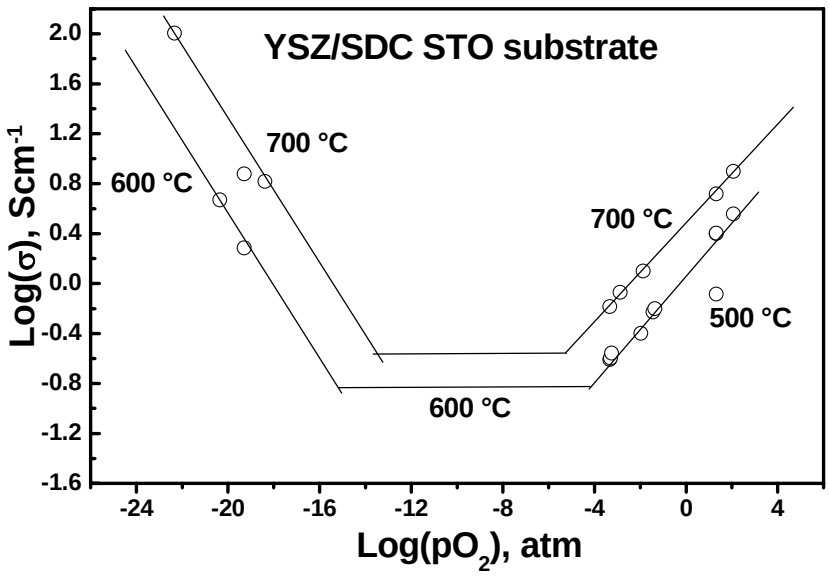

Figure 6. Total electrical conductivity of B-layer SDC/YSZ deposited onto STO substrate as a fuction of oxygen partial pressure.

3.3 XRD characterization of SDC and SDC/STO deposited onto MgO (001) single crystal substrate

MgO, which shows a remarkably low electrical conductivity at high temperatures, does not provide a good lattice match with the ceria fluorite structure, namely the lattice misfit between SDC and MgO is about 8.63%. As a consequence, doped ceria films on MgO show a higher degree of structural disorder, which can result in ionic conduction blocking effects and to contaminant segregation phenomena [13, 23]. To obtain a proper evaluation of the conductivity of epitaxial or single-crystal doped-ceria films, in this work PLD was used to grow highly doped SDC (20% molar samarium oxide) films on (001) MgO single-crystal substrates, using a STO thin film as a buffer layer, taking advantage of the good lattice match between MgO and STO that allows the epitaxial growth of STO films on MgO substrates. A similar approach has been previously used for the deposition of high temperature superconductor thin films onto MgO substrates [24-26]. The SDC/STO/MgO heterostructure was engineered in order to combine the chemical and thermal stability of the insulating MgO substrates with the structural properties of the SDC films grown on the perovskite structures. The STO buffer layer matched well both SDC and MgO. The STO thickness was kept at about 50 nm, introducing a negligible electronic contribution to the overall conductivity of the heterostructure. This allowed for the first time, to the best of our knowledge, the measurement of the ionic conductivity of epitaxially-ordered Sm-doped ceria thin films decoupling any interference from the substrate electronic conductivity.

X-ray diffraction (XRD) analysis showed that the materials used as targets and substrates in the PLD were single phase. The lattice parameters for starting materials, deposited films, and MgO substrates were calculated from XRD analysis, showing a good agreement between the experimental values and those reported in the literature [27-29]. Figure 8 shows the θ-2θ XRD patterns of the SDC/MgO film.

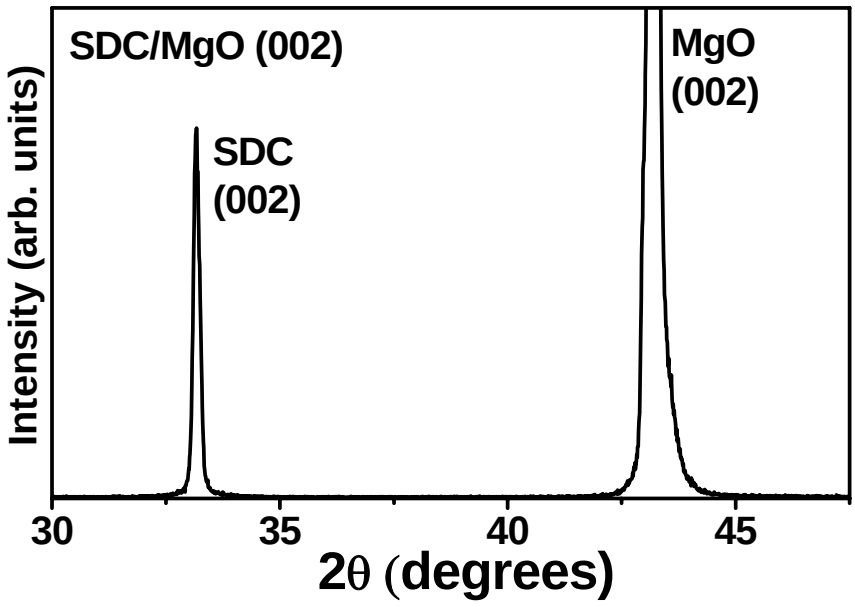

Figure 6. θ-2θ XRD plot of the SDC/MgO.

Figure 7 shows the rocking curves of the (002) diffraction peak for the SDC film deposited on MgO.

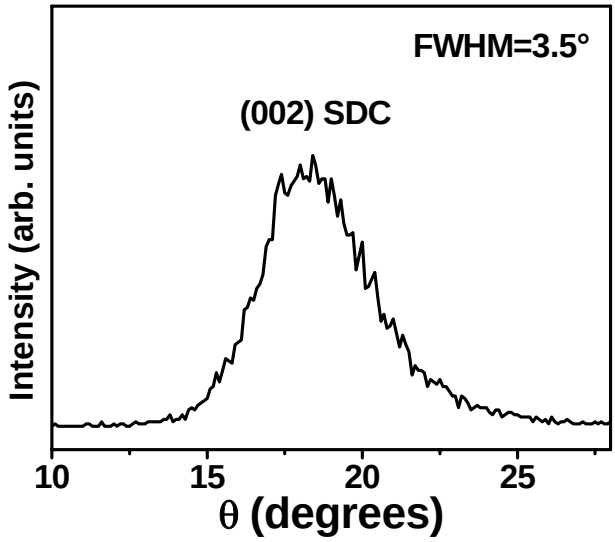

Figure 7. rocking curve of the (002) diffraction peak for SDC/MgO.
In the θ-2θ scan of Fig. 1, only the (002) diffraction peaks from the MgO substrate.

This indicated a [001] preferential orientation for the SDC film growth. The rocking curve of the SDC (002) reflection showed a full width at half maximum (FWHM) value of about 3.5°. Such a large FWHM value demonstrated a rather elevated degree of crystallographic disorder for the SDC film. This result is a consequence of the large lattice misfit of 8.63 % between MgO (a = 4.21 Å) and the SDC20 (a = 5.44 Å) structures. Fig. 8 shows the θ-2θ scan for the SDC/STO/MgO heterostructure: only the (002) diffraction peaks from the MgO substrate, STO buffer layer, and SDC film are visible.

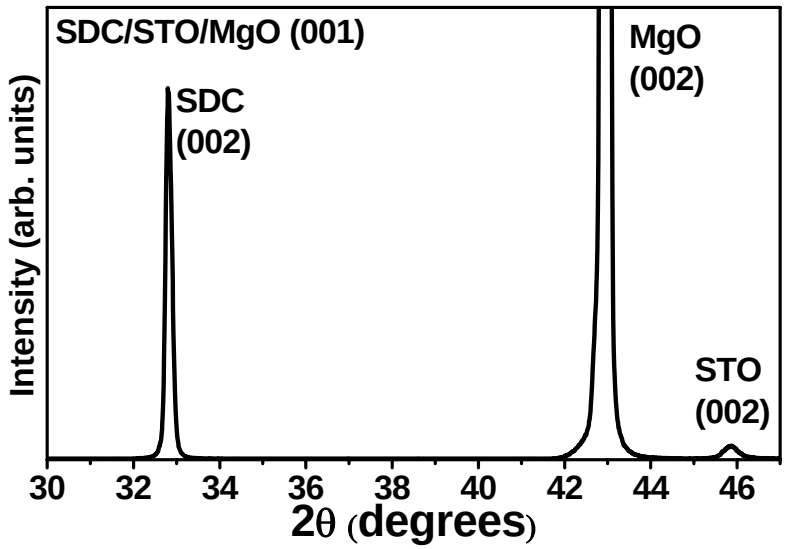

Figure 8. θ-2θ scan for the SDC/STO/MgO heterostructures.

This indicates that both buffer layer and film grew with the [001] axis perpendicular to the substrate surface. Moreover, the rocking curve of the (002) SDC film peak in figure 4 showed a FWHM value of about 0.3°. Small FWHM values demonstrate a very low degree of crystallographic disorder for the deposited film.

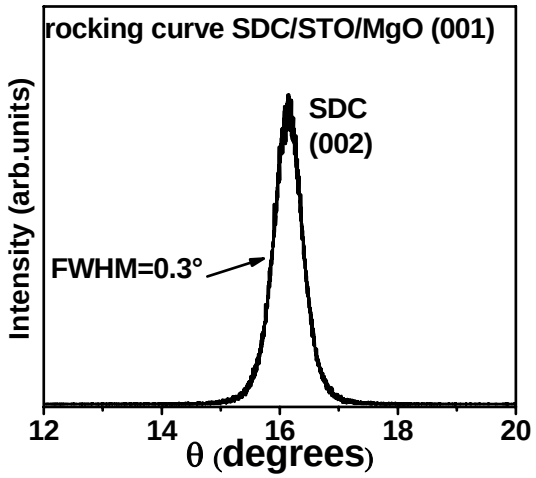

Figure 9. Rocking curve of the (002) diffraction peak for SDC/STO/MgO (001).

Such a result confirmed that the STO (a = 3.91 Å) buffer layer is able to withstand the large lattice mismatch between MgO and SDC with a relatively low number of misfit dislocations at the interface. The epitaxiality relationship among the different layers in the SDC/STO/MgO heterostructure was investigated by the ϕ-scan technique. Figure 10 shows the ϕ–scan XRD of SDC grown on a (001) MgO substrate with a buffer layer of STO.

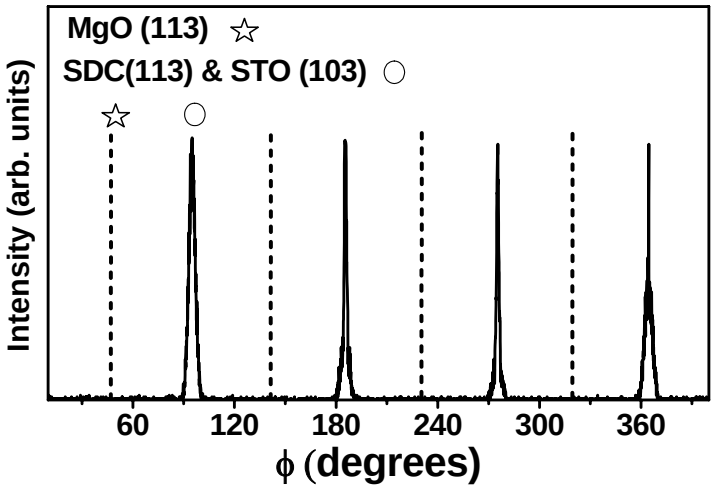

Figure 10. ϕ–scan XRD of SDC grown on a (001) MgO substrate with a buffer layer of STO.

The ϕ-scan of the SDC/STO/MgO heterostructure over 360° was first recorded keeping both the Bragg angle and the incidence angle set at the (113) MgO asymmetric reflection: four peaks having approximately the same intensity and a relative distance of 90° were detected. The same measurement was repeated for the STO and SDC layers. In the case of the STO buffer layer, the (103) asymmetric reflection was used instead of the (113) reflection because of its larger intensity. ϕ-scan of the (103) asymmetric reflection of the thin STO buffer layer showed four

peaks with 45° degree displacements with respect to the (113) MgO peaks (dashed lines in Fig. 10), proving the in plane "cube on cube" match between the two materials. Finally, a ϕ-scan of the (113) SDC reflection was taken, which showed the occurrence of four peaks at the same ϕ-angle values as the STO (103) diffraction peaks. This indicates that the SDC fluorite film grew with a 45° in-plane rotation of the cubic crystallographic axes relative to the orientation of both STO and MgO.

Figure. 13 shows a sketch of the epitaxial relationship between the SDC fluorite structure and the STO perovskite structure, as derived from the data of figure 11.

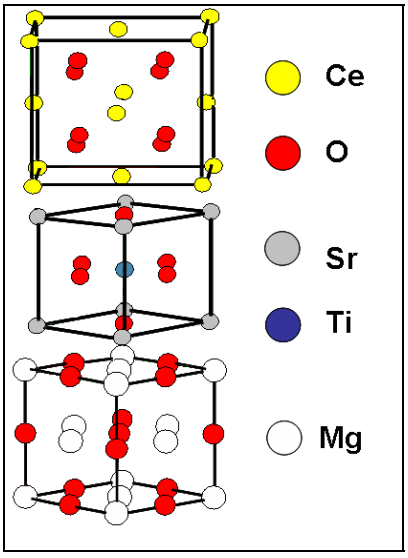

Figure 11. Schematic sketch of the correlation between the cubic cells of SDC, STO and MgO.

The 45° rotation of the SDC fluorite structure with respect to STO can be explained on the basis of simple structural considerations. SDC (fluorite structure) and STO (perovskite structure) have cubic lattice parameters of about 5.44 Å and 3.91 Å, respectively. Therefore, the STO basal diagonal, calculated to be about 5.53 Å, matches quite well the lattice parameter of the SDC fluorite (5.44 Å), with a misfit

percentage value of 1.62 %. Such a value is low if compared with 8.63 % present at the SDC/MgO interface and also to 7.12 % at the STO/MgO interface. XRD measurements taken after a post annealing treatment and measurements showed that the deposited films preserved the crystalline quality observed in figures. 8, 9 and 10. Lattice misfits at the films interfaces between the deposited film and the substrate is a crucial factor for the residual stress formation in the films structure and it is the main cause for a mosaic-spread epitaxial film growth and for their mechanical failure in operative condition [7, 19]. As shown by the XRD analysis, SDC/MgO presented high misfit value which can lead to stress conditions in the SDC film. On the other hand, STO-buffered SDC presented low lattice misfits and low residual stress are expected. The table 1 shows the misfit between SDC and substrates.

Misfit %	MgO	STO
SDC	8.63	1.62

Table 1

3.4 Morphological characterization of SDC and SDC/STO/MgO (001)

Figure 12 shows the FE-SEM micrographs of the cross-sections (fracture surface) and surface-views (in inset) of the SDC/MgO structure post-annealed at 800 °C for 1 hour in air.

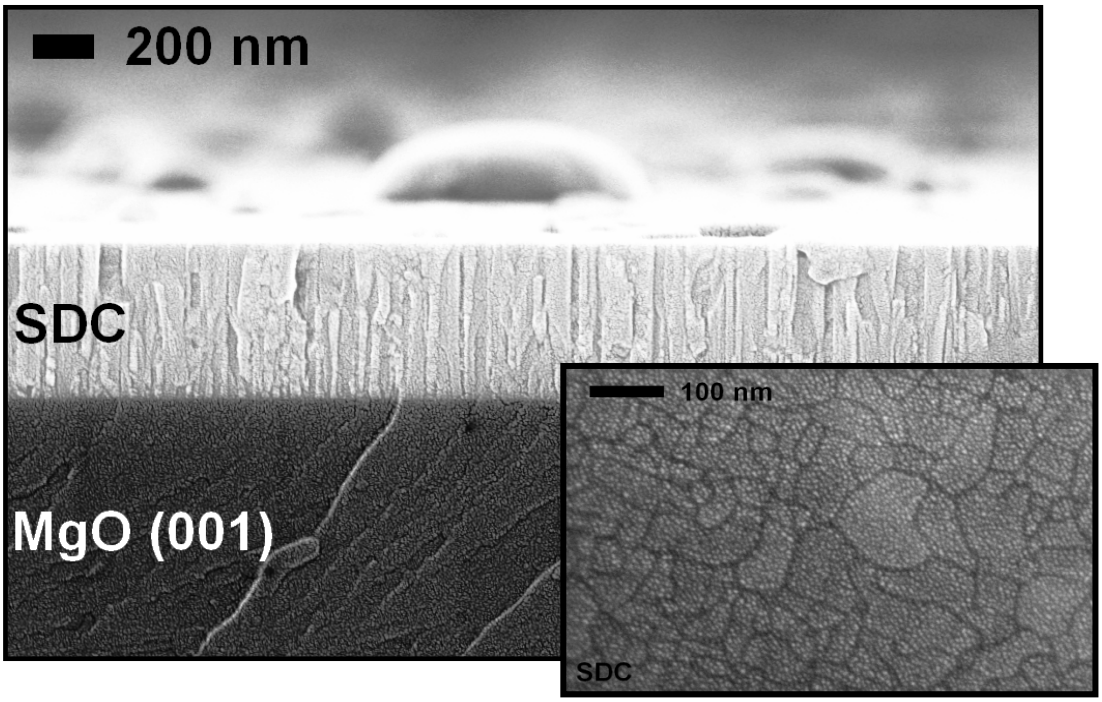

Figure 12. FE-SEM micrograph of cross-section and surface (in inset) of SDC/MgO (001).

Figure 13 shows SDC/MgO (001) tested for several days in reducing-oxidizing conditions in the 400-775 °C range. Figure 13a. shows the cross-section SDC/MgO (001) and figure 8b shows the surfaces of the sample.

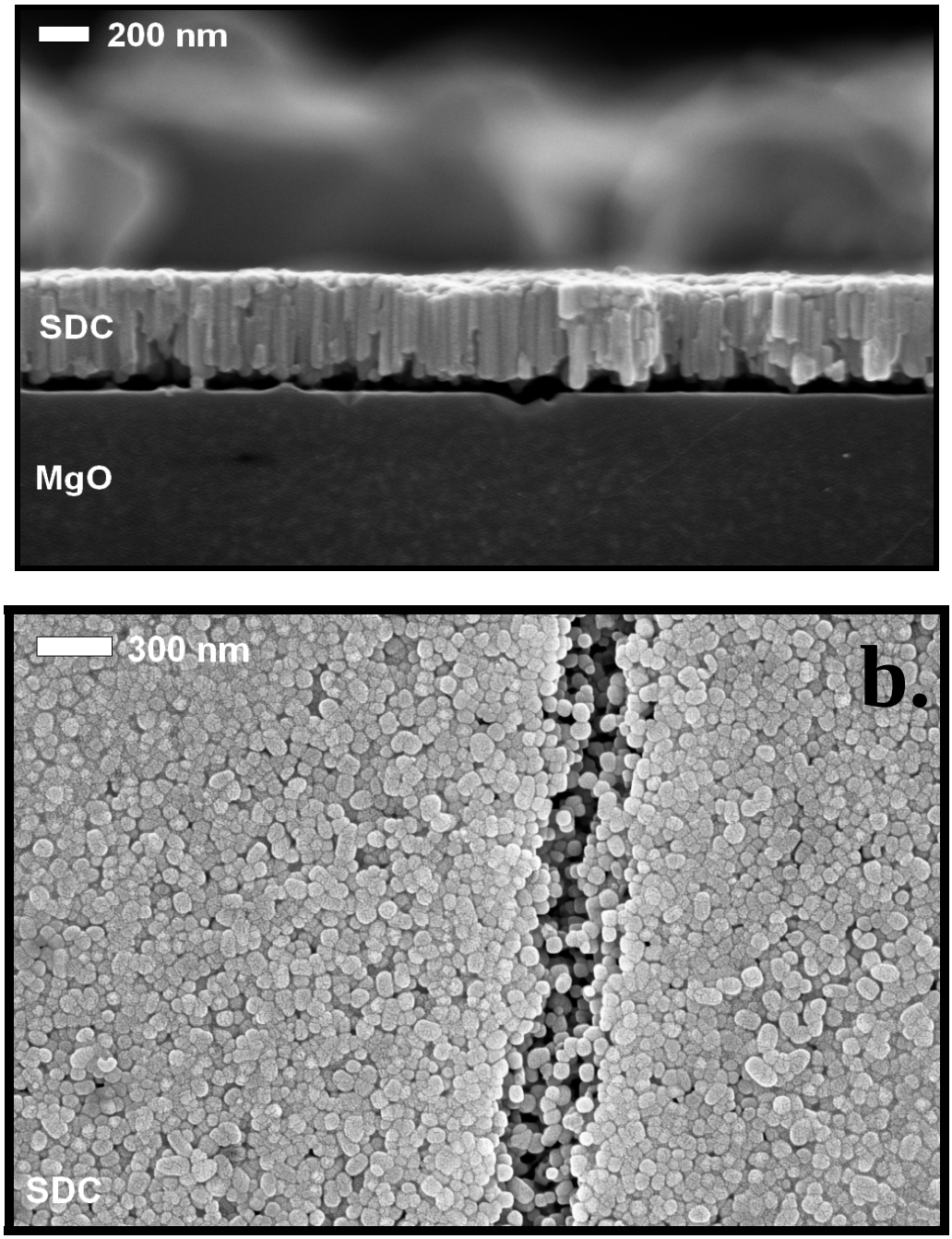

Figure 13. FE-SEM micrograph of the cross-section (a) and surface of the SDC/MgO tested for several days in reducing-oxidizing conditions in the 400-775 °C range.

Fig. 13 shows that the annealed SDC film was dense and homogeneous on the MgO substrate with a columnar morphology. The plan view images (fig. 13) showed a

highly textured columnar structure with a mosaic-spread arrangement in the nanometric scale. Such morphology showed instability during the thermal treatments in hydrogen and oxygen atmospheres. Figure 13a shows that SDC film lost adhesion from the MgO substrate, probably due to stress induced by the lattice misfit between SDC and MgO. However, fig. 13b shows that the columnar grains, in the treated film, changed their morphology from the textured structure (fig. 13) to a cylindrical shape. This evolution occurred with time at temperatures below 800 °C, upon a few oxidation-reaction cycles, and led to the formation of micro-cracks and nanometric porosity (fig. 13b). The microstructural evolution of SDC/MgO samples was explained by the fact that the annealed film (fig.13) presented a high surface energy at the grain boundary and at the SDC/MgO interface. This energy could be released in the diffusive regimes that can be activated also at low temperatures [11]. Despite several papers in the relevant literature reported electrical results obtained for columnar polycrystalline thin films of doped ceria, their long term thermal and chemical stability has been scarcely considered [7]. However, thermal stresses and microstructural evolution for thin films is crucial for μ-SOFC applications, usually subjected to reduction and oxidation cycles at elevated temperatures. Our results clearly showed a marked instability at high temperatures of ceria thin films deposited by PLD after a few red-ox cycles, demonstrating that problems might arise from the fuel cell operation of these films.

Figure 14 shows the FE-SEM micrograph of the cross-section (fracture surface) of the SDC/STO/MgO heterostructure post annealed at 800 °C for 1 hour and measured in the 400-775 °C range in reducing-oxidizing conditions for several weeks. The

SDC and STO films were dense, homogeneous, and continuous, with no delamination at the materials interfaces. The samples were stable even after several red-ox cycles used for the electrical measurements.

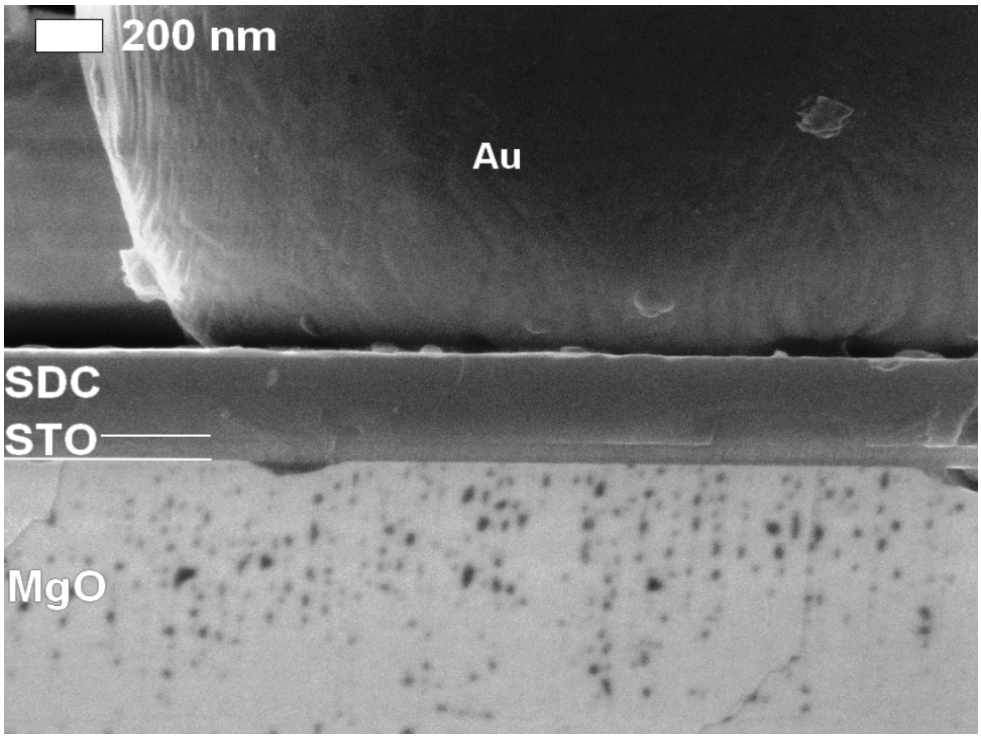

Figure 14. FE-SEM micrograph of the cross-section (fracture surface) of a film of SDC grown on a (001) MgO substrate with an STO buffer layer, post annealed at 800 °C for 1 hour.

Observation of the sample surface morphology and the cross-section did not show the presence of grain boundaries. The thickness of the SDC and STO layers was about 260 and 50 nm, respectively. It is expected that the contribution of the STO buffer layer to the electrical conductivity of the SDC/STO/MgO heterostructure would be negligible because of the relative thicknesses of the SDC and STO layers, estimated by FE-SEM observations. In fact, the electrical conductivity was measured in-plane, by depositing on the SDC film two Au electrodes having a 4 x 5 mm area, at a distance of 0.8 mm. Confirming the fact that the STO buffer layer does not give

a significant contribution to the electrical measurements is the fact that the conductivity of the SDC/STO/MgO and SDC/MgO have the same value before the degradation of SDC/MgO. However, contributions from the STO-SDC interface and from the STO buffer layer must be considered to occur when evaluating the electrical measurements performed in conditions of dominant electronic conduction mechanisms for SDC [30].

3.5 Electrochemical characterization of SDC/MgO (001) and SDC/STO/MgO (001)

Electrochemical impedance spectroscopy (EIS) analysis allows the separation of the electrolyte impedance contribution (at high frequencies) from the electrode impedance contributions (at low frequencies). EIS measurements can be performed using a two electrode configuration, allowing avoiding the use of a reference electrode that is difficult to place in a thin film-shaped sample [31].

Figure 15 shows typical Nyquist (fig.15) and imaginary part of the complex impedance, –Im(Z), measured in air at 700°C, for the post-annealed SDC/STO/MgO and SDC/MgO films.

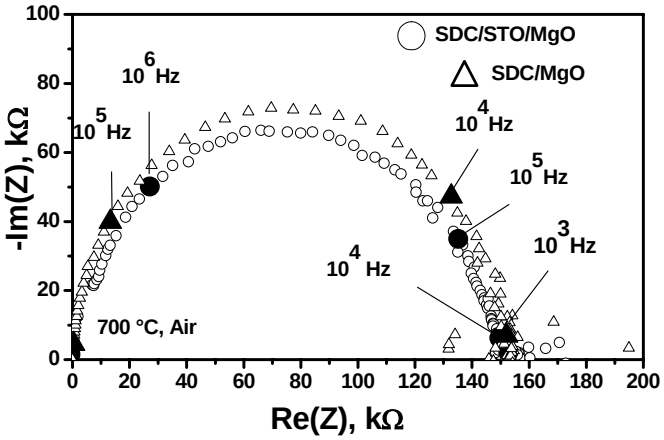

Figure 15. Nyquist (a) and –Im(Z) vs frequency plots (b), measured in air at 700°C, for the post-annealed SDC/STO/MgO and SDC/MgO films.

As is well known [32-33] a semicircle on the complex impedance plot is due to a resistive (R) and a capacitive (C) element in parallel. For both samples, the Nyquist plots exhibited a single semicircle, with a very similar R value of about 150 kΩ.

The SDC/STO/MgO sample did not exhibit grain boundaries and the single semicircle at high frequencies can be ascribed to bulk ionic conductivity.

Usually for polycrystalline ionic conductors, the Nyquist plots typically show two separated semicircles (series of two RC elements in parallel), which are attributed to conduction mechanisms at bulk (high frequency semicircle) and at the grain boundary (low frequency semicircle) [12]. In some circumstances, those two semicircles might be overlapped depending on the respective R and C values, making difficult the separation between bulk and grain boundary contributions. However, plotting the EIS data with different formalisms might allow the separation of the two peaks, if present [35]. An evaluation of the EIS data in figure 15 with other

formalisms did not show the presence of other peaks, confirming the presence of a single RC element for both the samples. The capacitance value measured for the SDC/MgO sample is on the upper range of values typical for doped-ceria grain boundary conductivity [33]. A single semicircle was measured also for the polycrystalline SDC/MgO samples. Therefore, considering the film morphology, in this case the *RC* element was attributed to the grain boundary contribution, due to the fact that the nanometric size of the crystals minimizes bulk conduction contribution [3]. Moreover, the in-plane cell configuration used for EIS measurements should expand grain boundary contribution since the current lines pass across the columnar grain boundaries. Therefore, the samples can present predominant bulk or grain boundary contributions depending on their microstructural features, as expected from SEM observations. The Nyquist plots at low frequencies (f < 1 kHz) for both the samples showed limited polarization and scattering phenomena at the Au electrodes. This fact was probably due to the high temperature used for the measurements and the low impedance values associated with polarization phenomena. Polarization at lower temperatures could not be evaluated because of the high impedance values of the samples at low temperatures reached the instrument resolution limits. Figure**.** 16 shows the Arrhenius plots in the 400 - 775 °C temperature range measured for the post-annealed SDC/MgO (fig.16a) and SDC/STO/MgO (fig. 16b) films in air and in Ar-H_2 mixtures at different pO_2. The total conductivity σ_{tot} was evaluated by the R_i values obtained by the single semicircle registered by the EIS measurements at all the temperatures. Figure 16 a shows the conductivity for SDC/MgO samples

measured in air in two different cooling ramps from 775 to 400 °C (in fig. 16 a, I and II cycle) and at 600 °C at pO_2= 10^{-3} atm and pO_2 =10^{-25} atm (see zoom in the inset).

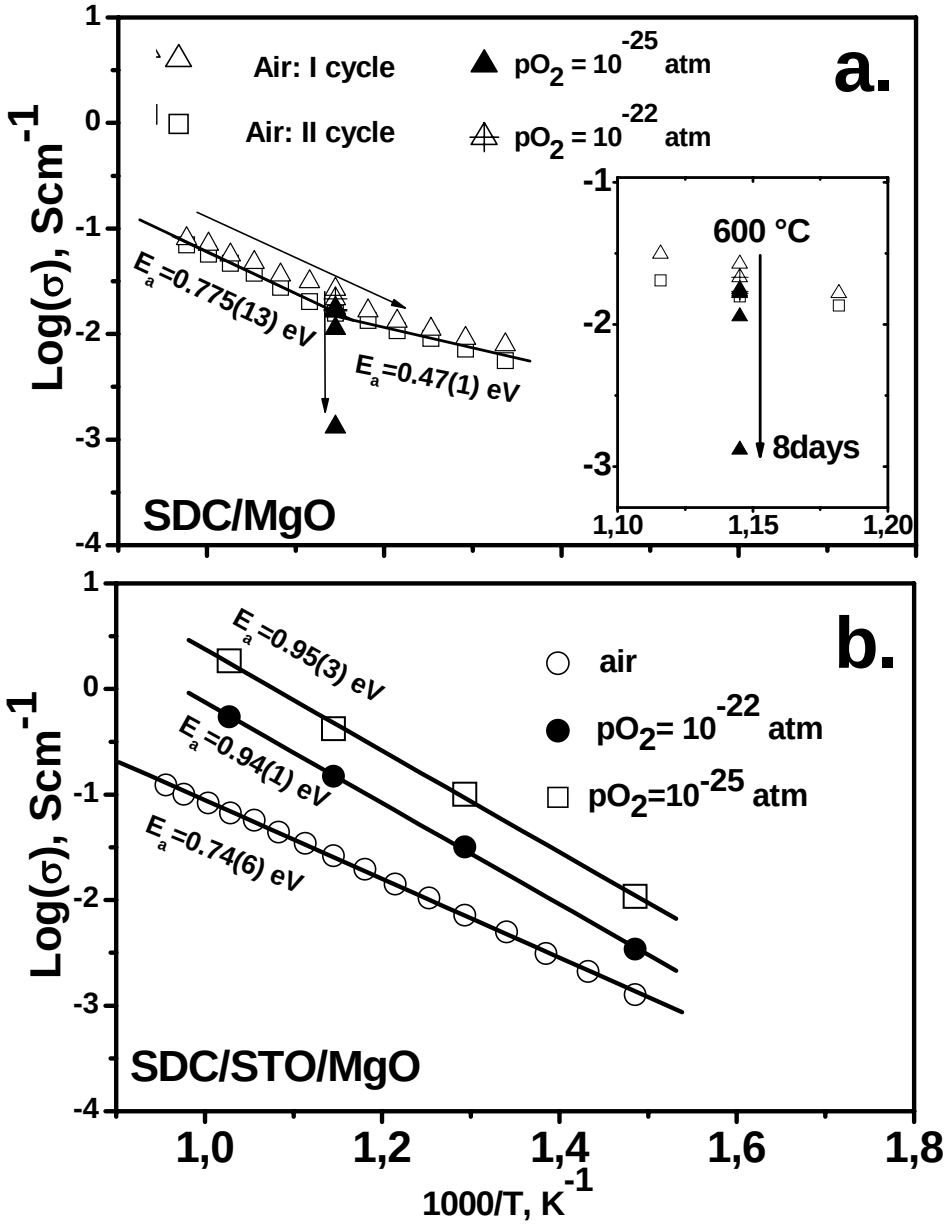

Figure 16. Arrhenius plots in the 400 - 775 °C temperature range measured for the post-annealed SDC/MgO (a) and SDC/STO/MgO (b) films in air and in Ar-H_2 mixtures at different pO_2.

Measurements were collected in about 14 days: each cycle was carried out in 3 days, and the measurements at low oxygen partial pressures required 8 days to reach the balance with the atmospheres. From these data typical activation energy, for temperatures above 600 °C, was calculated to be about 0.775 eV and below 600 °C to be about 0.47 eV. Such values are lower than the values 0.8-0.9 eV usually reported for polycrystalline doped-ceria grown thin films [37]. Particularly, at lower temperatures the Ea resulted close to the activation energy values reported for electron hopping mechanism phenomena for ceria and doped ceria [37]. However, the conductivity data collected revealed the instability of the SDC/MgO sample. Particularly, the conductivity decreased in air of 30-40 % from the I cycle to the II cycle. However, conductivity decreased drastically of around 2 magnitude orders in 8 days, when the sample was exposed to hydrogen atmospheres (inset fig. 18a). Such degradation was irreversible since the conductivity did not return to the values registered when, finally, the sample was re-exposed to air. An explanation to such a conductivity decay was found to be the microstructural instability which led to the cracks and porosity formation observed in the SDC/MgO sample (fig. 13). On the other hand, the SDC/STO/MgO sample was observed to be stable for all the time of measurements and the data were repeatable for all the temperatures and atmospheres. In this case Arrhenius plots could be drawn in air and in low oxygen partial pressure atmospheres. Figure 16b shows that sample conductivity increased with decreasing pO_2. σ_{tot} in air at 700 °C was evaluated to be about 7 10^{-2} S cm^{-1}. Such a value is larger than conductivity value (~2 10^{-2} S cm^{-1} at 700 °C) measured for the dense polycrystalline pellets obtained by a conventional sintering of the SDC powders [11].

Both stability and enhanced conductivity of SDC films onto STO buffer layers was attributed to the low disorder of the epitaxial deposition, resulting in the absence of grain boundaries, which means absence of conduction blocking effects and of high energy unstable regions. The calculated activation energies, E_a, for the SDC/STO/MgO film were found to be 0.74 eV in air, 0.94 eV for $pO_2 = 10^{-22}$ atm, and 0.95 eV for and $pO_2 = 10^{-25}$ atm. This can be explained in terms of different conduction mechanisms in air and at low pO_2. E_a values in air correspond to the typical activation energies reported for ionic conduction in doped-ceria bulk and thin film shapes [14, 18]. The conductivity enhancement at low pO_2 can be attributed to electronic conductivity related to the Ce reduction at low pO_2 [13, 14, 18, 35]. The typical process of ceria reduction may be written as:

$$O_o + 2Ce_{Ce} = \frac{1}{2}O_2(gas) + V_O^{\bullet\bullet} + 2Ce'_{Ce}(2e') \quad (2)$$

where the Kröger-Vink notation has been used, and $[V_O^{\bullet\bullet}]$ represents the oxygen vacancy concentration in doped ceria. The associated equilibrium constant K_r is:

$$K_r = [V^{\bullet\bullet}]n^2 pO^{1/2} \quad (3)$$

where $n = [e']$ represents the electron concentration. In mixed ionic-electronic conductorss, the total electric conductivity, σ_{tot}, is given by two contributions: ionic, σ_{ion}, and electronic, σ_e. The relation between σ_e and oxygen partial pressure pO_2 is described by the Brouwer equilibrium equation:

$$\sigma_e = K_r p(O_2)^{-r} \quad (4)$$

where r is usually 1/4 or 1/6 for doped ceria, depending on the stoichiometry of the electrochemical reduction reaction [12]. On the contrary, σ_{ion} does not depend on

pO_2 because the $V_O^{\bullet\bullet}$ concentration is nearly independent from the cerium valence state [12].

Therefore, to evaluate the Brouwer equilibrium equation and the electronic conductivity of the ceria films, EIS measurements were performed in a wide range of oxygen partial pressures. Figure 17 shows the Brouwer diagram for the SDC/STO/MgO sample obtained from EIS measurements at 400 °C, 500 °C, 600 °C, and 700 °C. σ_{tot} was constant in a pO_2 range whose width depended on the temperature.

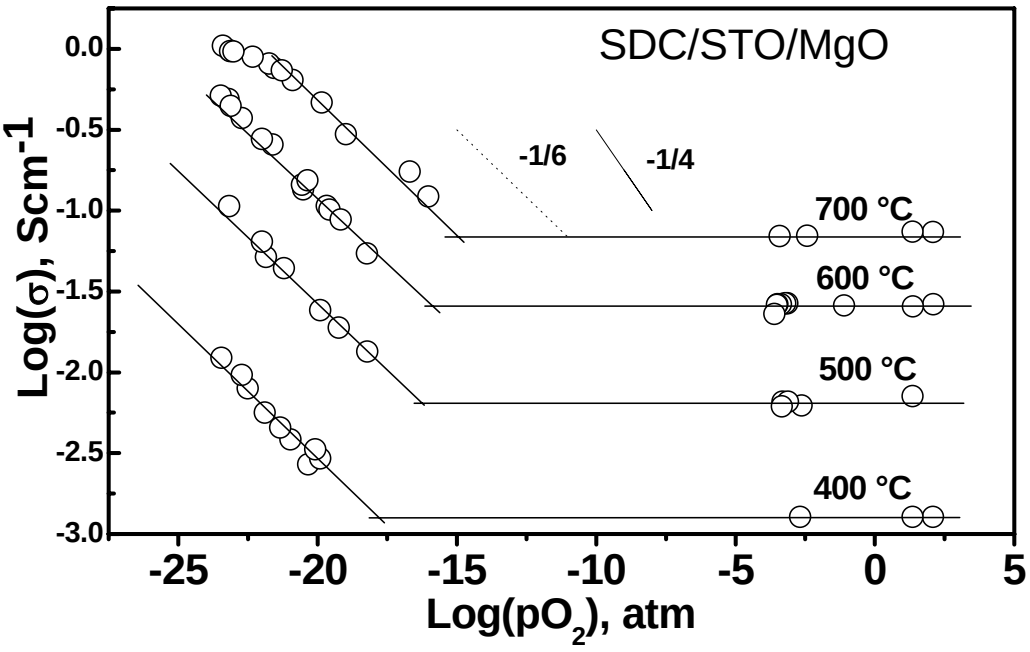

Figure 17. Total electrical conductivity as a function of oxygen partial pressure for the SDC/STO/MgO sample at 400, 500, 600, and 700 °C, obtained from EIS measurements.

In particular, figure 17 shows that at 400°C a plateau (horizontal lines in fig. 17) was observed in the 10^{-17} atm -1 atm pO_2 range. At higher temperatures, the plateau lower

limit was restricted at pO_2 values of about 10^{-16}-10^{-15} atm. Ionic conductivity was dominant in the plateau regions [12]. At all temperatures, conductivity increased for $pO_2 < 10^{-17}$ atm with decreasing pO_2 with a linear trend. In these cases, the σ_e component was predominant and changed according to the Brouwer equilibrium equation (eq. 4). In particular, the sample exhibited a linear trend with a calculated slope of -1/6, independent from the temperature. In polycrystalline bulk ceria, the -1/6 slope value is usually expected for pure ceria or low doped-ceria where $[V_O^{\bullet\bullet}]$ depends on the cerium valence state [12]. Conversely, a -1/4 slope is reported for highly doped ceria where $[V_O^{\bullet\bullet}]$ depends on the dopant concentration only, and it can be regarded as independent from the cerium oxidation state [12, 35, 36]. For polycrystalline doped ceria thin films, different slope values (-1/25, -1/6, -1/4) have been reported, depending on the film microstructure and thickness [18, 37, 38]. One possible explanation of the -1/6 slope value observed in the present work is the presence of the STO layer and SDC/STO interface where the oxygen vacancy concentration depends on the lattice defects formed at the interface and not on the dopant concentration [39]. However the -1/6 slope can be due to the electrical contribution of the STO buffer layer at lower oxygen partial pressure. Electrical properties of STO buffered SDC heterostructure demonstrated structural stability on MgO and measurements led in reducing-oxidizing condition for several weeks exhibited good reproducibility.

3.6 Conclusions

SDC thin films were grown by PLD on (001) single crystal MgO substrates. SDC single crystal thin film can be grown on insulating MgO substrate by using thin STO buffer layer. Onto STO buffer layer, SDC fluorite film grows with a reduced lattice mismatch respect to SDC deposited directly on the MgO substrate. Because of the reduced lattice misfit between the materials, SDC single-crystal structure exhibited high stability in both oxidizing and reducing atmospheres. Conversely SDC on MgO is instable in hydrogen atmosphere where microstructural transformation lead to crack, porosity and delamination. The STO buffer layer gives the possibility to evaluate the SDC single-crystal film electrical properties without introducing contribution from conducting substrates. The single-crystal thin film shows conductivity about 0.07 S cm^{-1} at 700 °C and predominant ionic conductivity for pO_2 higher than 10^{-17} atm. Dominant electronic conductivity is observed at pO_2 below 10^{-17} atm where conduction mechanism activation energy is 0.95 eV and a typical $\log(\sigma)$-pO_2 slope of -1/6. This peculiar SDC/STO electrical behavior could be attributed to the presence of the SDC-STO interface which introduces additional contribution especially at low pO_2 where electronic conduction component in SDC is dominant.

References

[1] U.P. Muecke, D. Beckel, A. Bernard, A. Bieberle-Hütter, S. Graf, A. Infortuna, P. Müller, J.L.M. Rupp, J. Schneider, L.J. Gauckler, *Adv. Funct. Mater.* **2008**, *18,* 3158.

[2] A. Bieberle-Hütter, J.L. Hertz, H.L. Tuller, *Acta Mater*. **2008**, *56*, 177.

[3] J. Fleig, H.L. Tuller, J. Maier, *Solid State Ionics* **2004**, *174*, 261.

[4] J. H. Joo, G.M. Choi, *J. Eur Ceram Soc*. **2007**, *27*, 4273.

[5] J.L. Hertz, H.L. Tuller, *J. Electroceram*. **2004**, *13*, 663.

[6] N. Ito, M. Iijima, K. Kimura, S. Iguchi, *J. Power Sources* **2005**, *152*, 200.

[7] S. J. Litzelman, J. L. Hertz, W. Jung, H. L. Tuller, *Fuel Cells* **2008**, *5*, 294.

[8] A. Bieberle-Hütter, D. Beckel, A. Infortuna, U.P. Muecke, J.L.M. Rupp, L.J. Gauckler, S. Rey-Mermet, P. Muralt, N.R. Bieri, N. Hotz, M.J. Stutz, D. Poulikakos, P. Heeb, P. Müller, A. Bernard, R. Gmür, T. Hocker, *J. Power Sources* **2008**, *177*, 123.

[9] B.C.H. Steele, *Solid State Ionics* **2000**, *129*, 95.

[10] D.J.L. Brett, A. Atkinson, N.P. Brandon, S.J. Skinner, *Chem. Soc. Rev.* **2008,** *37*, 1568.

[11] V. Esposito, E. Traversa, *J. Am. Ceram. Soc*. **2008**, *91*, 1037.

[12] M. Mogensen, N.M. Sammes, G.A. Tompsett, *Solid State Ionics* **2000**, *129*, 63.

[13] L. Chen, C. L. Chen, X. Chen, W. Donner, S. W. Liu, Y. Lin, D. X. Huang, A. J. Jacobson, *Appl. Phys. Lett*. **2003**, *83*, 4737.

[14] L. Chen, C.L. Chen, D.X. Huang, Y. Lin, X. Chen, A.J. Jacobson, *Solid State Ionics* **2004**, *175*, 103.

[15] G. Chiodelli, L. Malavasi, V. Massarotti, P. Mustarelli, E. Quartarone, *Solid State Ionics* **2005**, *176*, 1505.

[16] D.X. Huang, C. L. Chen, A. J. Jacobson, *J. Appl. Phys*. **2005**, *97*, 043506-1.

[17] C. Brahim, A. Ringuedé, E. Gourba, M. Cassir, A. Billard, P. Briois, *J. Power Sources* **2006**, *156*, 45.

[18] A. Karthikeyan, M. Tsuchiya, C.L. Chang, S. Ramanathan, *Appl. Phys. Lett*. **2007**, *90*, 263108.

[19] A. Infortuna, A. S. Harvey, L.J. Gauckler, *Adv. Funct. Mater.* **2008**, *18,* 127.

[20] A. Tebano, G. Balestrino, N.G. Boggio, C. Aruta, B. Davidson, P.G. Medaglia, *Eur. Phys. J. B* **2006**, *51,* 111.

[21] T.D. McColm, J.T.S. Irvine, *Ionics*, **2001**, *7*, 116.

[22] M. Ahrens, R. Merkle, B. Rahmati, J. Maier, *Phys.*, *B* **2007**, *393*, 239.

[23] E. Ruiz-Trejo, J.D. Sirman, Yu. M. Baikov, J.A. Kilner, *Solid State Ionics* **1998**, *113-115*, 565.

[24] X. Castel, M. G. Viry, A. Perrin, J. Lesueur, F. Lalu, *J. Cryst. Growth* **1998**, *187*, 211.

[25] A.R. Meier, F. Niu, B.W. Wessels, *J. Cryst. Growth* **2006**, *294*, 401.

[26] V. Boffa, T. Petrisor, L. Ciontea, U. Gambardella, S. Barbanera, *Physica C* **1996**, *260*, 111.

[27] R.W.G. Wyckoff, *Z. Kristallogr.*, **1925**, *62*, 529.

[28] G. Brauer, H. Gradinger, *Allgem. Chem*. **1954**, *276*, 209.

[29] J. Hutton, R. J. Nelmes, *J. Phys. C*, **1981**, *14*, 1713.

[30] N. Sata, K. Eberman, K. Eberl, J. Maier, *Nature* **2000**, *408*, 946.

[31] G. Hsieh, S.J. Ford, T.O. Mason, L.R. Pederson, *Solid State Ionics* **1996**, *91*, 191.

[32] J.R. Macdonald, *Impedance Spectroscopy—Emphasizing Solid Material and Systems*, Wiley Interscience, New York, N.J. **1987** Ch.2.

[33] J.T.S. Irvine, D. C. Sinclair, A. R. West, *Adv. Mater*. **1990**, *2*, 132.

[34] D. C. Sinclair, A. R. West, *J. Appl. Phys*. **1989**, *66*, 3850.

[35] J.L.M. Rupp, A. Infortuna, L. J. Gauckler, *Acta Mater*. **2006**, *54*, 1721.

[36] W. Lai and S. M. Haile, *J. Am. Ceram. Soc*. **2005**, *88*, 2979.

[37] T. Suzuki, I. Kosacki, H.U. Anderson, *Solid State Ionics* **2002**, *151*, 111.

[38] J.H. Joo, G.M. Choi, *Solid State Ionics*, **2007**, *27*, 4273.

[39] J. Garcia-Barriocanal, A. Rivera-Calzada, M. Varela, Z. Sefrioui, E. Iborra, C. Leon, S.J. Pennycook, J. Santamaria, *Science*, **2008**, *321*, 676.

Chapter 4

Structural and electrochemical characterization of [SDC/YSZ] heterostructures

4.1 Introduction

High quality YSZ/SDC superlattices having different modulation length Λ have been grown by pulsed laser deposition onto $SrTiO_3$ buffered (001) MgO substrates. The presence of the $SrTiO_3$ buffer layer, with thickness only 10 nm, improved the lattice match between substrate and YSZ/SDC superlattice without giving a relevant contribution to overall conductivity. Individual layers became heavily strained when Λ was reduced below 28 nm. A sizeable contribution to ionic conductivity from interfaces was measured. The interface contribution was larger in superlattices consisting of thinner individual layers. Such an effect was ascribed to the large in plane tensile epitaxial strain. Different $(YSZ/SDC)_N$/STO/MgO heterostructures, with N number of YSZ/SDC bilayers, were grown by a pulsed laser deposition

(PLD) equipment with a multitarget system allowing for sequential growth of the constituent layers without exposure to the atmosphere. The thickness of the STO buffer layer is only 10 nm and, therefore, it is not expected to give a sizeable contribution to the overall conductivity of the heterostructures. The superlattice modulation length Λ (thickness of an individual YSZ/SDC bilayer) was tuned varying the number of laser shots on the targets. The SDC target was prepared using $(CeO_2)_{0.8}(Sm_2O_3)_{0.2}$ powders synthesized in our laboratory using a direct coprecipitation method. The YSZ target was prepared using (ZrO_2):8 mol % Y_2O_3 commercial powder. Cylindrical pellets were fabricated by uniaxially cold-pressing the powder at 140 MPa and sintering it at 1450°C for 10 h. Sample crystallographic properties were characterized by x-ray diffraction (XRD) using a Bragg-Brentano diffractometer with Cu Kα radiation. θ-2θ scans around the (002) symmetric reflection and reciprocal space mapping around the (113) asymmetric reflection were performed on the $(YSZ/SDC)_N$/STO/MgO heterostructures. Electrochemical Impedance Spectroscopy (EIS) characterization was carried out in a two-electrode configuration geometry using silver paste electrodes painted onto the film surface. EIS measurements were performed in the 500–800°C temperature range and 0.01 Hz–10 MHz frequency range, with a 50mV alternate signal. Electrical conductivity measurements were carried out at an oxygen partial pressure pO_2 in the range between 10^{-25}-1 atm.

4.2 Heterostructures and superlattices

Recent developments in the field of thin films growth technologies have allowed a control at an atomic level of deposited layers thus opening new perspectives in the

field of engineering of multilayers and heterostructures based on complex oxides [1]. In particular, it is expected that oxide heterostructures, having almost ideal interfaces, may lead to interesting artificial materials with novel properties. Artificial thin-film oxide structures make the already complex individual bulk properties even more interesting through their interaction at the interface. Following such an approach a number of heterostructures showing extraordinary properties, which do not belong to the individual layers, have been tailored. These range from superconductivity at the interface between non superconducting layers to high mobility 2D conductivity at the interface between insulating oxides [2,3]. The number of possible combinations of these oxides is enormous, and the potential for novel behaviour having practical applications represents a strong motivation for this research. The same approach can be applied to heterostructures based on oxide ion conductors provided that the issues concerning structural match at the interface are solved. The interest in oxide ionic conductors based heterostructures is driven by the space-charge-zone effects at the interface, which can increase locally the charge carrier concentration, and on interface mobility effects, the latter effect being of particular relevance in the case of materials with high defects density and relatively low mobility. The potential impact of oxide ionic conductors superlattices has been shown in ref.[4]. In this case superlattices based on CaF_2 and BaF_2 layers, grown by Molecular Beam Epitaxy, exhibited an ionic conductivity increasing with the number of interfaces. For thinner individual layers the increase of conductivity of the superlattices relative to the pure BaF_2 films was about two orders of magnitude over the whole measured temperature range. These results were found in excellent agreement with a model based on a redistribution of fluoride atoms at the interface.

More recently the same approach was applied to the investigation of superlattices made of $SrTiO_3$ (STO) and (ZrO_2):8 mol % Y_2O_3 (YSZ). In this case a colossal enhancement of the ionic conductivity of several orders of magnitude relative to the pure YSZ compound was found even at room temperature [5]. However, this finding was successively criticized on the basis of the ionic conductivity from the much thicker STO substrate hindering the superlattice contribution [6]. In this chapter I consider a superlattice system based on samarium doper ceria (SDC) and yttria stabilized zirconia (YSZ). These systems are highly defective so that eventual interface effects should be related to mobility enhancement phenomena rather than to space-charge-region effects [7]. Samarium doped ceria (SDC) shows larger ionic conductivity than yttria-stabilized zirconia (YSZ), the conventional SOFC electrolyte material, and is thus intensively studied to reduce the SOFC operating temperature in the 600-800 °C range [8-10]. Doped ceria films having fluorite structure can be deposited, starting from a polycrystalline target, on several non-fluorite substrates maintaining the correct stoichiometry [11]. In particular, doped ceria has been shown to grow on (001) MgO substrates as well as on (001) $LaAlO_3$ (LAO), (110) $NdGaO_3$ (NGO), and (001) STO perovskite substrates [12,13]. Perovskite-type substrates provide the proper lattice match for ceria, inducing the growth of epitaxial monocrystalline films with a low degree of structural disorder [13]. Namely, STO, LAO and NGO have a cubic (pseudocubic for NGO) structure with lattice parameter values a=3.905 Å (STO), 3.86 Å (NGO) and 3.79 Å (LAO). On the other hand the lattice parameter of highly doped SDC (20% molar samarium oxide) is a=5.44 Å. This circumstance does not allow a good “square on square” epitaxial relationship between (001) oriented perovskite substrates and SDC films. On the other hand, the

interplanar distance along the in-plane [110] direction for STO results to be $d_{(110)}$=5.52 Å which gives a good match with the SDC cubic parameter (*Δa/a=1,5%* for STO and even better for NGO and LAO). As a consequence the epitaxial growth may occur with a relative rotation of 45° of the cubic axis: the [110] film direction lies along the [100] substrate direction. This circumstance was experimentally verified in ref. [14]. Heteroepitaxial growth of YSZ on STO/SDC structures may be more difficult because of the smaller value of its lattice parameter (a= 5.14 Å). Unfortunately, perovskite substrates are unsuited because of their electrochemical properties: namely they show electronic, ionic, or mixed ionic-electronic conduction at temperatures above 300 °C, which might affect the proper evaluation of the electrical measurements performed on films [12]. On the other hand MgO, another standard substrate material, shows a remarkably low electrical conductivity at high temperatures but does not provide a good lattice match with YSZ and SDC: namely the cubic lattice parameter of MgO (*a=4,21 Å*) results in a large structural mismatch with both YSZ and SDC. As a consequence, ionic oxide conductor films on MgO show a higher degree of structural disorder, which can result in ionic conduction blocking effects and to contaminant segregation phenomena [15,16]. In the past YSZ/SDC superlattices have been grown on Al_2O_3 substrates [17]. Al_2O_3 is an excellent substrate from the viewpoint of electrochemical properties but shows a poor structural compatibility with YSZ and SDC. Films grown on such substrates showed the presence of spurious phases and high interface roughness which, very likely, are at the origin of the decrease of the ionic oxygen conductivity when the individual layer thickness decreases below 15 nm [17]. A solution to the problem of epitaxial growth of SDC films having high crystallographic quality onto substrates

that do not contribute to the ionic conductivity was showed in ref. [14]. The proposed approach foresees the use of a thin (few nm thick) STO buffer layer to adapt the SDC crystallographic structure with the MgO structure. STO buffer layers were successfully used in the past to adapt the lattice parameter of (001) MgO substrates to high Tc superconducting cuprates [18]. When used in connection with SDC, STO buffered MgO substrates resulted in thin films having excellent structural and transport properties. In this chapter I extend the same approach to the growth of SDC/YSZ superlattices. Preliminary results on SDC/YSZ superlattices onto perovskite substrates are reported in ref. [19]. However, in this case, electrochemical properties were hindered by the overwhelming contribution from the substrates.

4.3 XRD characterization

Fig.1 shows the XRD θ-2θ patterns of different $(YSZ/SDC)_N$/STO/MgO heterostructures having roughly the same overall thickness but N ranging from 1 to 20. A sketch of the heterostructure is shown at the top of figure 1.

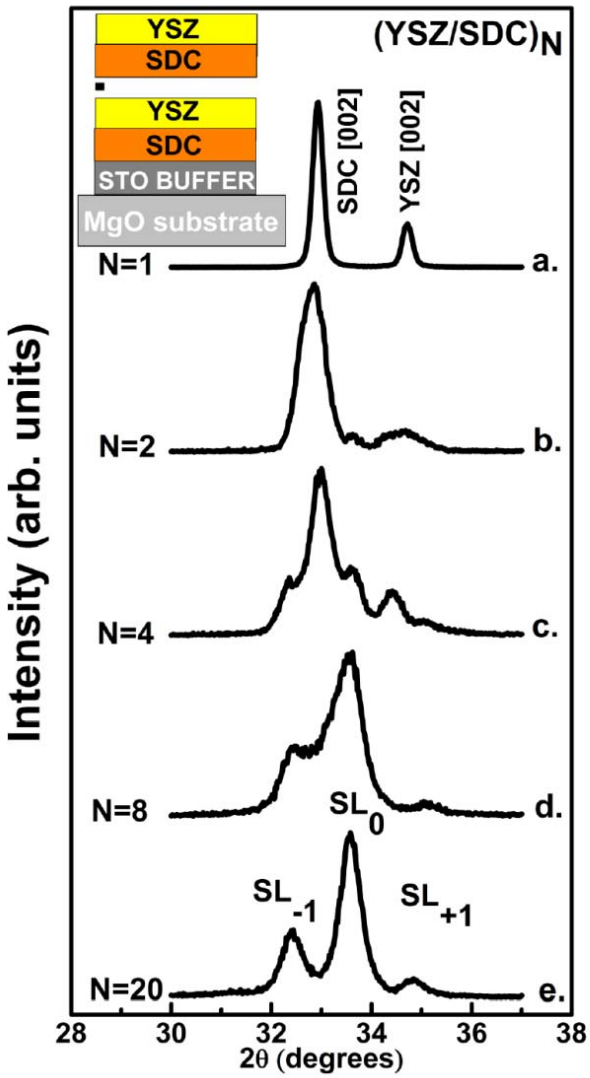

Figure 1. XRD θ-2θ patterns of several $(YSZ/SDC)_N$/STO/MgO heterostructures with approximately the same overall thickness but N ranging from 1 to 20 (fig.a. to fig.e.). A sketch of the heterostructure is shown at the top.

For N=1 (Fig.1 a.) two separate diffraction peaks, corresponding to the (002) reflections of SDC and YSZ, respectively, are visible. When the number of bilayers N is increased (Fig.1 b. to d.), interference effects between the SDC and YSZ blocks start to show up. Finally, for N=20 (Fig.1 e.), the typical features of a superlattice pattern can be recognized: an average structure peak SL_0 together with the two first

order satellite peaks SL_{-1} and SL_{+1}. The appearance of sharp satellite peaks indicates high quality interfaces between the two constituent oxides.

The angular position of the satellite peaks allows calculating the thickness of the individual bilayer according to the formula

$$\Lambda = \frac{\lambda_{Cu}}{\sin\theta_{+1} - \sin\theta_{-1}} \quad (1)$$

where λ_{cu} is the Cu Kα wavelength and $\theta_{+1}$and θ_{-1} are the positions of the SL_{+1} and SL_{-1} peaks in the θ-2θ scan. For N=20, Λ resulted to be 7.7 nm and the total film thickness 154 nm. Fig.2 illustrates the epitaxial relationships among the different constituent blocks of our heterostructures as deduced by XRD asymmetric reflections [14].

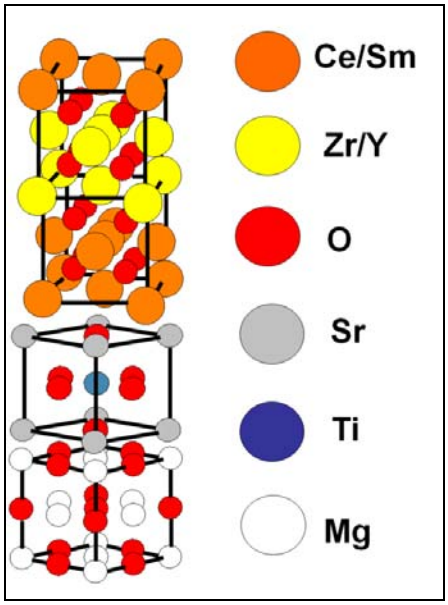

Figure 2. Epitaxial relationship among the different constituent blocks of the $(YSZ/SDC)_N$/STO/MgO heterostructure.

In the drawing the SDC and YSZ blocks are supposed to be strained adopting the same in plane lattice parameters. In practice, depending on the individual layer thickness, blocks can relax so that lattice parameters approach their bulk values.

4.4 Electrochemical Impedance characterization of $(YSZ/SDC)_N$ superlattices

Figure 3 shows typical Nyquist plots of imaginary part (–Im(Z)) versus real part (Real(Z)) of the complex impedance for the sample $[YSZ/SDC]_{N=20}$ having the modulation length of Λ=7.7 nm at several temperatures (from 700°C to 800°C) measured in air.

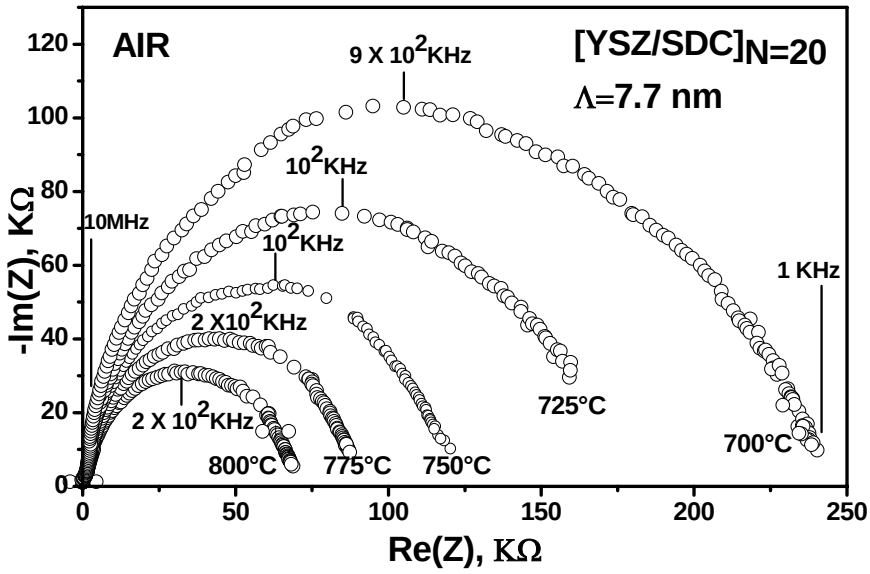

Figure 3. Nyquist plots of the sample $[YSZ/SDC]_{N=20}$ with modulation length Λ=7.7 nm measured in air at several temperatures.

The Nyquist plots (fig.3) exhibited a single semicircle for several temperatures due to a resistive (R) and a capacitive (C) element in parallel. Fig.4 a. shows the Arrhenius plot, in the 400-800°C temperature range, of the electrical conductivity measured in air for SDC/YSZ superlattices having the same overall thickness of 154 nm but N=3, N=8 and N=20, respectively. Figure 4b. shows the Arrhenius plot for a set of superlattices having the same number of interfaces but Λ=7.7 nm, 15 nm, 28 nm, respectively.

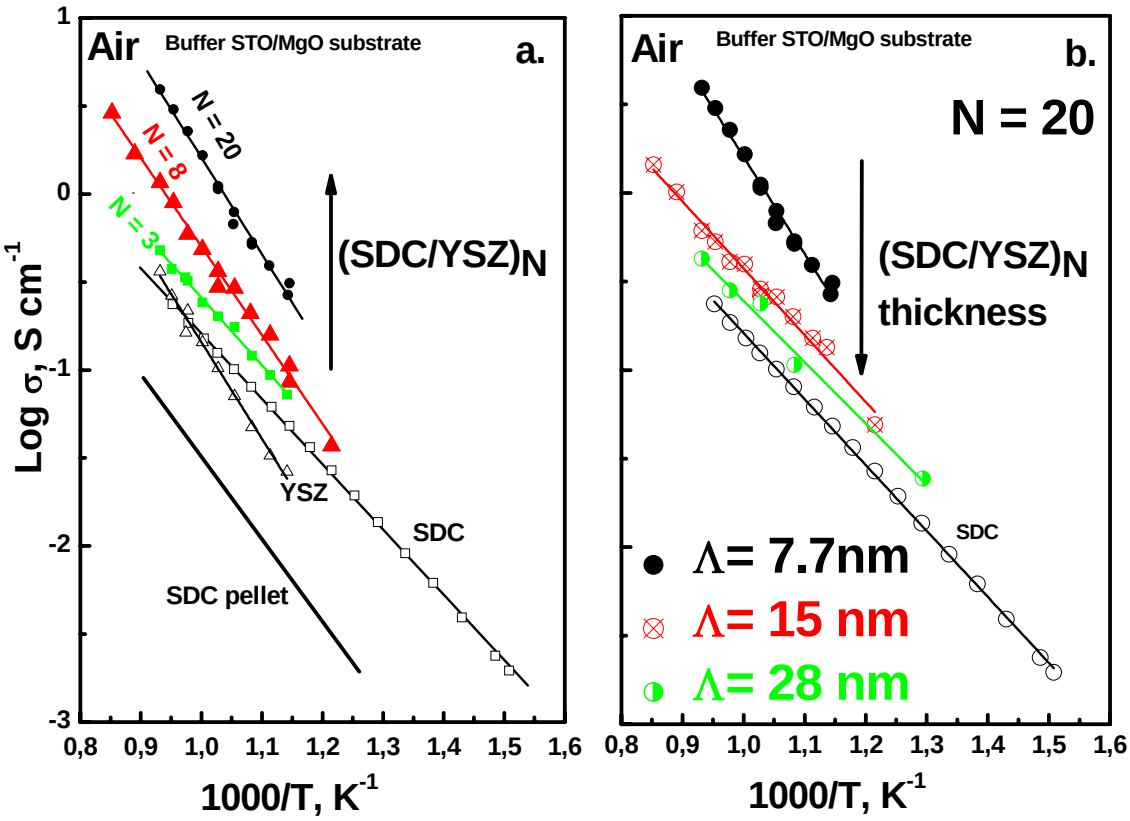

Figure 4. Arrhenius plots, in the 400-800°C temperature range, of the electrical conductivity in air for several $(YSZ/SDC)_N$/STO/MgO superlattices: (a.) SDC/YSZ superlattices having the same overall thickness of 154 nm but N=3 (green full squares), N=8 (red full triangles) and N=20 (black full circles), respectively, the conductivity of thin films SDC/STO/MgO (black empty squares), YSZ/STO/MgO (empty triangles) and SDC pellet (filled line). (b.) conductivity of superlattices having the same number of interfaces (N=20) but Λ=7.7 nm (black filled circles), 15 nm (red crossed circles), 28 nm (half filled circles), respectively, the conductivity of thin films SDC/STO/MgO (black empty circles).

Conductivity of pure SDC and YSZ thin films deposited onto STO buffered MgO, together with the conductivity of a SDC pellet, are reported for comparison. In particular SDC/YSZ films with N=20, showed an increase of conductivity of about one order of magnitude at 700°C relative to SDC and YSZ thin films conductivity, and about two orders of magnitude relative to SDC polycrystalline pellets [10]. The increase of conductivity in monocrystalline high quality SDC films has been reported in ref [14]. The dependence of conductivity on N for films having the same overall

thickness (Fig.4 a.) clearly demonstrates a sizeable interface contribution to conductivity. Fig. 4 b. shows that the interface contribution becomes much more relevant when the individual layer thickness is decreased. Moreover, the activation energy for the multilayered films increased from 0.76 (3) eV to 1.09 (3) eV decreasing the bilayer thickness Λ. Fig. 5 shows the dependence of conductivity on Λ at several temperatures.

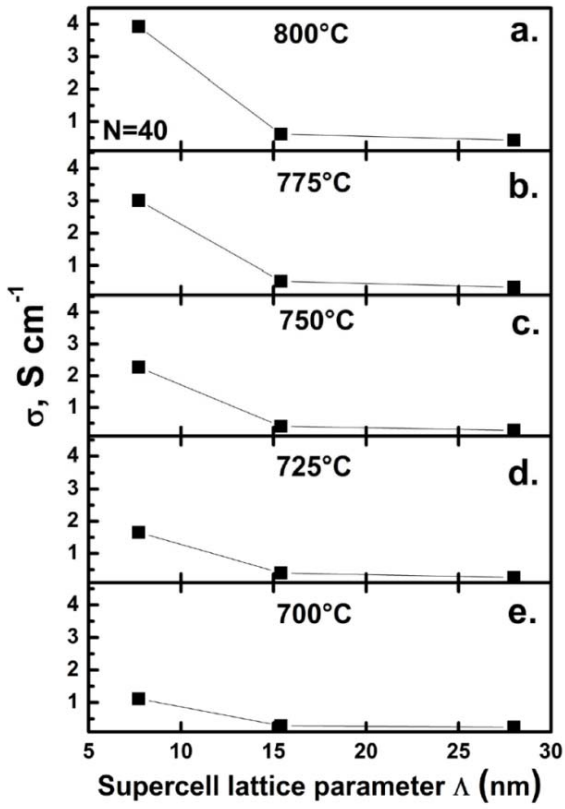

Figure 5. Dependence of conductivity on Λ at several temperatures.

A sizeable increase of conductivity can be noticed when decreasing Λ. This effect is similar to that observed by other researchers in very thin layers of ionic conductors [4,17]. However, in Ref. [4, 17] a reversed effect, namely a decrease of ionic conductivity, was observed when Λ decreased below a critical value of either 16 nm in [4] or 30 nm in [17]. Possibly, the decrease of ionic conductivity in very thin

layers was ascribed to the high interface roughness which could disrupt ionic conductivity on a macroscopic length. In our case the increase of ionic conductivity with the reduction of Λ is observed all the way down to the smallest value of Λ = 7,7 nm. In order to separate the ionic and electronic contributions, EIS measurements were carried out in the oxygen partial pressure (pO_2) range between 10^{-25} atm and 1 atm (Brouwer diagrams) and in the temperature range from 600°C to 800°C. Fig.6a shows the Brouwer diagrams for samples consisting of three and 20 bilayers. The Brouwer diagram of a thick YSZ film deposited onto a STO buffered MgO is also shown for comparison. The conductivity at 800°C of superlattices having N=3 and 20 remained constant in the pO_2 range between 1 atm and 10^{-15} atm, thus showing that, in this pO_2 range, conductivity is dominated by the ionic contribution [20]. For $pO_2<10^{-15}$ atm, conductivity increased with decreasing pO_2: in this region the electronic conductivity σ_e predominates changing according to the Brouwer equilibrium conditions [20-22]. On the other hand, for a pure YSZ film, a wider plateau extending from 1 atm to 10^{-20} atm was observed at 800°C. Fig.6b shows the Brouwer diagrams for a superlattice with N=20 taken at 600°C, 700°C and 800°C.

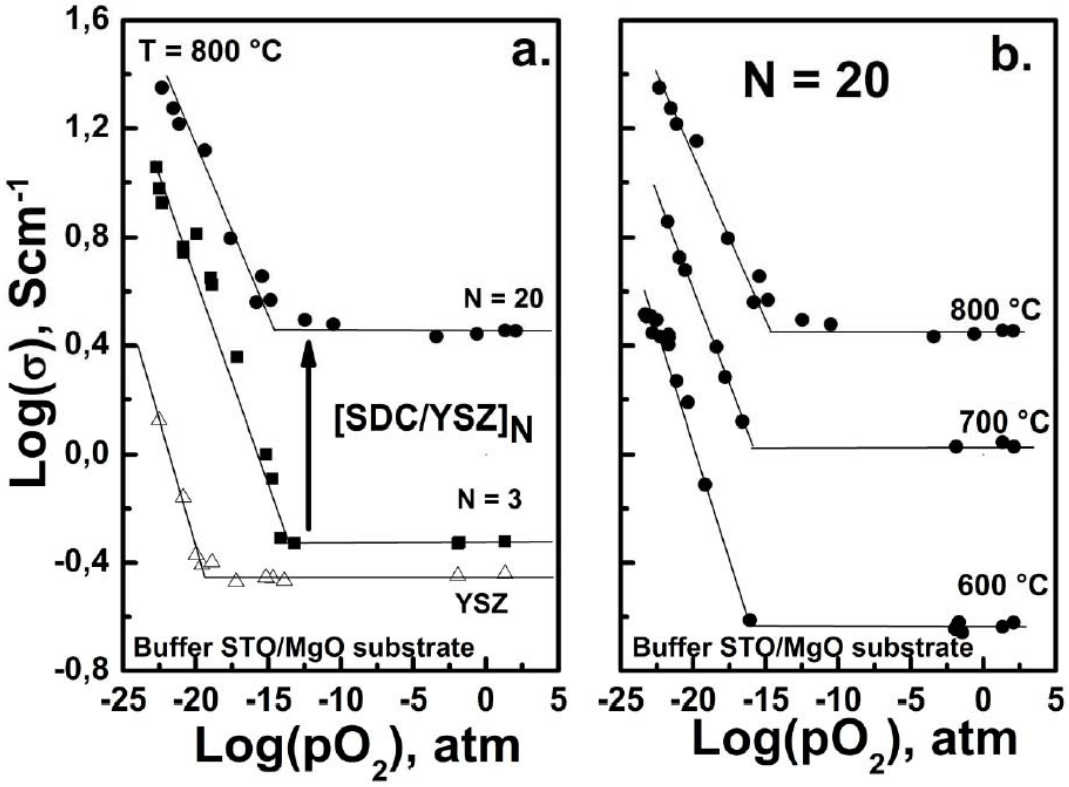

Figure 6. Brouwer diagrams for samples having N=3 and N=20 (a). YSZ/STO/MgO is also shown for comparison. Brouwer diagrams for a superlattice with N=20 taken at 600°C, 700°C and 800°C (b).

In these diagrams the plateau extends in the same pO_2 range, namely from 1 atm to 10^{-15} atm, regardless of temperature. For $pO_2<10^{-15}$ atm the conductivity increased with the same slope for all temperatures. These results are in agreement with the Brouwer diagram of a pure SDC film showing that the electronic contribution is a "bulk" SDC effect and not an interface effect [14]. Moreover, the Brouwer diagrams show that the contribution from the STO buffer layer does not affect the electrical measurements [23].

4.5 X-Ray reciprocal space mapping of $(YSZ/SDC)_N$ heterostructures

Fig.6 shows the reciprocal space maps around the (113) asymmetric reflection for superlattices with N=1 and Λ= 54.4 nm (fig. 7a.), N=20 and Λ= 28 nm (Fig. 7b.) and N=20 and Λ= 7.7 nm (fig. 7c.). The red vertical lines are guides for the eye. Reciprocal space maps allow calculating in-plane *a* and out-of-plane *c* lattice parameters according to the relations $d_{110} = \frac{a}{\sqrt{2}} = \frac{2\pi}{q_x^*}$, $d_{003} = \frac{c}{3} = \frac{2\pi}{q_z^*}$, where $q^*_{x,z}$ refer to the in-plane (*x*) and out-of-plane (*z*) components of the diffracted wavevector. Fig. 7a. (N=1) shows only two peaks which can be attributed to SDC and YSZ, respectively. Lattice parameters were calculated to be about *c*=*a*=5.44 Å for SDC and *c*=*a*=5.14 Å for YSZ. These values are in good agreement with those reported in literature for bulk SDC and YSZ [10, 14, 24]. It can be observed that for the N=1, Λ= 54.4 nm sample the epitaxial strain is fully relaxed: namely each of the two constituent layers results to have its own in-plane bulk lattice parameter without any influence from the under laying buffered substrate. Similarly, two separate peaks (Fig. 7b.) for SDC and YSZ were visible in the reciprocal lattice map of the superlattice with N=20 and Λ= 28 nm. However, in this case, the in-plane peak position of YSZ is shifted toward the SDC position. This indicates that when the thickness is reduced the SDC layer remains fully relaxed while the YSZ is partially strained with an in plane lattice parameter approaching SDC in-plane value. Namely, in this case, the YSZ lattice parameters were calculated to be *c*= 5.14 Å, *a*=5.21 Å, respectively, while the SDC lattice parameters remain essentially unvaried. Fig. 6c.,

referring to the superlattice with the smallest Λ value, shows the presence of a single broad peak whose position coincides roughly with the position of bulk SDC.

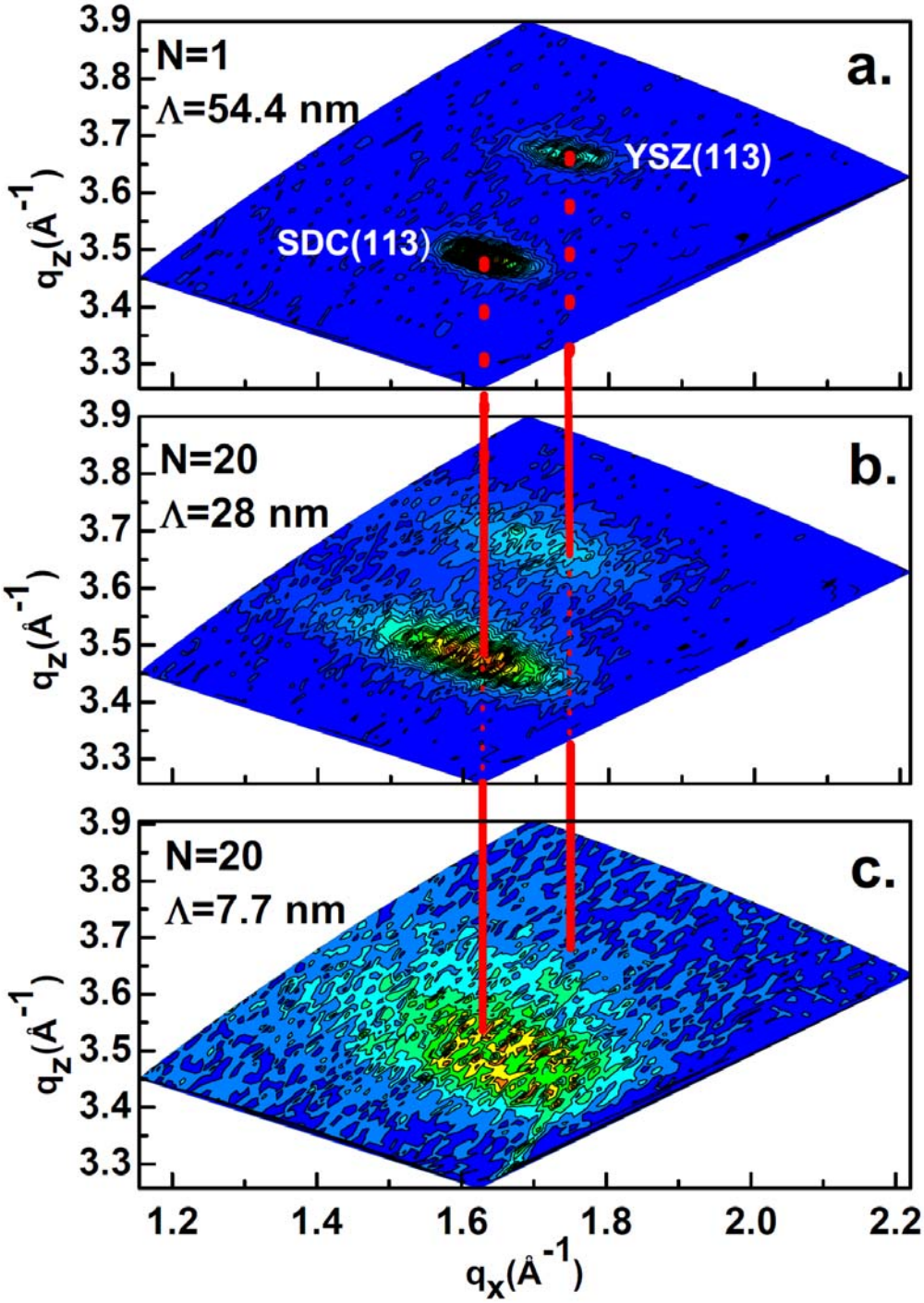

Figure 6. Reciprocal space maps around the (113) asymmetric reflection for superlattices with N=1 and Λ= 54.4 nm (a.), N=20 and Λ= 28 nm (b.) and N=20 and Λ= 7.7 nm (c.). The red vertical lines are guides for the eye.

This result indicates that, when the layer thickness is reduced below a certain value, the YSZ layer tries to adapt its in-plane lattice parameter to the in-plane lattice parameter of SDC thus becoming strongly strained. Assuming, for sake of simplicity, that YSZ is fully strained and SDC fully relaxed, this corresponds to a huge in plane distortion of the YSZ block ($\frac{\Delta a}{a} \cong 6\%$), higher than that usually found for other heteroepitaxial oxide structures.

4.6 Conclusions

Measurements reported in this paper show that a sizeable increase of conductivity occurs at the interface between YSZ and SDC which has not an electronic origin as demonstrated by measurements at reduced pO_2. On the other hand, due to the high defectivity of SDC and YSZ compounds, the effect can be hardly ascribed to interface space-charge-regions. In agreement with previous reports [4,7], we attribute the conductivity enhancement to tensile strain effects. Tensile strain effects have been predicted to give rise to a moderate enhancement of ionic conductivity [7]. XRD measurements demonstrate that, in our superlattices, the YSZ block is heavily strained. Noticeably, ionic conductivity enhancement effects persist down to the thinnest value of Λ= 7.7 nm, namely much smaller than that previously reported in literature. We ascribe this effect to the improved crystallographic quality of interfaces in our $(YSZ/SDC)_N$/STO/MgO heterostructures preventing disruption of electric transport as a consequence of interface roughness.

References

[1] E. Dagotto, *Science* **2007**,*318*, 1076.

[2] N. Reyren S. Thiel, A. D. Caviglia, L. Fitting Kourkoutis, G. Hammerl, C. Richter, C. W. Schneider, T. Kopp, A.-S. Rüetschi, D. Jaccard, M. Gabay, D. A. Muller, J.-M. Triscone, J. Mannhart , *Science* **2007**, *317*, 1196.

[3] A. Ohtomo, H. Y. Hwang, *Nature* **2004**, *427*, 423.

[4] N. Sata, K. Eberl, K. Eberman, J. Majer, *Nature* **2000**, *408*, 946.

[5] J. Garcia-Barriocana, A. Rivera-Calzada, M. Varela, Z. Sefrioui, E. Iborra, C. Leon, S. J. Pennycook, J. Santamaria, *Science* **2008**, *321*,676.

[6] X. Guo *Science* **2008**, *324*, 465a.

[7] X. Guo, J. Maier, *Adv. Mater* **2009**, *21*, 2619.

[8] B. C. H. Steele, *Solid State Ionics* **2000**, *129*, 95.

[9] D. J. L. Brett, A. Atkinson, N. P. Brandon, S. J. Skinner, *Chem. Soc. Rev*. **2008**, *37*, 1568.

[10] V. Esposito, E. Traversa, *J. Am. Ceram. Soc.* **2008**, *91*, 1037.

[11] A. Infortuna, A. S. Harvey, L.J. Gauckler, *Adv. Funct. Mater.* **2008**, *18,* 127.

[12] L. Chen, C. L. Chen, D. X. Huang, Y. Lin, X. Chen, A. J. Jacobson, *Solid State Ionics* **2004**, *175*, 103.

[13] D. X. Huang, C. L. Chen, A. J. Jacobson, *J. Appl. Phys*. **2005**, *97*, 043506-1.

[14] S. Sanna, V. Esposito, D. Pergolesi, A. Orsini, A. Tebano, S. Licoccia, G. Balestrino, E. Traversa, *Adv. Funct. Mater* **2009**, *19*,1713.

[15] L. Chen, C. L. Chen, X. Chen, W. Donner, S.W. Liu, Y. Lin, D. X. Huang, A. J. Jacobson, *Appl. Phys. Lett*. **2003**, *83*, 4737.

[16] E. Ruiz-Trejo, J. D. Sirman, Y. M. Baikov, J. A. Kilner, *Solid State Ionics* **1998**, *113*, 565.

[17] S. Azad, O. A. Marina, C. M. Wang, L. Saraf, V. Shutthanandan, D. E. McCready,

A. El-Azab, J. E. Jaffe, M. H. Engelhard, C. H. F. Peden, S. Thevuthasan *Appl. Phys. Lett*. **2005**, *86*, 131906.

[18] V. Boffa, T. Petrisor, L. Ciontea, U. Gambardella, S. Barbanera, *Phys. C* **1996**, *260*, 111.

[19] A. Orsini, P.G. Medaglia, S. Sanna, E. Traversa, S. Licoccia, A. Tebano, G. Balestrino, *Superlattices and Microstruct*, **2009**, *46*, 223.

[20] M. Mogensen, N. M. Sammes, G. A. Tompsett, *Solid State Ionics* **2000**, *129*, 63.

[21] W. Lai, S. M. Haile, *J. Am. Ceram. Soc*. **2005**, *88*, 2979.

[22] J. L. M. Rupp, A. Infortuna, L. J. Gauckler, *J. Am. Ceram. Soc*. **2007**, *90*, 1792.

[23] G. M. Choi, Tuller, J. Am. Ceram. Soc. **1988**, *71*, 201.

[24] I. Kosacki,T, C. M. Rouleau, P. F. Becher, J. Bentley, D. H. Lowndes, solid Sate Ionics **2005**, *176*, 1319.

Chapter 5

Nanostructured cathode thin films grown by pulsed laser deposition

5.1 Introduction

In the recent years many researches are working to realize Solid Oxides Fuel Cell in micrometric scale (micro-SOFCs). Micro-SOFCs are very promising because a reduction to the micro-scale of the fuel cell components (cathodes, electrolytes and anodes) thickness has relevant consequence to increase the performances. Higher performance of the SOFCs means to reduce the working temperature (about 1200 °C

for conventional SOFC based on yttria-stabilized zirconia) and used as batteries in the portable devises. Reduction of SOFC operating temperatures is a prerequisite for their use in portable devices [1,5]. This can be achieved reducing the electrolyte thickness thus reducing its ohmic resistance,[6] and indeed μ-SOFCs are fabricated using materials in thin film form [7-11]. The integration of thin film SOFC materials with silicon technology takes advantage of recent progress in creating complex 3D structures utilizing a variety of micromachining techniques. Moreover, a micro-fabricated fuel cell could, in principle, be integrated onto a single chip with other electronic circuits, enabling extended, remote operation of electronic devices [12-15]. However, lowering the SOFC operating temperature makes slow the kinetics of charge transfer reactions at the electrolyte-electrode interfaces, mainly at the cathode [16]. This results in a worst fuel cell performance, because the lower the fuel cell working temperature, the larger the cathode overpotential. In fact, up to now the selection of cathode materials for μ-SOFCs has been limited to Pt, [17,18] while more performing cathode materials have been proposed but not yet implemented in a device [7,19,20]. To overcome this shortcoming, materials with a high electrocatalytic activity towards oxygen reduction reaction and enhanced oxygen diffusion properties are usually required for IT-SOFC applications [21,22]. Good performance of the electrodes, though, depends also on their internal microstructure, a feature that has remained largely hidden until recently [23]. To ensure the required performance, cathodes must possess a large active surface area with low area specific resistance (ASR) and large triple phase boundary (TPB) at the electrode/electrolyte interface [24]. The large TPB is considered paramount mainly for pure electronic conducting cathode materials. In this perspective, the nanometre-scale reduction

factor becomes crucial for the electrodes of miniaturized SOFCs, because TPB length and active surface can be significantly constrained by the small size of the device if tailored with conventional SOFC micrometer-sized morphologies. Generally, large TPB and low ASR can be achieved by a wide and well-interconnected porosity, high electronic and ionic conductivity, enhanced gas diffusion, and no formation of resistive additional phases at the electrode/electrolyte interfaces [25]. Therefore, the microstructural features of μ-SOFC cathodes must be rescaled at the nanometer level to ensure a proper active site density.

The choice of coupling Yttria Stabilized Zirconia (YSZ) and Samarium Doped Ceria (SDC) with $La_{0.6}Sr_{0.4}Co_{0.2}Fe_{0.8}O_{3-\delta}$ (LSCF) was made despite of the general knowledge that the two materials react producing insulating phases at the interface, based on previous results that showed a good performance when the LSCF processing temperature was kept below 900°C [26]. One of the most suitable technique for fabrication of micro-SOFC is Pulsed Laser Deposition technique (PLD) [27-33]. PLD is a technique particularly suitable in the case of dense or porous ultra thin films of composite oxide materials [34]. Moreover, by this technique, we can grow epitaxial thin films with high crystallographic order, heterostructures and superlattices [35].

5.2 Thin films deposited on polycrystalline substrates

LSCF onto SDC polycrystalline

Micro-SOFCs consisting of anodes, electrolyte and cathodes. In particular in this thesis our attentions were focused on cathodes and electrolytes.

Figure 1 shows the XRD of (LSCF) usually used as cathode deposited on polycrystalline electrolyte Samarium oxide (20 mol%)-doped ceria (SDC).

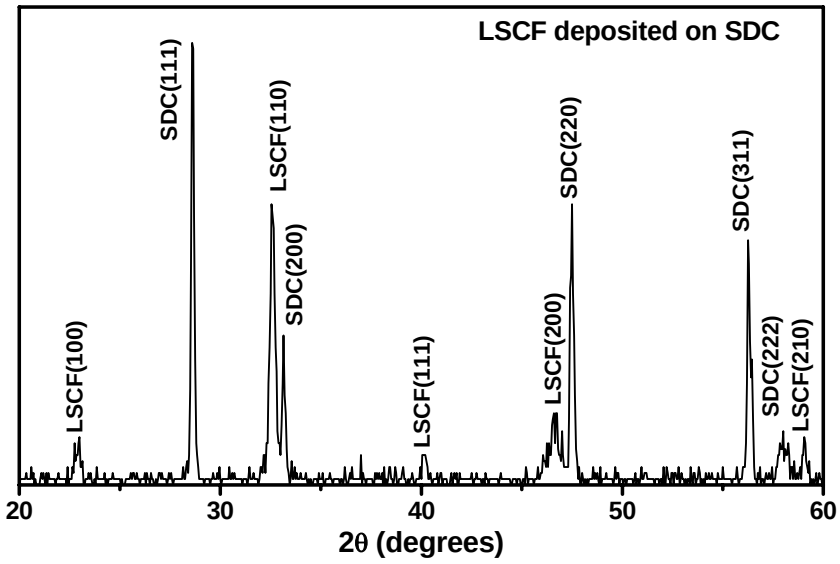

Figure 1. θ-2θ scan of LSCF thin film deposited on poly-crystalline SDC.

By θ-2θ scan several orientations of SDC and LSCF are revealed without spurious phases. Figure 2 shows the FE-SEM of dense LSCF films deposited onto poly-crystalline SDC.

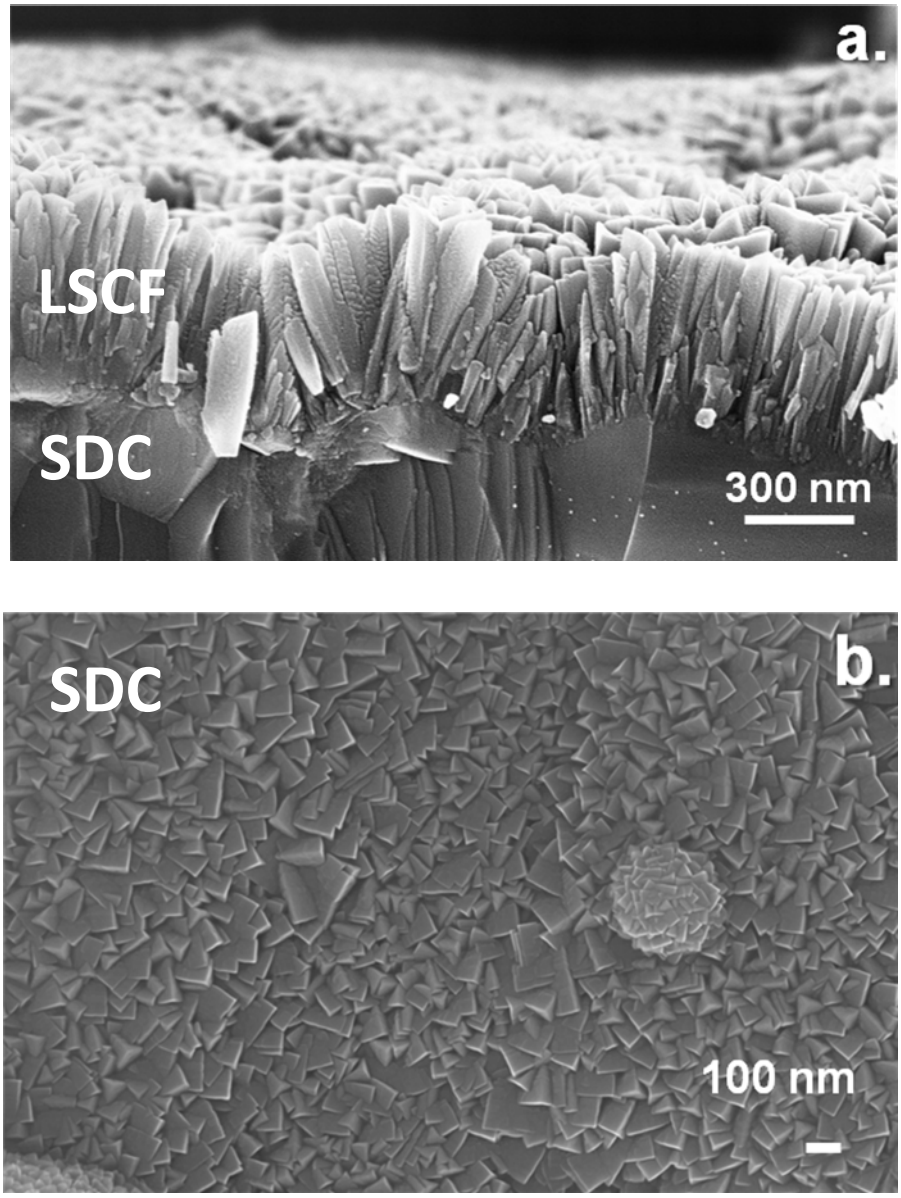

Figure 2. FE-SEM micrographs of dense LSCF deposited onto SDC poly-crystalline: (a) cross section, (b) plan wiew.

Figure 3 shows the Nyquist plot of dense LSCF deposited onto SDC at 700°C in O_2.

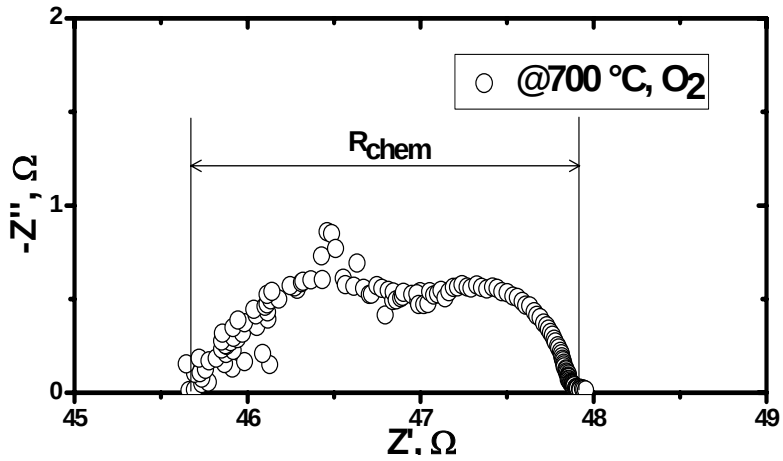

Figure 3. Nyquist plot of dense LSCF deposited onto SDC SDC poly-crystalline.

From the Nyquist plot two contributions can be separated. Figure 4 shows the area specific resistance (ASR) Arrhenius plot of dense LSCF in air (full circles) and in oxygen atmosphere (empty circles) .

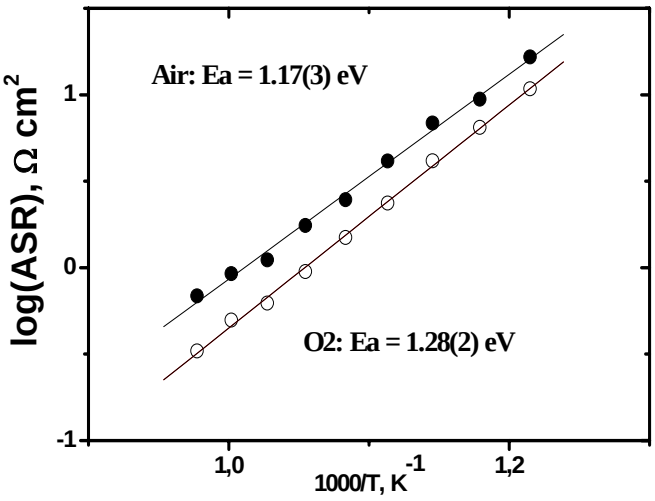

Figure 4. ASR Arrhenius plot of LSCF electrodes in air (full circles) and O_2 (empty circles).

5.3 SDC deposited onto YSZ polycrystalline

Figure 5 shows the XRD of LSCF cathode deposited on polycrystalline electrolyte YSZ.

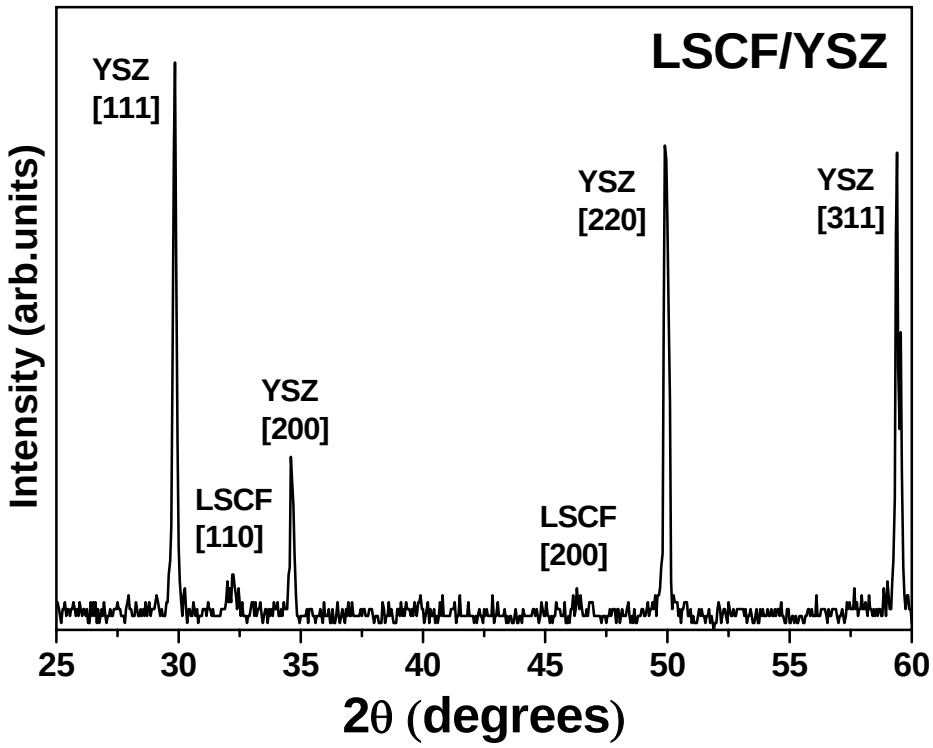

Figure 5. θ-2θ scan of LSCF thin film deposited on poly-crystalline YSZ.

Figure 6. shows the FE-SEM micrographs of LSCF films as-deposited on polycrystalline YSZ at $pO_2 = 4 \cdot 10^{-4}$ bar with a substrate temperature (Ts) of 700 °C and post-annealed at 800 °C for 12 h. Figure 1a shows the LSCF/YSZ fractured cross-section.

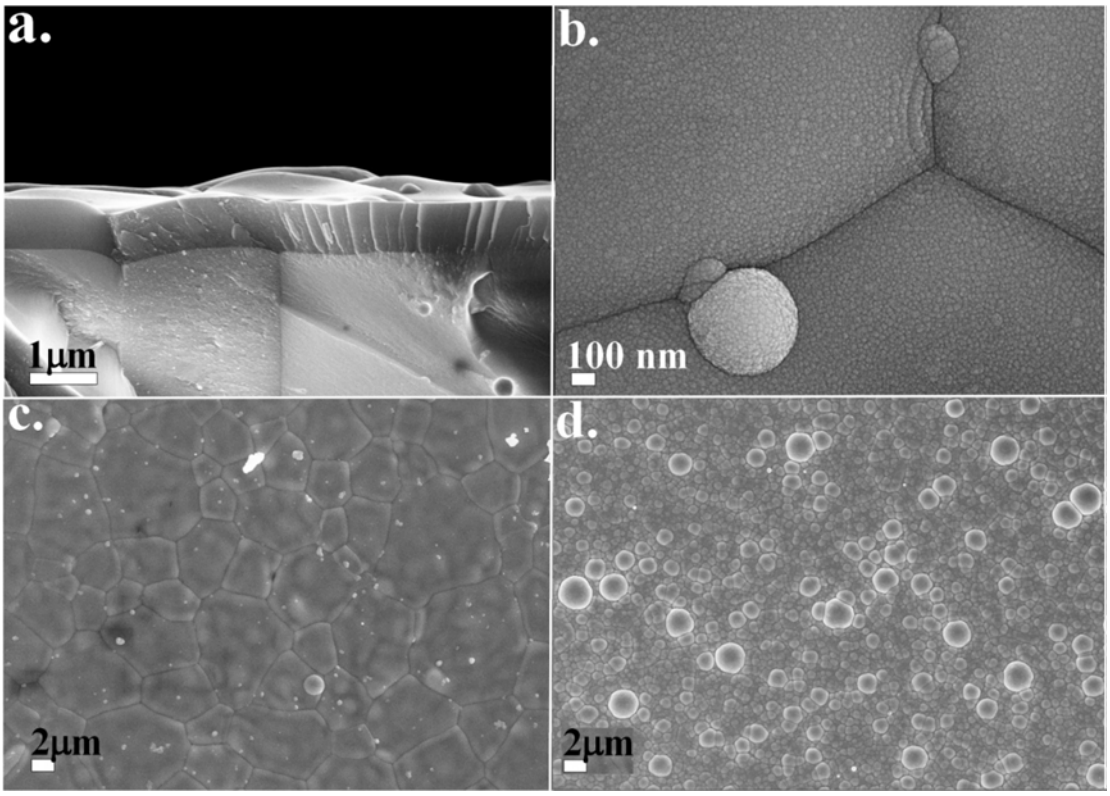

Figure 6. FE-SEM micrographs of the dense LSCF films deposited at $pO_2 = 4 \cdot 10^{-1}$ mbar and substrate temperature of 700 °C, as-deposited on polycrystalline YSZ (a: cross-section; b: high magnification plan-view; and c: low magnification plan-view) and post-annealed at 800 °C for 12 h (d: plan view).

The 600 nm-thick LSCF film was dense and homogeneous along the growth direction axis. The film replicated the roughness (~ 50 nm) and, interestingly, also the grain shape of the YSZ substrate surface, as shown in figures 6b and 6c, which report the LSCF film plan-views at high and low magnifications, respectively. Figure 1b shows that the LSCF film was polycrystalline with crystal size of a few nanometers when deposited on the YSZ grain bulk, while discontinuities were observed at YSZ grain boundaries. At high Ts, LSCF nucleated and grew replicating the YSZ substrate morphology. Figure 6d shows the FE-SEM micrograph of the LSCF film after post-annealing at 800 °C for 12 h. The post annealing induced LSCF

grain growth with a crystalline rearrangement, which led to the formation of spherical grains and the disappearance of the YSZ grain boundary replica texture.

The film density and homogeneity were preserved after the annealing. No cracks or exfoliation, due to thermal mismatch between substrate and the deposited material, were observed along the film thickness or at the film/substrate interface. Homogeneous and dense LSCF films with a thickness of 600 nm were produce when the substrate temperature was kept above 300 °C, with similar characteristics of the film shown in figure 6. Figure 7 shows the FE-SEM micrographs of fractured cross-section (figure 7a) and plan-view (figure 7b) of the LSCF films as-deposited on polycrystalline YSZ at $pO_2 = 4 \cdot 10^{-4}$ mbar with the substrate kept at room temperature.

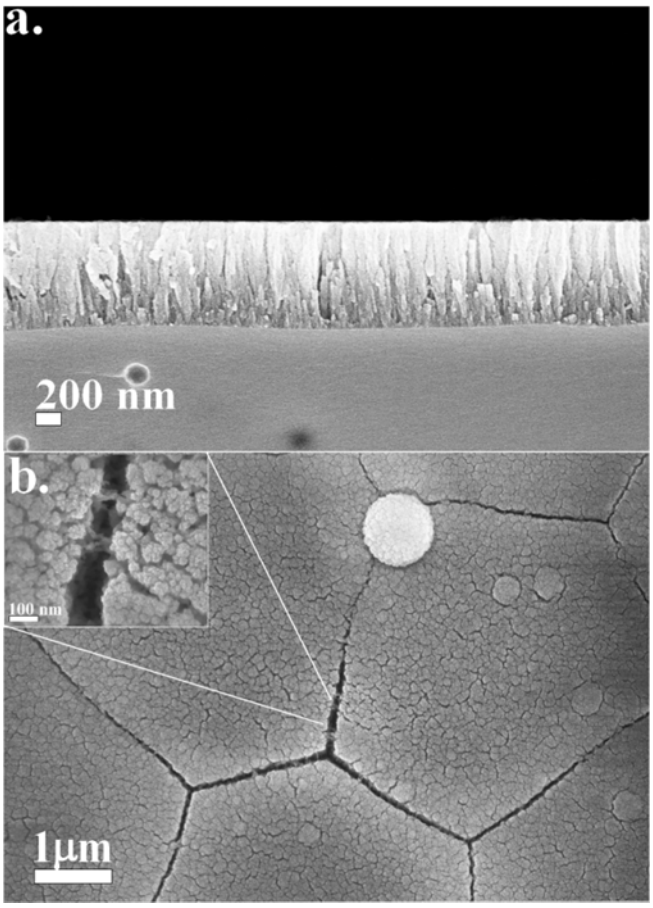

Figure 7. FE-SEM of the LSCF films as-deposited on polycrystalline YSZ: (a) cross section, (b) and (c) plan-view.

Figure 8 shows the FE-SEM of fractured cross-section (figure 8a and b) and plan-view (figure 8c and d) of the same film post-annealed at 800 °C for 12 h.

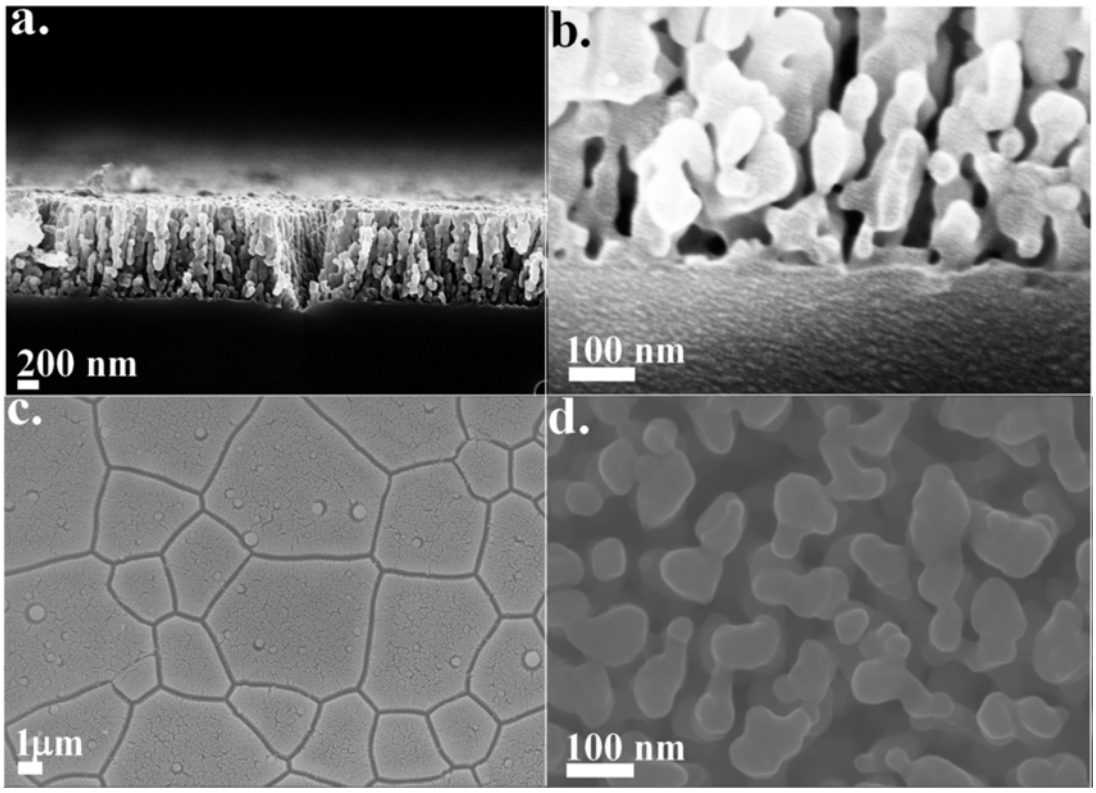

Figure 8. FE-SEM micrographs of the porous LSCF films deposited at $pO_2 = 4 \cdot 10^{-1}$ mbar and substrate kept at room temperature, as-deposited on polycrystalline YSZ post-annealed at 800 °C for 12 h: (a) and (b) the cross-section; (c) and (d) plan-view.

The surface of the LSCF film deposited at low temperature before annealing was made of nanometric spherical particles arranged in a porous layer. Figure 7a shows the columnar arrangement of small particles after deposition (see also inset in figure 7b), which trapped interconnected porosity in the nanosized range [32]. Figure 7b shows in detail that the as-deposited LSFC film surface replicated the substrate morphology with grooves in correspondence of the YSZ grain boundaries. This fact might be attributed to the disorder of the grain boundary regions that avoided the

LSCF deposition. The figure 8 emphasizes that the LSCF film was made of nanometric particles in an extremely open framework. After annealing at 800 °C for 12 h, the film preserved the porosity, which was even increased by the LSCF shrinkage, and the nanoparticles reached a mean particle size of 50 nm, as shown in figure 8c. The film thickness was about 600 nm, the same as for the dense LSCF films. The film was nanoporous and homogeneous in the whole thickness and surface, apart from grooves about 200 nm wide, which remained in correspondence of the YSZ grain boundaries after post-annealing. The figure 8b shows a high magnification of the LSCF/YSZ interface, demonstrating an excellent adhesion of the film and a large TPB length. Figure 8d shows the plan-view of the LSCF porous layer with its high magnification, clearly showing in the LSCF film the presence of the 200 nm-sized grooves in correspondence of the YSZ grains. Moreover, the annealed LSCF film grew with well-interconnected particles and porosity (fig.8d). Such morphology is unique and highly desirable to increase the cathode performance in SOFCs and it can be hardly obtained by conventional techniques. The factors leading to the formation of the porous layers are the rapid condensation of the plasma occurring during the laser deposition when a cold substrate was used. Condensation of the target material onto the substrate formed particles and entrapped gas at the nanometric level.

5.4 Electrochemical characterization (EIS) of dense and porous LSCF deposited onto polycrystalline YSZ

While for the dense films a Pt current collector allowed to obtain EIS measurements, the presence of structural discontinuities at the grain boundary of the porous LSCF films hindered electrical percolation at the electrodes. The problem was solved by using a continuous LSCF layer as a current collector, prepared by slurry coating. For sake of comparison, measurements were performed using the LSCF current collectors also in the case of the dense films, obtaining results not different from those obtained with Pt current collectors. Figure 9 shows the Nyquist plots (-Im(Z) vs Re(Z)), measured at 750 °C for dense (figure 9a) and porous (figure 3b) electrodes in air and oxygen.

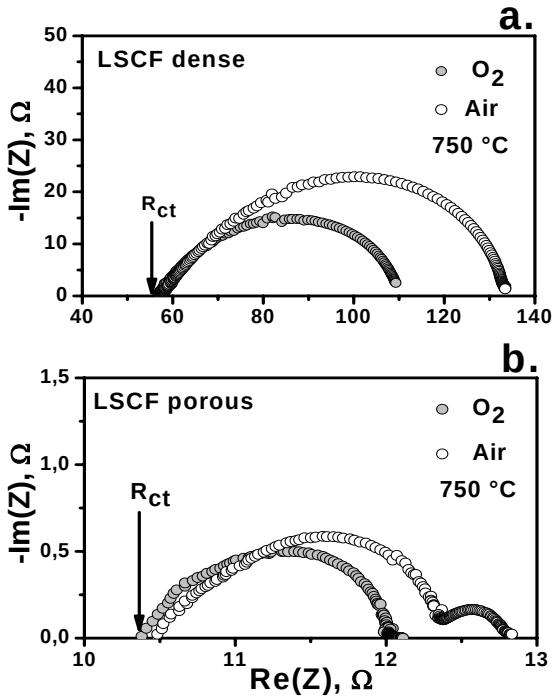

Figure 9: Nyquist plots, at 750 °C for dense(a) and porous (b) electrodes in air and oxygen.

Figures 9a and 9b show typical arcs related to the symmetrical cell electrochemical response where the low Re(Z) intercepts represents the charge transfer resistance (R_{ct}), corresponding to the ohmic YSZ electrolyte resistance (R_{el}), and the ohmic chemical resistance value (R_{chem}) is the resistance due to LSCF electrode polarization [24,36,37]. In the Nyquist plots, the Gerischer model fits properly both the dense and porous LSCF electrode polarization impedance responses indicating the presence of oxygen sorption diffusion limited processes at the electrodes [24]. As a consequence, the measured R_{chem} values were observed to decrease with increasing the pO_2 from air to pure oxygen. While in air the dense electrode samples at 750 °C showed a single arc with a typical capacitance values of ~10^{-5} F and a relaxation frequency of about 50 Hz (figure 9a), the porous electrode samples showed two arcs with typical capacitance values of 10^{-5}-10^{-4} F for the high frequency arc and 10^{-1} F for the additional arc observed at lower frequencies (figure 9b).

In oxygen, both samples showed a single arc. The frequency distribution of the impedance imaginary part gives crucial information about the kinetics of the polarization process steps; each process involved in the polarization showing peaks at given typical frequencies (and time constants) [37]. Each contribution to polarization, such as gas dissociation, sorption-desorption, diffusion mechanisms, etc., can be distinguished by associated typical values of frequency and capacitance of the imaginary impedance components [24, 37].

Figures 10a and 10b show that both the dense and porous samples presented two peaks correlated with reaction steps, apart from a third peak observed for the porous samples in oxygen at 750°C.

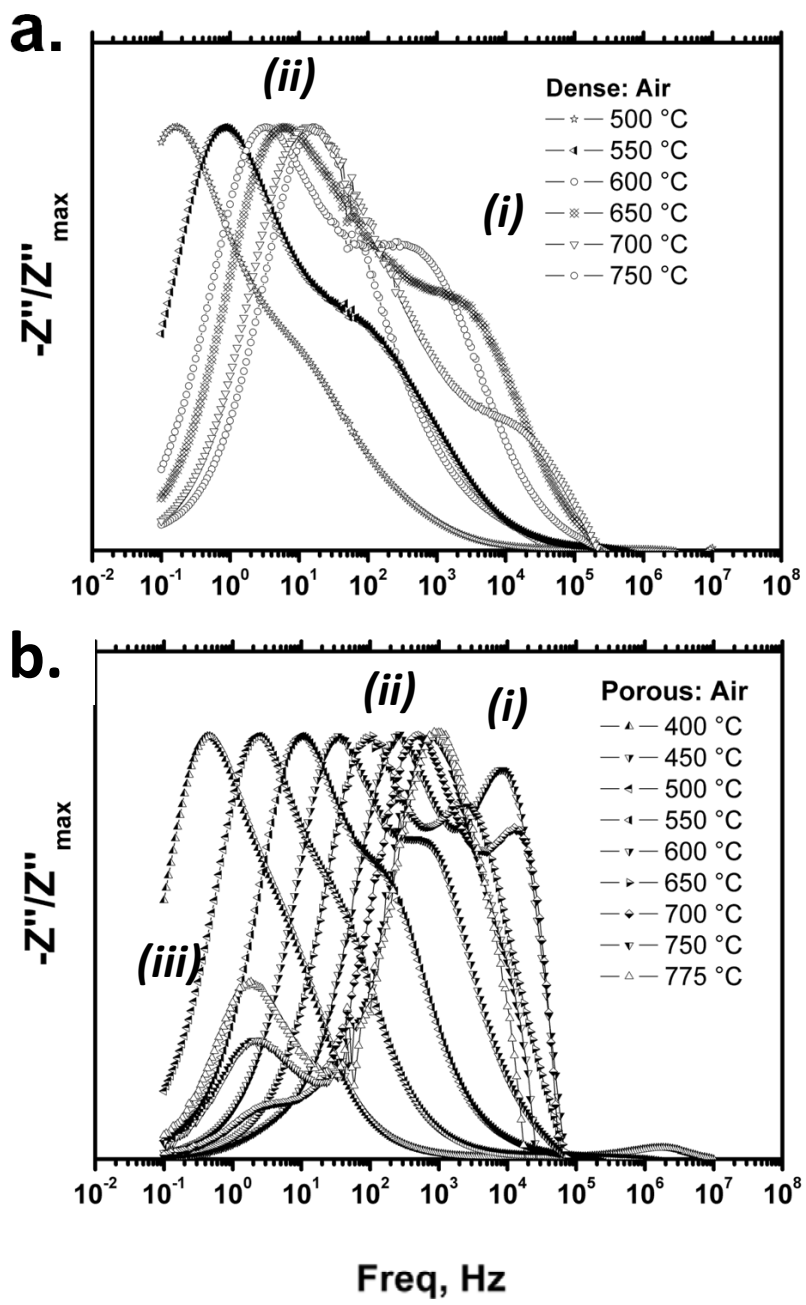

Figure 10. normalized imaginary impedance frequency distribution for dense (a) and porous (b) electrodes in air.

The high frequency peaks in the figure 10a b *(i)*, presented their maxima at the same frequency at the same temperatures, for both dense and porous samples, showing the

same relaxation time and thus the same conduction mechanism. The high frequency *(i)* contributions are usually attributed to the charge transfer reaction process, where oxygen vacancies diffuse through the YSZ/LSCF interface, in a solid-solid reaction mechanism [37]. This process depends mainly on the electrical properties and contact features at the materials interface [26]. EIS measurements clearly showed the absence of highly resistive phases or spread resistances that constrain the current lines at the YSZ/LSCF interface, for both dense and porous PLD electrodes. The formation of resistive phases at the LSCF/YSZ interface is considered the main cause of the cathodic degradation and polarization that avoid the use of LSCF as a cathode for YSZ [25]. It is worth noticing that a clean YSZ/LSCF interface can be achieved using PLD and post-annealing temperatures not larger than 800°C.

The frequency at the maximum of the *(ii)* peaks increased with increasing the measurement temperature, for both dense and porous samples. The peaks labelled a *(ii)* showed typical frequency and capacitance values associated to gas-solid reactions (desorption, absorption, and dissociation), and gas diffusion (at the surface and through the electrode bulk) Phenomena [24,37]. The spectroscopic plots in figures 10a and 10b indicated that the major contribution for both electrodes was ascribable to gas-solid reactions. However, the relaxation frequencies for the processes *(ii)* were different for the dense and porous electrodes, indicating a faster process at higher frequencies for the porous electrodes (figure 10a and 10b).

Therefore, the porous and dense electrodes are dominated by distinct mechanisms. For the highly porous electrodes, where TPB was larger, the polarization is supposedly a surfacelimited process where oxygen adsorption (or co-limited oxygen

adsorption-diffusion) process is the rate-determining step (*rds*) for the overall gas-solid reaction process [24].

Conversely, dense electrodes exhibited diffusion-limited processes because the TPB-length was nearly zero and the oxygen reduction/oxidation reactions are controlled by the ambipolar diffusion of O_{2-} through the mixed ionic-electronic conducting film. This explanation is supported by the remark that, for the nano-porous electrodes obtained by PLD, the faster *rds* is a consequence of the large surface area and TPB, resulting in a large materials portion directly exposed to the gas/solid interaction. In other words, nano-porous electrodes behave as a "pure surface" and the other limiting processes were not revealed. On the other side, dense electrodes behaved as "pure bulk" because the exposed electrodes area was small and the dominant process was oxygen vacancy diffusion and transport. The low-frequency contribution at high capacitance (10^{-1} F) observed for the porous samples in oxygen at 750°C (peak *(iii)* in figure 3d) can be associated to gas conversion cathode-loss that is typically observed for porous electrodes in N2-O2 mixtures (*i.e.* air), resulting from an oxygen concentration gradient in the cathode, which is due to a hysteresis in the oxygen sorption-adsorption on top of the electrode with respect to the electrode/electrolyte interface region [37]. This is confirmed by the fact that this gas-conversion arc disappeared when pure O2 was fed to the electrode, because the O2 partial pressure was constant (figure 3b). Moreover, this effect was observed only at temperatures higher than 700 °C, because at lower temperatures all the other mechanisms have larger impedances. Figure 11 shows the Arrhenius plots of the ASR for the dense and porous electrodes in air and oxygen. Samples with dense electrodes showed ASR values of 10 Ωcm^2 at 750 °C and activation energy (E_a) values around 1.1 eV, both in

air and oxygen. An ASR values around 10 Ωcm^2 at 750 °C has been reported as a satisfactory performance for a LSCF/YSZ cell fabricated with conventional processing methods [4]. Larger ASR values could be expected for dense LSCF electrodes because of the limited gas/electrode exchange surface and the nearly-zero TPB-length. Such finding confirmed that the use of relatively low temperatures for the deposition and the post annealing treatment of LSCF avoided the formation of resistive phases that are usually formed at the interface in conventional electrodes by the reaction with YSZ.

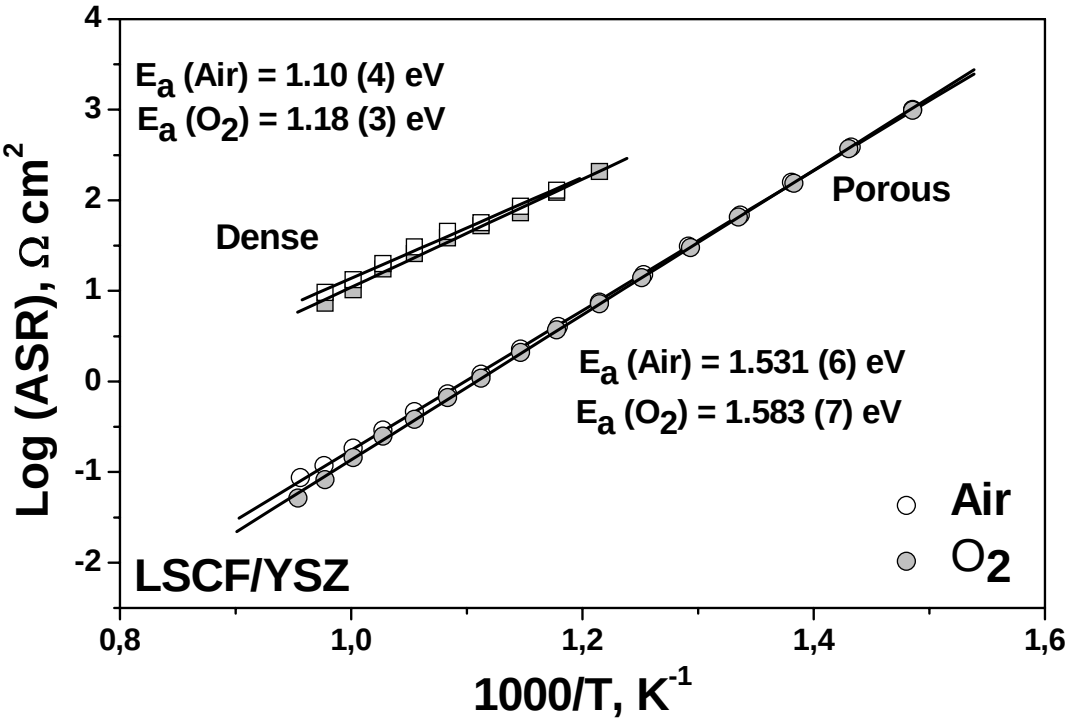

Figure 11. Arrhenius plots of the ASR for the dense and porous electrodes in air and oxygen.

In the table 1 ASR values for dense and porous electrodes are reported in air and O_2 at several temperature for comparison.

T(°C) in AIR	Dense chatode ASR(Ωcm^2)	Porus chatode ASR(Ωcm^2)
775	6.62	0.08
750	9.62	0.117
700	19.9628	0.29
600	86.06	2.27
500	374	31.02
400	1950	1001.52

T(°C) in O_2	Dense chatode ASR(Ωcm^2)	Porus chatode ASR(Ωcm^2)
775	4.8	0.05
750	7.32	0.08
700	17.42	0.25
600	7.06	2.09
500	578	30.03
400	2912	984.22

Table1.

Porous electrodes showed at 750 °C ASR values of 0.08 Ωcm^2 in oxygen and 0.1 Ωcm^2 in air, which are more than two orders of magnitude smaller than the ASR values measured for the dense films. The activation energies (E_a) calculated for the porous electrodes were around 1.5 eV. The porous electrodes showed very low ASR values also when compared with ASR values reported in the literature for conventional or highly performing lanthanum based perovskite-type cathodes [4, 12, 16, 17]. This result can be ascribed to the large specific surface area and especially to the wide TPB length of the nano-porous films obtained by PLD. Therefore, the findings clearly showed that the presence of a large TPB is paramount to reduce the cathode polarization not only of electronic conductor materials, such as lanthanum manganite, but also of a mixed ionic-electronic compound such as LSCF. Polarization activation energy values around 1-1.6 eV are commonly observed for LSCF conventional electrodes. The differences in the *Ea* values usually depend on the perovskite composition or in the electrode fabrication thermal condition [17]. For PLD electrodes, different E_a values can be ascribed only to the electrode morphology, which determines a dominant process at the TPB for the porous

electrodes and to the gas exchange at the surface area for the dense ones. Morphologies were crucial not only for the R_{chem} reduction, but also for the *rds* mechanisms of the entire polarization process. These factors have to be considered in tailoring the electrochemical properties of miniaturized electrodes. The performance of porous LSCF deposited onto YSZ substrate is comparable to the performance of dense LSCF deposited onto GDC pellet, probably it is due to the fact that the film deposited onto GDC shows a columnar structure and many TPB can be present at the LSCF/GDC interfaces.

5.5 Conclusion

In summary, PLD was successfully used to deposit dense and porous LSCF layers onto polycrystalline YSZ substrates. Electrode microstructure was finely controlled by the substrate temperature and nano-porous layers were produced and stabilized by post-annealing thermal treatment at relatively low temperature (800 °C). Very small ASR values were obtained for the LSCF/YSZ cells, particularly when porous electrodes were used. The use of low temperature for the processing avoided the formation of detrimental phases at the electrode/electrolyte interfaces. Extremely fast processes for nanoporous electrodes were observed. The rate determining step for dense electrodes was attributed to the oxygen diffusion through the electrodes, with an activation energy of 1.1 eV both in air and oxygen. Polarization of the porous electrodes was controlled by gas-solid surface reaction processes occurring at the TPB, with typical activation energy around 1.6 eV. Nanoporous electrodes prepared by PLD showed very low ASR values, below 10^{-1} Ωcm^2 at 750 °C in air, which make

these films very promising as cathode materials for μ-SOFC development. The presence of a large TPB has demonstrated to play a paramount role to improve the electrochemical performance also of a mixed ionic-electronic conductor like LSCF.

References

[1] G.A. Tompsett, C. Finnerty, K. Kendall, T. Alston, N.M. Sammes, *J. Power Sources* **2000**, *86*, 376.

[2] A. Bieberle-Hütter, D. Beckel, A. Infortuna, U.P. Muecke, J.L.M. Rupp, L.J. Gauckler, S. Rey-Mermet, P. Muralt, N.R. Bieri, N. Hotz, M.J. Stutz, D. Poulikakos, P. Heeb, P. Müller, A. Bernard, R. Gmür, T. Hocker, *J. Power Sources* **2008**, *177*, 123.

[3] A. Boudghene Stambouli, E. Traversa, *Renewable and Sustainable Energy Rev.* **2002**, *6*, 433.

[4] K. Kendall, M. Palin, *J. Power Sources* **1998**, *71*, 268.

[5] N.M. Sammes, R.J. Boersma, G.A. Tompsett, *Solid State Ionics* **2000**, *135*, 487.

[6] S.J. Litzelman, J.L. Hertz, W. Jung, H.L. Tuller, *Fuel Cells* **2008**, *5*, 294.

[7] J. Fleig, H.L. Tuller, J. Maier, *Solid State Ionics* **2004**, *174*, 261.

[8] J. Will, A. Mitterdorfer, C. Kleinlogel, D. Perednis, L. Gauckler, *Solid State Ionics* **2000**, *31*, 79.

[9] Y. Tang, K. Stanley, J. Wu, D.G.J. Zhang, *J. Micromech. Microeng.* **2005**, *15*, S185.

[10] D. Beckel, A. Bieberle-Hütter, A. Harvey, A. Infortuna, U.P. Muecke, M. Prestat, J.L.M. Rupp, L.J. Gauckler, *J. Power Sources* **2007**, *173*, 325.

[11] S. J. Litzelman, J. L. Hertz, W. Jung, H. L. Tuller, *Fuel Cells* **2008**, *5*, 294.

[12] J.P. Nair, E. Wachtel, I. Lubomirsky, J. Fleig, J. Maier, *Adv. Mater.* **2003**, *15*, 2077.

[13] J.L. Hertz, H.L. Tuller, *J. Electroceram.* **2004**, *13*, 663.

[14] D. Perednis, L.J. Gauckler, *Solid State Ionics* **2004**, *166*, 229.

[15] S. Rey-Mermet, P. Muralt, *Solid State Ionics* **2008**, *179*, 1497.

[16] T. Horita, K. Yamaji, M. Ishikawa, N. Sakai, H. Yokokawa, T. Kawada, T. Kato, *J. Electrochem. Soc.* **1998**, *145*, 3196.

[17] H. Huang, M. Nakamura, P. Su, R. Fasching, Y. Saito, F. B. Prinz. *Journal of The Electrochemical Society* **2007**, *154*, B20.

[18] A. Bieberle-Hütter, J.L. Hertz, H.L. Tuller, *Acta Mater.* **2008**, *56*, 177.

[19] M. Prestat, J.-F. Koenig, L.J. Gauckler, *J. Electroceram.* **2007**, *18*, 87.

[20] M. Prestat, A. Infortuna, S. Korrodi, S. Rey-Mermet, P. Muralt, L.J. Gauckler, *J. Electroceram.* **2007**, *18*, 111.

[21] J.M. Ralph, C. Rossignol, R. Kumar, *J. Electrochem. Soc.* **2003**, *150*, A1518.

[22] Z. Shao, S.M. Haile, *Nature* **2004**, *431*, 170.

[23] J.R. Wilson, W. Kobsiriphat, R. Mendoza, H.-Y. Chen, J.M. Hiller, D.J. Miller, K. Thornton, P.W. Voorhees, S.B. Adler, S.A. Barnett, *Nature Mater.* **2006**, *5*, 541.

[24] S.B. Adler, *Chem. Rev.* **2004**, *104*, 4791.

[25] J. Fleig, J. Maier, *J. Electroceram.* **1997**, *1*, 73.

[26] D. Z. de Florio, R. Muccillo, V. Esposito, E. Di Bartolomeo, E. Traversa, *J. Electrochem. Soc.* **2005**, *152*, A88.

[27] J.H. Joo, G.M. Choi, *Solid State Ionics* **2006**, *177*, 1053.

[28] D. Yang, X. Zhang, S. Nikumb, C. Decès-Petit , R. Hui, R. Maric, D. Ghosh, *J. Power Sources* **2007**, *164*, 182.

[29] D. Pergolesi, V. Esposito, A. Tebano, P.G. Medaglia, S. Sanna, S. Licoccia, G. Balestrino, E. Traversa, *ECS Trans.* **2007**, *7 [1]*, 891.

[30] A. Infortuna, A.S. Harvey, L.J. Gauckler, *Adv. Funct. Mater.* **2008**, *18*, 127.

[31] E. Koep, C.M. Jin, M. Haluska, R. Das, R. Narayan, K. Sandhage, R. Snyder, M.L. Liu, *J. Power Sources* **2006**, *161*, 150.

[32] J. Yoon, R. Araujo, N. Grunbaum, L. Baqué, A. Serquis, A. Caneiro, X. Zhang, H. Wang, *Appl. Surf. Sci.* **2007**, *254*, 266.

[33] D. Beckel, A. Dubach, A.N. Grundy, A. Infortuna, L.J. Gauckler, *J. Eur. Ceram. Soc.* **2008**, *28*, 49.

[34] B.N. Nair, T. Suzuki, Y. Yoshino, S. Gopalakrishnan, T. Sugawara, S.-I. Nakao, H. Taguchi, *Adv. Mater.* **2005**, *17*, 1136.

[35] D.X. Huang, C. L. Chen, and A. J. Jacobson, *J. Appl. Phys.* **2005,** *97*, 043506.

[36] E.J. Abram, D.C. Sinclair, and A.R. West, *J. Electroceram.* **2003**, *10*, 165.

[37] S.H. Jensen, A. Hauch, P.V. Hendriksen, M. Mogensen, N. Bonanos, and T. Jacobsen, *J. Electrochem. Soc.* **2007**, *154*, B1325.

Conclusions

Complex oxides and heterostructures in thin film shape, grown by Pulsed Laser Deposition, were studied in this thesis. Especially this work was focused on microstructure and electrochemical characterization of electrolytes and cathodes for SOFC applications. In particular our attention was directed on the most promising materials such as SDC, used as electrolyte, and LSCF used as cathode in the SOFCs. This work shows the importance of low crystalline disorder for the thin films, that must be stable in reducing and oxidizing atmosphere in the 400°C to 800°C temperature range. Perovskite substrates provide a proper lattice match for fluorite structure of SDC and YSZ, inducing the growth of epitaxial monocrystalline films with a low degree of structural disorder. However, perovskite substrates exhibit mixed ionic-electronic conduction at temperatures above 300 °C, which might affect the proper evaluation of the electrical measurements performed on ceria and zirconia

films. On the contrary MgO, which shows a remarkably low electrical conductivity at high temperatures, does not provide a good lattice match with the fluorite structure. To obtain a proper evaluation of the conductivity of epitaxial doped-ceria films, and SDC/YSZ superlattices was used to grow thin films on (001) MgO single-crystal substrates, using a STO thin film as a buffer layer, taking advantage of the good lattice match between MgO and STO. The chapter 3 showed that SDC single-crystal structure exhibited high stability in both oxidizing and reducing atmospheres. Conversely SDC on MgO is instable in hydrogen atmosphere where microstructural transformation lead to crack, porosity and delamination. The STO buffer layer gives the possibility to evaluate the SDC single-crystal film electrical properties without introducing contribution from conducting substrates. The single-crystal thin film shows conductivity about 0.07 S cm^{-1} at 700 °C and predominant ionic conductivity for pO_2 higher than 10^{-17} atm. Dominant electronic conductivity is observed at pO_2 below 10^{-17} atm.

High quality YSZ/SDC superlattices having different modulation length Λ deposited onto $SrTiO_3$ buffered (001) MgO substrates are reported in the chapter 4. Electrochemical measurements reported in chapter 4 showed that a sizeable increase of conductivity occurs at the interface between YSZ and SDC which has not an electronic origin as demonstrated by measurements at reduced pO_2. In agreement with many papers, the conductivity enhancement was attributed to tensile strain effects. XRD measurements demonstrated that, in our superlattices, the YSZ block is heavily strained. Noticeably, ionic conductivity enhancement effects persist down to the thinnest value of Λ= 7.7 nm, namely much smaller than that previously reported in literature. We ascribe this effect to the improved crystallographic quality of

interfaces in our $(YSZ/SDC)_N$/STO/MgO heterostructures preventing disruption of electric transport as a consequence of interface roughness.

As shown in the chapter 5, PLD was successfully used to deposit dense and porous LSCF layers onto polycrystalline YSZ substrates. Electrode microstructure was finely controlled varying the substrate temperature and nano-porous layers were produced and stabilized by post-annealing thermal treatment at relatively low temperature (800 °C). Very small ASR values were obtained for the LSCF/YSZ cells, particularly when porous electrodes were used. Polarization of the porous electrodes was controlled by gas-solid surface reaction processes occurring at the TPB, with typical activation energy around 1.6 eV. Nanoporous electrodes prepared by PLD showed very low ASR values, below 10^{-1} Ωcm^2 at 750 °C in air, which make these films very promising as cathode materials for micro-SOFC development. The presence of a large TPB was demonstrated to play an important role to improve the electrochemical performance even in the case of a mixed ionic-electronic conductor like LSCF.

List of publications and conferences

Thesis Related:

1. **S. Sanna**, V. Esposito, A. Tebano, S. Licoccia, E. Traversa and G. Balestrino.

Enhancement of ionic conductivity in Sm-doped Ceria (SDC)/Yttria-stabilized Zirconia (YSZ) heteroepitazial structures

2009, submitted to Small

2. D. Pergolesi, V. Esposito, A. Tebano, **S.Sanna**, P.G. Medaglia, S. Licoccia, G. Balestrino, E. Traversa

Ceria-Based Thin Film Hetero-structure Growth and Characterization for SOFC Applications.

ECS Transactions, **(2007)**, *7(1)*, 891-898.

3. **S. Sanna**, V. Esposito, D. Pergolesi, A. Orsini, A. Tebano, S. Licoccia, G. Balestrino, E. Traversa

Fabrication and Electrical Properties of Epitaxial Samarium-Doped Ceria Films Onto $SrTiO_3$-Buffered MgO Substrates.

Advanced Functional Materials, (**2009)**, *19*, 1713-1719.

4. A. Orsini, P.G. Medaglia, **S. Sanna**, E. Traversa, S. Licoccia, A. Tebano, G. Balestrino

Epitaxial Superlattices of Ionic Conductor Oxides.

Superlattices and Microstructures, **(2009)**, *46*, 223-226

5. V. Esposito, **S. Sanna**, E.Di Bartolomeo, G. Balestrino, S. Licoccia, E. Traversa

Nanostructured $La_{0.6}Sr_{0.4}Co_{0.2}Fe_{0.8}O_{3-\delta}$ Cathode Thin Films with Low Area Specific Resistance for Micro-Solid Oxide Fuel Cells (μ-SOFCs)

2009 Advanced Materials, submitted.

6. D. Pergolesi, E. Fabbri, A. D'Epifanio, E. Di Bartolomeo, A. Tebano, **S. Sanna**, S. Licoccia, G. Balestrino, E. Traversa

Crystalline Order Boosts Proton Conductivity of Yttrium-Doped Barium Zirconate Films for Intermediate Temperature Fuel Cells.

2009 sept. Submitted to Nature Materials.

7. E. Fabbri, A. D'Epifanio, **S. Sanna**, E. Di Bartolomeo, G. Balestrino, S. Licoccia, E. Traversa

Performance of a Single Chamber Solid Oxide Fuel Cell Based on a Thin Y-doped $BaZrO_3$ Proton Conducting Electrolyte.

2009, Submitted to Energy and Environmental Science.

Conferences

1. D. Pergolesi, V. Esposito, A. Tebano, P. G. Medaglia, **S. Sanna**, S. Licoccia, G. Balestrino, E. Traversa

Ceria-Based Thin Film Hetero-structure Growth and Characterization for SOFC Applications.

10th International Symposium on Solid Oxide Fuel Cells, SOFC-X, Nara (Japan), June **2007.**

2. **S. Sanna**, V. Esposito, D. Pergolesi, M. Zunic, G. Balestrino, S. Licoccia, E. Traversa

Pulsed laser deposition of dense and nano-porous $La_{0.8}Sr_{0.2}Co_{0.8}Fe_{0.2}O_{3-\delta}$ cathodes for IT-SOFCs applications.

212th ECS Meeting, Washington (DC, USA), October **2007**

3. A. Orsini, **S. Sanna**, P.Medaglia, A.Tebano, G. Balestrino, V. Esposito, E. Traversa, S. Licoccia

Nanolayers of heterogeneous ionic conductors

Nano SEA 2008, Second International Conference on Nanostructures SElf-Assembly, Monteporzio Catone, (Rome, Italy) 7 - 10 July **2008.**

4. **S. Sanna**, V. Esposito, S. Licoccia, G. Balestrino, E. Traversa

Microstructure and Electrochemical Properties of Epitaxial Samarium Doped Ceria (SDC)-$SrTiO_3$ (STO) Buffered-MgO Films by Pulsed Laser Deposition.

2008 MRS Fall Meeting, Boston, MA, USA, Dicembre **2008**

5. E. Fabbri, A. D'Epifanio, **S. Sanna**, E. Di Bartolomeo, G. Balestrino, S. Licoccia, E. Traversa (University of Rome Tor Vergata)

Intermediate Temperature Solid Oxide Fuel Cells (IT-SOFCs) Based on a Thin Protonic Conductor Electrolyte

215th ECS Meeting - San Francisco, CA, May 24-29, **2009**

6. D. Pergolesi, E. Fabbri, A. D'Epifanio, A. Tebano, S. Sanna, S. Licoccia, G. Balestrino, E. Traversa

Study of the Influence of the Morphology on the Proton Conductivity of Y-doped Barium Zirconate Thin Films.

215th ECS Meeting - San Francisco, CA, May 24-29, 2009

7. D. Pergolesi, E. Fabbri, A. D'Epifanio, A. Tebano, **S. Sanna**, S. Licoccia, G. Balestrino, E. Traversa

Fabrication of highly textured Y-doped barium zirconate thin films by pulsed laser deposition for bulk conductivity direct measurement.

11th International Conference on Advanced Materials, ICAM 2009, Rio de Janeiro, Brazil, Sept. 20-25, **2009**

8. **S. Sanna**, V. Esposito, D. Pergolesi, A. Orsini, E. Traversa, S. Licoccia

Electronics Fabrication and Electrochemical Properties of Epitaxial Samarium-Doped Ceria Films on SrTiO3-Buffered MgO Substrates

16th International Workshop on Oxide Electronics (WOE 16), Tarragona (Catalonia, Spain) October 4-7, **2009**.

Other publications

1 A. Tebano, C. Aruta, **S. Sanna**, P.G. Medaglia, G. Balestrino, A. A. Sindorenko R. De Renzi G. Ghiringhelli, L. Braicovich, Bisogni e N. B. Brookes.

Evidence of Orbital Reconstruction at Interfaces in Ultrathin $La_{0.67}Sr_{0.33}MnO_3$

Films**,** Physical Review Letters, **(2008),** *100,* 13, 137401-4.

2 S. Irrera, G. Contini, N. Zema, S. Turchini, **S. Sanna**, P. Moras, C. Crotti e T. Prosperi

Two-Dimensional Chiral Single Domain by D-Alaninol Functionalization of Cu(100)

Journal of Physical Chemistry B Letters, (**2007**), *111*, 7474-7480.

3 S. Irrera, G. Contini, N. Zema, S. Turchini, J. Fujii **S. Sanna**, e T. Prosperi *Adsorption of D-alaninol on Cu(100)*

Surface Science, **(2007)**, *601*, 2562–2565.

4 M. Lucci, **S. Sanna**, G. Contini, N. Zema, V. Merlo, M. Salvato, H.N. Thanh e I. Davoli.

Electron spectroscopy study in the NbN growth for NbN/AlN interfaces

Surface Science, **(2007)**, *601*, 2647–2650.